Thin Equilibrium Amorphous Films at a Model Metal-Ceramic Interface

RESEARCH THESIS

SUBMITTED IN PARTIAL FULFILLMENT OF THE
REQUIREMENTS FOR THE DEGREE OF
DOCTOR OF PHILOSOPHY

Amir Avishai

Submitted to the Senate of
The Technion – Israel Institute of Technology

Svat 5764 **Haifa** **February 2004**

The research thesis was performed under the supervision of Prof. Wayne D. Kaplan.

ACKNOWLEDGMENTS

I wish to thank Prof. Wayne D. Kaplan for his devoted guidance and help.

Prof. David Brandon, Prof. Rachman Chaim, Prof. Eugen Rabkin, Dr. L. Klinger, Dr. R. Ghez, Dr. Aleksander Reçnik, Dr. Alex Berner, and Dr. R. Brener for fruitful discussions and helpful suggestions.

A very warm thank you to Prof. Adrian Parsegian for his kind help and suggestions, and for allowing me to read his insightful book before it was finished.

I would like to express my gratitude to Prof. M. Rühle for the invitation to work at the Max-Plank Institute, Stuttgart, and the Minerva Fellowship Committee for supporting this visit (Minerva Seed Fellowship). I kindly acknowledge Dr. C. Scheu for her guidance during my stay at the MPI, and her assistance on the dedicated STEM. I would like to thank as well Dr. W. Siegle for his TEM operating tips.

I would like to thank my numerous friends at the Technion, especially my fellow students in the Metal-Ceramic Interface Group (Mike, Yaron, Tzipi, Moshe, Shaul, Adham, Lior and George) as well as Saed, Michal, Gili, and Adi.

My family for their support. My friend, and partner Nanthawan for her support and encouragement all along.

Carmel, and Hadar for distracting me from my writing and reminding me I should chase them around the house.

The generous financial support from Applied Materials (Applied Materials Fellowship). This research was partially supported by the Israel Science Foundation.

TABLE OF CONTENTS

LIST OF FIGURES

LIST OF TABLES

ABSTRACT

Intergranular amorphous equilibrium films at ceramic grain boundaries, interfaces, and free surfaces have been studied extensively. Microstructural features characterizing amorphous *equilibrium* intergranular films include a constant film thickness of the order of 1nm, which extends along the grain boundaries or interfaces, and a composition that is often based on an oxide combination including glass network formers such as SiO_2. It has been experimentally observed that the film thickness strongly depends on the composition and type of ions, while it weakly depends on the total amount of the additives in the bulk. The equilibrium thickness suggests a force balance exists between attractive and repulsive forces. Clarke modeled the force balance at grain boundaries in alumina, based on colloid-like behavior. The forces are dominated by long range attractive van der Waals (vdW) forces (Π_{DISP}) and steric disjoining forces (Π_{ST}), which act to establish the equilibrium intergranular film thickness.

Recently the presence of intergranular films was experimentally observed at *Cu-alumina* interfaces in melt-infiltrated alumina matrix composites, raising the question whether equilibrium films may exist at *metal-ceramic* interfaces. If so, this is an important phenomenon, potentially critical to controlling both mechanical and functional properties of metal-ceramic interfaces.

The primary goal of this research was to conduct a basic scientific study to determine whether intergranular equilibrium films are stable at *metal-ceramic* interfaces. In this work the structure, chemistry, and energy of intergranular films at *metal*-ceramic interfaces were investigated via detailed microstructural characterization of model *metal*-Al_2O_3 nanocomposites, and wetting/dewetting experiments. Cu-Al_2O_3 and Ni-Al_2O_3 composites, with and without glass-forming additives, were produced and characterized. Cu/Ni-sapphire wetting and dewetting experiments were performed with and without the presence of anorthite glass.

The glass doped composites contained amorphous glass pockets, as well as intergranular films at the *metal*-Al_2O_3 interfaces. Chemical analysis of the glass pockets and intergranular films showed they differ in composition. The film thickness was found to be different between the two types of metal-alumina interfaces for the same

terminating alumina planes. High spatial resolution energy dispersive spectroscopy showed the two interfaces also have a different composition. On the other hand, no amorphous phase was observed in the undoped composites.

It was observed in the composite materials that glass doping promotes metal particle *occlusion*. This indicates a specific role of intergranular films in particle occlusion, resulting in significant changes to the nanocomposite microstructure and properties.

Wetting experiments of Ni on sapphire performed in the presence of a glass drop resulted in glass elements penetrating the Ni-sapphire interface. This caused a considerable lowering of the contact angle and the interfacial energy.

Calculations of Hamaker coefficients were performed for metal-ceramic interfaces which indicated that a stronger attractive force is expected for intergranular films at metal-alumina interfaces, relative to alumina grain boundaries, correlating to the film thickness measured in this work.

From the present study, it is evident intergranular films at metal-alumina interfaces are stable. The wetting experiments strengthen this conclusion. Using a colloid-like force balance model developed for ceramic systems and performing the calculations for a metal-ceramic interface in the presence of an intergranular film, it was shown that a similar force balance may be obtained for the a metal-ceramic interface.

LIST OF SYMBOLS AND ACRONYMS

α	The scaling factor
α_s	Solute drag force per unit velocity and per unit solute concentration in the low-velocity limit
β	The scaling factor
β_d^{-1}	An approximation of the drift velocity with which a solute diffuses across the near grain boundary region
$\hbar$	Planck's constant divided by 2π
η_0	Degree of epitaxy in intergranular film (1 being totally ordered, and 0 completely random)
ξ	Correlation length
Ω	Total ionic volume divided by the number of slow diffusing ions
κ'	Reaction constant
κ^{-1}	Debye screening length
γ_{GB}	Grain boundary energy
γ_{GF}	Grain-film interface energy
γ_{LV} [J/m^2]	Surface tension of the liquid
γ_{SL} [J/m^2]	Solid-liquid interfacial energy
γ_{SV} [J/m^2]	Free surface energy of solid
$\varepsilon_i(0)$	Zero frequency dielectric permittivities of phase i
ε_j	Dielectric permittivity of the *j*th phase
ε_o	Permittivity of free space
ψ_s	Surface electrostatic potential
ψ	Dihedral angle
Π_{ADS}	Solute adsorption force
Π_{EDL}	Electrical double layer force
Π_{HB}	Hydrogen bonding force
Π_{ST}	Steric disjoining forces
δ	Boundary core width
$\nu_{e,ceramic}$ **[1/s]**	Absorption frequencies in the UV
$\nu_{e,metal}$	Metal plasmon frequency
$\nu_{rot,ceramic}$ **[1/s]**	Absorption frequencies in the IR
θ	Contact angle
a	Corresponds to the heat of melting of the intergranular phase
b_L	Bjerrum length

c_m	Solubility of the diffusing atoms in the particle
e	Electron charge
f	Site factor reflecting the density of boundary core sites associated with high jump probabilities
h	Intergranular film thickness
$i\zeta$	Imaginary frequency
k_β	Boltzmann's constant
l	Thickness of the liquid later between grains
m	Electron mass
n_e	Free electron density
n_i	Refractive index of phase i
r	Particle/pore radius
r_d	Radius of the drop contact area with the substrate
z	Ion charge
zJ [10^{-21}J]	Zeptojoules
A	Constant
C_∞	Bulk solute concentration
C_l	Solubility of diffusing element in liquid film
D_{GB}	Boundary self diffusion coefficient
D_l	Diffusivity of bulk ions in the liquid layer at grain boundary
F_p	Particle/pore drag force
F_{Debye}	Debye force
F_i	Driving force of i
F_{Keesom}	Keesom force
F_{LD}	London dispersion force
F_{rep}	Repulsive force
F_{vdW}	van der Waals force
$\bar{G}$	Average grain size
H	Hamakar coefficient
H_d	Drop height
I_{imp}	Intensity of impurity signal
M_i	Mobility of i
P	External force
Pc	Capillary force

R_0	Drop radius
T	Absolute temperature
V_{el}	Characteristic electronic absorption frequency in the ultraviolet
V_i	Velocity of i
W_{ad}	Work of adhesion
Z	Atomic Number

AEM	Analytical Electron Microscopy
AES	Auger Electron Spectroscopy
AFM	Atomic Force Microscopy
BF	Bright Field
BSE	Backscattered Electron
CA6	Calcia-Hexaluminate $CaO•6(Al_2O_3)$
CCD	Charge Coupled Device
CUS	Coordinatively Under-Saturated
DPI	Dots per Inch
EBSD	Electron Backscattered Diffraction
EDL	Electrical Double Layer
EDS	Energy Dispersive Spectroscopy
EELS	Electron Energy Loss Spectroscopy
FEG	Field Emission Gun
FIB	Focused Ion Beam
HIP	Hot Isostatic Pressing
HRSEM	High Resolution Scanning Electron Microscopy
HRTEM	High Resolution Transmission Electron Microscopy
IGF	Intergranular Films
IR	Infrared
LD	London Dispersion
PEELS	Parallel Electron Energy-Loss Spectroscopy
PVD	Physical Vapor Deposition
SAD	Selected Area Electron Diffraction
SE	Secondary Electron
SEM	Scanning Electron Microscopy
STEM	Scanning Transmission Electron Microscopy

TEM	Transmission Electron Microscopy
TEOS	Tetraethylorthosilicate - $Si(OCH_2CH_3)_4$
UHR	Ultra High Resolution
UHV	Ultra-High Vacuum
UV	Ultraviolet
vdW	van der Waals
VEELS	Valence Electron Energy Loss Spectroscopy
WDS	Wavelength Dispersive Spectroscopy
XPS	X-ray Photoelectron Spectroscopy
XRD	X-ray diffraction
ZAF	Z - Atomic number, A -Absorption, and F - Fluorescence)

Understanding the properties of metal-ceramic interfaces is of scientific and technological importance. Such interfaces are found in oxide scales formed on metals [1], metal-ceramic joins [2,3], bonding of ceramic parts [3-5], metal-ceramic composites [6,7], electronic packaging systems, catalyst support [8], thin film technology [9], and more. The metal-ceramic interface has a crucial role in determining the mechanical and functional properties of the system.

To understand the forces acting at an interface, a number of parameters should be considered: the structure and properties of the bulk metal and ceramic, the structure of the interface, impurities or dopants in the bulk materials that may segregate at the interface, and possible reaction products at the interface.

Some interfacial thermodynamic properties may be determined through measurement of interfacial energy and adhesion. These can be obtained from sessile drop experiments [10] and measurement of dihedral angles at metal-ceramic triple junction boundaries [11].

The information obtained by these methods is not complete without precise monitoring of the atmosphere during the experiment, and analysis of the resulting interfacial structure and chemistry at the atomistic level. Of particular importance is the partial pressure of oxygen ($P(O_2)$), since even a very low $P(O_2)$ has a dominate role in interface reactions, and on surface and interface energies [12,13]. Impurities or additives in the starting materials tend to segregate at grain boundaries, and in ceramic systems with low solubility levels these are known in some cases to form thin equilibrium amorphous films [14-18].

The formation of intergranular films at ceramic interfaces has been the subject of intense study [19]. Equilibrium intergranular films are unique in that they are above levels that are considered to be segregation, but at the same time, they are not a bulk phase. There are attempts to describe the films in terms of multilayer adsorption [20], but these have not yet been developed to a level that predicts the observed behavior at internal interfaces in ceramic systems. The model explaining the equilibrium film

thickness is based on colloid-like force balance [15]. This approach is based on a balance between attractive van der Waals forces and repulsive steric forces leading to an *equilibrium* thickness (and thus the use of the term equilibrium films or amorphous equilibrium films). This model is lacking, in that it is not able to predict the conditions leading to the formation of the films. Molecular dynamics simulations of film behavior have been performed, but these are still in a very early stage, and give only a limited insight regarding film stability and mechanisms of formation [21,22].

In a recent study of alumina matrix composites, infiltrated with liquid Cu, Scheu *et al.* [23] detected amorphous films at interfaces between Cu and α-Al_2O_3. While all the Cu-Al_2O_3 interfaces investigated by Scheu *et al.* showed the presence of thin amorphous films, the nature of the process used to form the composite led to the question whether the films formed at equilibrated metal-ceramic interfaces, or if they formed as surface films prior to infiltration with liquid Cu. Since equilibrium amorphous surface films exist [24], this is not a trivial issue, and thus remains an open question regarding the existence of equilibrium amorphous films at metal-ceramic interfaces. The goal of the present work is to establish the stable existence of amorphous films at metal-ceramic interfaces. This was performed by preparing controlled alumina specimens reinforced with Cu or Ni particles to which predetermined amounts of glass formers were added, and through wetting experiments of the same metals on sapphire in the presence of anorthite glass.

Engineering in Ceramics edited by Taketo Sakuma, Laurel M. Sheppard, and Yuichi Ikuhara, Publihed by the American Ceramic Society, 427-444, (2000)

21. S. Blonski, S. H. Garofalini, "Atomistic Structure of Calcium Silicate Intergranular Films in Alumina Studied by Molecular Dynamics Simulations", *J. Am. Ceram. Soc*., 80[8], 1997-2004 (1997).

22. D. A. Litton and S. H. Garofalini, "Molecular Dynamics Simulation of Calcium Aluminosilicate Intergranular Films on (0001) Al_2O_3 Facets", *J. Am. Ceram. Soc*., 83[9], 2273-2281 (2000).

23. C. Scheu, G. Dehm, and W. D. Kaplan, "Equilibrium Amorphous Silicon-Calcium-Oxygen Films at Interfaces in Copper-Alumina Composites Prepared by Melt Infiltration", *J. Am. Ceram. Soc*. 84[3] 623-630 (2001).

24. J. Luo, and Y. M. Chiang, "Existence and Stability of Nanometer-Thick Disordered Films on Oxide Surfaces", *Acta Mater*., 48, 4501-4515 (2000).

25. M. Rühle, "Structure and Composition of Metal/Ceramic Interfaces", *J. Eur. Ceram. Soc.* 16, 353-365 (1996).

26. M. W. Finnis,"The Theory of Metal-Ceramic Interfaces", *Journal of Physics: Condensed Matter*, 8, 5811-5836 (1996).

27. R. Benedek, A. Alavi, D. N. Seidman, L. H. Yang, D. A. Muller, and C. Woodward, "First Principles Simulation of a Ceramic/Metal Interface with Misfit", *Phys. Rev. Lett.*, 48[15], 3362-3365 (2000).

28. I. G. Batirev, A. Alavi, M. W. Finnis, and T. Deutsch "First-Principles Calculations of the Ideal Cleavage Energy of Bulk Niobium(111)/α-Alumina(0001) Interfaces", *Phys. Rev. Lett.*, 82[7], 1510-1513 (1999).

29. A. Hashibon, J. Adler, M. Finnis, W. D. Kaplan, "Ordering at Solid-Liquid Interfaces Between Dissimilar Materials", *Inter. Sci.*, 9, 175 (2001).

30. A. Hashibon, J. Adler, M. Finnis, W. D. Kaplan, "Atomistic Study of Structural Correlations at a Liquid–Solid Interface", *Computational Mater. Sci.*, 24, 443 (2002).

31. L. E. Murr, "Interfacial Energetics in Metal-Metal, Metal-Ceramic, Metal-Semiconductors, and Related Solid-Solid and Liquid-Solid Systems", in Materials Science Research vol, 14, Surfaces and Interfaces in Ceramic and Ceramic-Metal Systems, Edited by J. Pask and A. Evans, Plenum Press, 107-119 (1981).

32, G. Levi and W. D. Kaplan, "Aluminium-Alumina Interface Morphology and Thermodynamics from Dewetting Experiments", *Acta Mater.*, 51, 2793–2802 (2003).

33. G. Levi, C. Scheu, and W. D. Kaplan, " Segregation of Aluminium at Nickel-Sapphire Interfaces", Segregation of Aluminium at Nickel-Sapphire Interfaces", *Inter. Sci*., 9, 213–220, (2001).

34. F. Ernst, "Metal Oxide Interfaces", *Mater. Sci. Eng*., R14[3] 97-156 (1995).

35. S. Jiao, M. L. Jenkins, and R. W. Davidge, "Interfacial Fracture Energy-Mechanical Behaviour Relationship in Al_2O_3/SiC and Al_2O_3/TiN Nanocomposites", *Acta Metall.*, 45[1], 149-156 (1997).

36. B. K. Hodgson, and H. Mykura, "Torque Terms and Grain-Boundary Energy Measurement", *J. Mater. Sci*, 8, 565-570 (1973).

37. A. G. Evans and M. Rühle, "Microstructure and Fracture Resistance of Metal-Ceramic Interfaces", in *Materials Interfaces* ed D. Wolf and S.Yip Chapman & Hall, London, 654-661 (1992).

38. Don. M. Lipkin, J. N. Israelachvili, and D. R. Clarke, " Estimating the Metal-Ceramic Van Der Waals Adhesion Energy", *Phil. Mag. A*, 76[4], 715-728 (1997).

39. F. Didier and J. Jupille, "The Van Der Waals Contribution to the Adhesion Energy at Metal-Oxide Interfaces", *Surf. Sci.*, 314, 378-384 (1994).

40. F. Ernst, O. Kienzle, M. Rühle, "Structure and Composition of Grain Boundaries in Ceramics", *J. Euro.Ceram. Soc.*, 19, 665-673 (1999).

1. LITERATURE SURVEY

In this chapter, the criteria for defining an intergranular film as an *equilibrium* film are reviewed. Models and experimental evidence of their stability are introduced, and key parameters defining the film properties are discussed. Since the observation of intergranular films at metal-ceramic interfaces is new, the review focuses mainly on films found in ceramic systems.

1.1. Metal-Ceramic Interfaces

Studies of metal-ceramic interfaces primarily focus on the bonding between the two dissimilar materials. This is evaluated through a variety of experimental and theoretical methods. From sessile drop experiments, thermodynamic properties can be measured, such as the interfacial energy and work of adhesion between the two materials. Mechanical testing of the bonded samples can yield the work of fracture. The two measurements are correlated, but differ since heat dissipation and deformation that occur during mechanical testing are not taken into account in the work of adhesion. Alternatively, a growing number of theoretical works attempted to calculate the metal-ceramic interfacial properties from first principles models, but these are still at an early stage and were applied only to very well defined interfaces [25-28]. Some work has been carried out using molecular dynamics simulations, but these are lacking for need of good potentials to describe the complex interaction at the interface [26,29,30]. However, marked improvement in analytical microscopy techniques is now providing high-spatial resolution information (structural and compositional) from interfaces, enabling a quantitative comparison to the developing models [9].

1.1.1. Interface Adhesion and Energy

The experimental measurement of solid-liquid interface energy is usually performed by sessile drop experiments [10,31], and use of Young's equation: (Figure 1a):

$$\textbf{(1)} \qquad \gamma_{SL} = \gamma_{SV} + \gamma_{LV} \cos\theta$$

where γ_{SV} is the surface energy of the solid, γ_{LV} is the surface tension of the liquid, γ_{SL} is the solid-liquid interfacial energy, and θ is the contact angle between the liquid drop and the substrate. The contact angle can be measured *in-situ* during the experiment, and the liquid vapor energy can be measured simultaneously by applying the Laplace equation to a drop large enough for the gravitational force to be significant in determining the drop's curvature [10]. The solid-vapor energy has to be provided from other experiments for the absolute interface energy to be determined. This description of interfacial energy measurement is applicable to experiments where the substrate cannot be deformed and diffusion of the substrate is negligible, but this is not always the case for high temperature wetting [11]. When dealing with molten metal on a ceramic substrate the temperatures are such that diffusion and/or solution-precipitation are no longer negligible and can occur. These conditions lead to the formation of small ridges at the triple junction shown in Figure 1b,c [11]. This means that to fully characterize the drop it is not enough to measure the macroscopic contact angle, but rather a cross-section of the specimen has to be prepared [32,33]. The force balance for this geometry is described by the following relationship [11]:

$$\textbf{(2)} \qquad \frac{\sin\phi_s}{\gamma_{lv}} = \frac{\sin\phi_l}{\gamma_{sv}} = \frac{\sin\phi_v}{\gamma_{sl}}$$

where ϕ_s, ϕ_l, and ϕ_v are the equilibrium dihedral angles in the solid, liquid and vapor, respectively. A similar relation can be used to determine the relative interface energies from TEM analysis of the dihedral angles [34,35].

When dealing with solids the anisotropy of the surface energy is important and can result in considerable error in the energy measurements if the torque term is not taken into account [34,36]. This error can be reduced if enough measurements are taken and averaged [36].

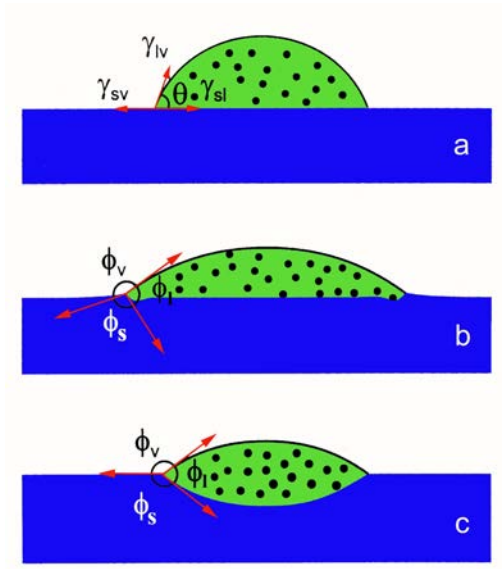

Figure 1. Schematic drawing of a sessile drop profile and the geometric parameters a) for low temperature or short treatment time, b) formation of a small ridge, c) a fully equilibrated particle/drop.

The work of adhesion (W_{ad}) of the interface can be calculated from the Dupré equation:

$$\textbf{(3)} \qquad W_{ad} = \gamma_{LV} + \gamma_{SV} - \gamma_{SL}$$

By combining the Dupré equation with Young's equation the work of adhesion can be measured within one experiment through the contact angle and the surface energy of the drop:

$$\textbf{(4)} \qquad W_{ad} = \gamma_{LV}(1 + \cos\theta)$$

This is especially important since the atmosphere used for the experiments and any impurities in the specific system used (equipment and materials) may result in considerable changes in the surface energy of the drop and substrate [12,13]. This may be further complicated due to possible variation in the local atomistic structure at the interface and its chemical composition.

1.1.2. Interface Structure and Chemistry

Understanding the relationship between processing and properties, with the structural and chemical features of metal-ceramic interfaces is becoming increasingly important as the requirements in applications demand control "down to" atomistic levels (e.g. electronic devices). At the atomistic level, the interfacial energy and adhesion are a measure of the bonding at the interface. The bonding could be separated into different contributions of ionic, covalent and van der Waals interactions [37-39]. In general bonding of two different phases having different crystal symmetries, structure, and lattice parameters, results in structural and chemical defects at the interface. Structural defects take the form of: steps, misfit dislocations, lattice dislocations, and others, while chemical defects include reaction products, chemical gradients, segregation, and *intergranular films* [37].

Two of the more common methods to investigate the interfacial structure at the atomistic level are high resolution transmission electron microscopy (HRTEM) and scanning transmission electron microscopy (STEM) [25,40-42]. Combining these two methods with analytical measurements using energy dispersive spectroscopy (EDS) and/or electron energy loss spectroscopy (EELS) provide a powerful tool for the investigation of the structure and chemistry of the interfaces. In a nice review by Rühle [25] extensive results obtained using these methods on two metal-ceramic interfaces (Nb-Al_2O_3 and Cu-Al_2O_3) are presented.

1.2. Equilibrium Amorphous Films

1.2.1. Characteristics of Equilibrium Amorphous Films

Microstructural features characterizing amorphous equilibrium intergranular films include a constant film thickness of the order of 1nm, which extends along the grain boundaries or interfaces (which may reach microns in length) [15,43]. The film composition is often based on some oxide combination that includes a glass network former such as SiO_2. Three general cases can be described that lead to incorporation of impurities which can result in glass formation (and the potential formation of equilibrium intergranular films); additives used in liquid phase ceramic sintering; glass ceramics in which the material is prepared by controlled but incomplete crystallization of the glass; and impurities found in the starting material. The inability of ceramic materials to incorporate impurities or additive cations into their structure (low solubility limit), leads to the formation of secondary phases in polycrystalline ceramics [43,44]. It has been experimentally observed that the film thickness strongly depends on the composition and type of sintering additives (or impurities), while it weakly depends on the total amount of the additives in the bulk [14]. In systems having intergranular films, low-angle grain boundaries and low-energy ("special") grain boundaries are found to be "dry" (without a film). The films are limited to high angle grain boundaries, since for these boundaries the total boundary energy (including the film) is less than the “dry” grain boundary energy (see Figure 2) [40].

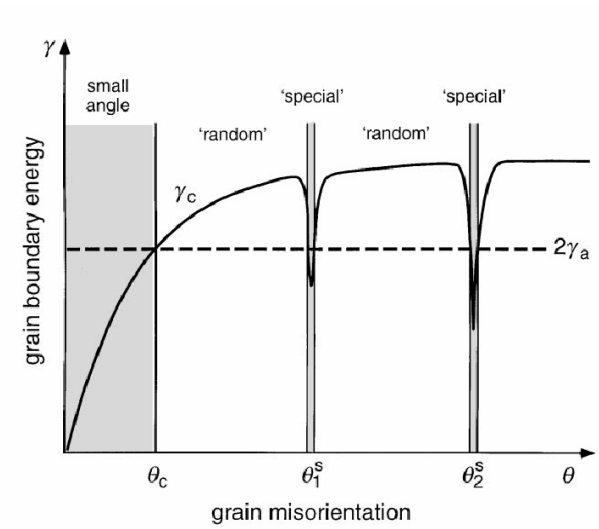

Figure 2. Schematic graph of the grain boundary energy versus misorientation angle. The solid line represents the energy of a dry interface while the dashed line is of a boundary containing an intergranular film [40].

A straight horizontal line (constant energy) usually represents the grain boundaries' energy in the presence of an equilibrium film. However, this description is not accurate for an anisotropic material (e.g. alumina), since its general grain boundaries in the presence of a liquid phase tend to facet to lower energy planes, and for different angles the configuration will differ.

1.2.2. Microstructural Evolution and Intergranular Films

The driving force for grain growth in the absence of strain is the reduction of the overall surface energy of the system. An extensive amount of published work has been addressed to fundamental questions concerning the mechanisms involved in grain growth and grain boundary mobility, and the influence of small levels of impurities and/or the presence of secondary phases [45-48]. The basic mechanisms governing the thermodynamic and kinetic factors are well understood.

Commercial ceramics typically contain hundreds of ppm's, if not more, of impurities. The combined effect of crystalline anisotropy and the presence of impurities, even at ppm levels, can affect these mechanisms significantly [45,46,49]. This can be through formation of a solid solution with the matrix and the introduction of defects, thereby modifying diffusion rates within the solid. Segregation to interfaces will affect their mobility (solute drag) and determine whether pores or secondary phases present in the material will be occluded during grain growth process [45-47].

At steady state, with boundaries moving with a velocity V_b, the driving force is exactly balanced by the total drag force on the boundary F_p . This drag force can have several different components: intrinsic drag from diffusion rate limitations, drag from a solute, which interacts with the boundary, and drag from pores or precipitates (Zener drag) [45,48].

The formation of intergranular films may have an important effect on mircostructural evolution. Their presence can enhance mass transport at grain boundaries, and lead to rapid coarsening. For thin films (~1nm) the process will be dependent on the reaction

rate at the film-grain interface [45]. Formation of thicker intergranular films will result in dependence on the diffusion rate through the film.

Less work has been focused on the combined effect of intergranular films in the presence of secondary phases.

1.2.3. Systems with Intergranular Films and their Role

Over the years, a large number of materials have been found to contain intergranular films. One of the most studied systems is silicon nitride [50]. The intergranular films in Si_3N_4 result in high creep rates at elevated temperatures due to grain boundary sliding [51]. Other systems include zinc oxide varistors [52], ruthenate resistors [53] (where the electrical properties are controlled by the film thickness), SiC composites [54], zirconia ceramics, glass ceramics, nuclear waste ceramics, and alumina [14] (where the films influence wear behavior [55] and high temperature creep).

Clarke [15] was the first to suggest a model explaining the formation of equilibrium intergranular films.

1.3. Modeling of Equilibrium Amorphous Films

Different approaches have been used to model the behavior of intergranular films. The first reviewed here is by Clarke, and is a continuum, statistical approach [15,56]. The second model is an atomistic approach, by means of molecular dynamic simulations [21,22,57]. Other works, discuss the stability of intergranular films through thermodynamical considerations [58-60].

1.3.1. Clarke's Model

Clarke modeled the force balance at grain boundaries in alumina, based on colloid-like behavior [15,56]. The forces are dominated by long-range attractive van der Waals (vdW) forces (F_{vdW}) and steric disjoining forces (Π_{ST}), which act to establish the equilibrium intergranular film thickness. In general there may be other forces involved including: electrical double layer (Π_{EDL}), solute adsorption (Π_{ADS}), hydrogen bonding (Π_{HB}), capillary forces (P_c), and applied external forces (P) [15]:

$$\textbf{(5)} \qquad P + P_c + F_{vdw} + \Pi_{EDL} + \Pi_{ADS} + \Pi_{HB} + \Pi_{ST} = 0$$

Van der Waals-Dispersion Forces

The key component in the model is the van der waals force originating from dipole interactions. It can be divided into three additive terms [61]:

$$\textbf{(6)} \qquad F_{vdW} \approx F_{Keesom} + F_{Debye} + F_{LD}$$

F_{Keesom} – the Keesom force is the force arising from the interaction of two permanent dipoles. This force depends on the relative orientation of the dipoles. As the temperature rises, thermal induced motion causes disorder in the mutual alignment of the dipoles and this force vanishes. F_{Debye} – the Debye force results from permanent dipole interaction with an induced dipole. This force is active at high temperature and always results in an attractive force, but requires the presence of one permanent dipole. The last term F_{LD}, is the London dispersion (LD) force, and its source is in interatomic bonds in atoms and molecules inducing dipole moments in nearby interatomic bonds. For induced dipole interactions to develop, each grain should have comparable characteristic frequencies. The resulting LD force will be a summation of the contributions of each interatomic bond that can find a corresponding bond of comparable frequency in the adjacent grain. According to Lifshitz theory for LD forces [62], the most effective induced dipoles have frequencies in the visible through the vacuum ultraviolet spectral range [61]. The higher frequency limit is due to the finite speed of electromagnetic wave propagation and is termed as the retardation effect. For example, at a wavelength of 12nm (~100eV) the critical retardation length is 0.2nm. The lower limit is determined by the thermal frequency, below which there is loss of the coupling.

The LD force is an attractive force between two objects, and is always present in any system. When more than two phases are involved, the resulting force can be repulsive. The general form of the London dispersion force for the parallel slab geometry seen in Figure 3 is [15,63]:

$$\textbf{(7)} \qquad \Pi_{DISP}(h) = \frac{\hbar}{8\pi^2 h^3} \int_0^\infty \sum_{n=1}^{\infty} \frac{1}{n^3} \left[\left(\frac{\varepsilon_\alpha - \varepsilon_\beta}{\varepsilon_\alpha + \varepsilon_\beta} \right) \cdot \left(\frac{\varepsilon_\gamma - \varepsilon_\beta}{\varepsilon_\gamma + \varepsilon_\beta} \right) \right]^n d\zeta$$

where $\varepsilon_j = \varepsilon_j(i\zeta)$ is the dielectric permittivity of the jth phase as a function of the imaginary frequency $i\zeta$, h is the film thickness or distance between the boundaries, and $\hbar$ is Planck's constant divided by 2π (wave function).

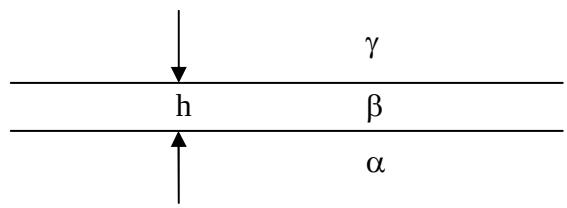

Figure 3. Intergranular phase β of thickness h between phases α and γ.

Clarke considered a simple case of a grain boundary (with the same phase on both sides of the film) taking the first term of the summation.

$$\textbf{(8)} \qquad \Pi_{DISP}(h) = \frac{\hbar}{8\pi^2 h^3} \int_0^\infty \left[\left(\frac{\varepsilon_\alpha - \varepsilon_\beta}{\varepsilon_\alpha + \varepsilon_\beta} \right) \right]^2 d\zeta = \frac{H_{\alpha\beta\alpha}}{6\pi h^3}$$

where H is the Hamakar coefficient. Calculation of the Hamaker coefficient using this expression demands the integration over all the frequencies of the dielectric permeabilities of both phases (or in a more general case of all the phases involved in the film formation), data that is not available for most materials. This difficulty may be over come by using the Tabor-Winterton approximation or the Ninham-Parsegian representation (the latter being more accurate) [15,61,63-66]. Both methods take advantage of the relation between the dielectric and optical properties of the material.

The Hamaker coefficient represents a force constant for the attractive or repulsive van der Waals interaction between bodies. For the case of a grain boundary, this force will always be an attractive force.

Structural Disjoining Force

The model assumes that the film, unlike a bulk amorphous material, is not totally a random structure but exhibits some order close to the interface with each grain. This order is induced on the liquid due to the ordered structure of the adjacent grains [63,67]. The ordering in intergranular films has not yet been experimentally proven, but ordering of a liquid on a crystal has been experimentally observed by x-ray scattering of liquid Ga on diamond [68], and by high resolution electron microscopy of liquid xenon confined in aluminum cavities [69]. Such ordering was also predicted by molecular dynamics simulations [29,30].

For simplicity, Clarke used a mean field approach with a scalar quantity η(x) to describe the ordering parameter in the film [15]. Starting from the Cahn-Hillard equation, which expresses the free energy density of a liquid and minimizing the energy of the film as a function of the thickness, the following equation was obtained for the disjoining force:

$$\textbf{(9)} \qquad \Pi_{ST} = \frac{-a\eta_0^2}{\sinh^2(-h/2\xi)}$$

where h is the thickness of the film, ξ is the correlation length, and $a\eta_0^2$ represents the free-energy difference between the intergranular films (IGF) liquid with and without structural ordering. η_0 is the degree of epitaxy (1 being totally ordered, and 0 completely random) and the constant "*a*" corresponds to the heat of melting of the intergranular phase. The correlation length physically represents the effective distance of atomistic interaction. Higher values of the correlation length will result in an increase in the repulsive force.

Electrical Double Layer

Clarke also examined the effect of a disjoining force resulting from the formation of an electrical double-layer [56]. Two alternative approaches were considered, the weak overlap approach (10), and the case of a charged surface, which is compensated by a

counter ion build up in the liquid (11). In the latter the disjoining force depends only on the counter-ion concentration at the mid-plane ρ_o.

$$\textbf{(10)} \qquad \Pi_{EDL} = \frac{16k_BT}{z^2\pi b_L}\left(\tanh\frac{ze\psi_s}{4k_BT}\right)\kappa^2 e^{-\kappa h}$$

$$\textbf{(11)} \qquad \Pi_{EDL} = k_BT\rho_0 = 2\varepsilon\varepsilon_0\left(\frac{k_BT}{ze}\right)^2 K^2$$

where k_BT is the Boltzmann constant times the absolute temperature, z is the ion charge, b_L is the Bjerrum length (the distance between two protons in a dielectric medium at which their electrostatic energy equals their thermal energy, experimental values are in the range of 0.5-10nm). ψ_s is the electrostatic potential on the surface of the grains, and κ^{-1} is the Debye screening length (equation (10) is valid for $\kappa h > 1$). ε is the dielectric constant of the intervening medium, ε_o is the permittivity of free space, and *K* is a constant that can be evaluated by the boundary conditions.

The two approaches represent the minimum and maximum values expected for the electrical double layer force (weak overlap approach and charged surface, respectively) [56,63].

Capillary Forces

Clarke *et al.* [15,56] did not introduce an explicit expression for estimating the capillary force acting at the interface. From his analysis of the force balance in the case of an attractive vdW force and a repulsive electrical double layer force, a capillary force of a few MPa was needed to equilibrate a 2nm thick film. This value, Clarke *et al.* claimed, was in the range of the expected forces (1-10MPa) based on unpublished work by Shaw. According to Kingery [70] these values represent pressures expected at the initial stages of liquid phase sintering in alumina with silicate additions.

The capillary force results from the surface wetting of two solids by a liquid and the formation of a meniscus bridging between them. When this liquid-bridge forms a negative curvature, a pressure difference bringing them together is obtained, which is termed the Laplace pressure [47,71]. However, reports on equilibrium intergranular

films are mostly in dense materials and therefore no such meniscus is present within the fully dense bulk material. Therefore, calculating the pressure should be approached in a different way. The same effect can occur in the case of two different immiscible liquids [71].

Evaluation of the Force Balance

Clarke evaluated the forces acting at a grain boundary for a number of different materials using two approaches. In both cases he assumed no external forces were applied (P=0), and ignored possible contributions of a hydrogen-bonding term.

The first calculation was carried out using only two terms: an attractive van der Waals force and a steric repulsive force [15]:

$$\textbf{(12)} \qquad \frac{H_{\alpha\beta\alpha}}{6\pi h^3} - \frac{-a\eta_0^2}{\sinh^2(-h/2\xi)} = 0$$

The parameters used to evaluate the steric force were based on the assumption of a SiO_2 intergranular film. The values obtained from the calculations were in good agreement to the experimental measurements of the intergranular films thickness.

In the second case the repulsive steric force was replaced by a disjoining force arising from an electrical double layer (using equations 10 and 11) and a contribution of an attractive capillary force [56]:

$$\textbf{(13)} \qquad \Pi_{EDL} = \frac{16k_BT}{z^2\pi b_L}\left(\tanh\frac{ze\psi_s}{4k_BT}\right)\kappa^2 e^{-\kappa h} = P_c + \frac{H_{\alpha\beta\alpha}}{6\pi h^3}$$

$$\textbf{(14)} \qquad \Pi_{EDL} = k_BT\rho_0 = 2\varepsilon\varepsilon_0\left(\frac{k_BT}{ze}\right)^2 K^2 = P_c + \frac{H_{\alpha\beta\alpha}}{6\pi h^3}$$

The conclusion based on these calculations was that the force resulting from the presence of an electrical double layer may very well contribute to the total disjoining force acting between the grains in the liquid phase, but it is unlikely to be the only repulsive force.

1.3.2. Molecular Dynamic Simulation of Intergranular Films

The atomistic structure and stability of intergranular films in alumina was investigated by Garofalini *et al.* using molecular dynamics simulations [21,22]. The first study was based on calcium silicate films (*without* Al_2O_3), which were placed between two (Al terminated) alumina basal (0001) surfaces. The positions of the atoms in the alumina were fixed and only the glass atoms were allowed to move. The simulations consisted of five different glass compositions: 0%, 12%, 22%, 32%, and 41% mol. of CaO, and four different thicknesses. The thicknesses were determined using different amounts of atoms in the film (300, 450, 600, and 750).

The results showed that ordered cage-like structures formed at the glass-alumina interfaces (Figure 4). The observed ordering was slightly different than that considered by Clarke's model [15]. The cage structure is created by the bonding of bridging oxygen atoms (Si-O-Al). Coordinatively under-saturated (CUS) aluminum atoms at the alumina terminated plane bonded through the oxygen with the Si in the IGF. These Al atoms sit at tetrahedral sites with a coordination number of 4. The addition of Ca, stabilized these cage structures by interacting with the CUS oxygen atoms at the alumina surface rather than the Si atoms from the film. The stability of the IGF was assessed by the system's energy. It was observed that an increase in the film thickness contributed only very slightly to the stability, while an increase in Ca concentration had a much more pronounced effect (see Figure 5). Ca segregation to the alumina surface reaches a saturation point with increase in Ca concentration, which is very reasonable, but the authors do not clearly state what the segregation value actually is.

In fracture experiments performed on the *simulated* samples, two modes of fracture were observed: along the column oxygen bonds (the film/alumina interface), or through the intergranular film. The initial increase in the Ca concentration resulted in a strength increase. This was attributed to the Ca stabilizing effect on the cage structure (Si-O-Al bonds). With higher additions of Ca, the SiO_2 network structure was disrupted by the formation of non-bridging oxygen atoms, which decreased the overall strength.

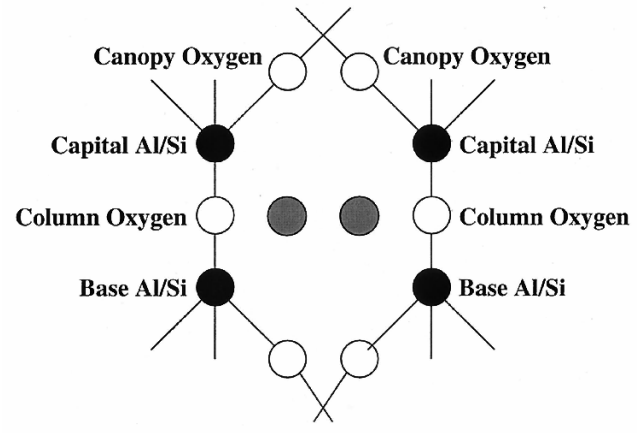

Figure 4. Idealized schematic drawing of the cage-like structure that forms at the alumina-glass interface. ((–) bonds, (O) oxygen ions, and (●) cations). The alumina terminating plane is not shown, but is at the bottom of the figure [22].

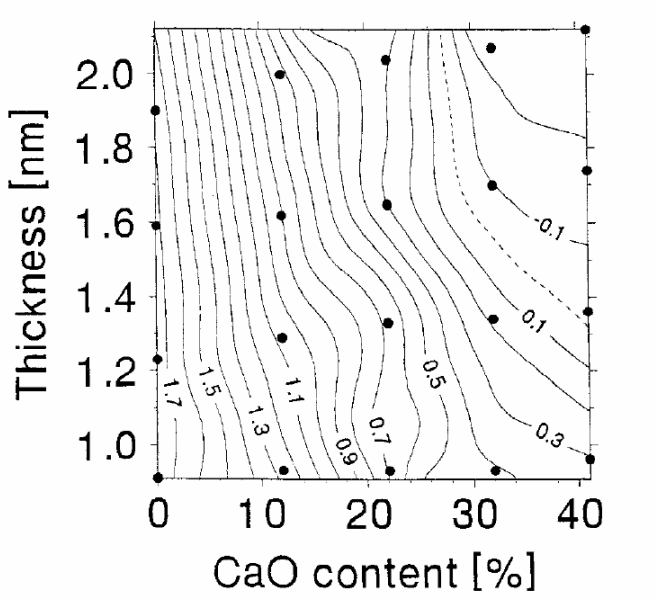

Figure 5. Dependence of the $CaSiO_3/Al_2O_3$ interface energy on the intergranular film thickness and composition [21]. The filled circles represent the simulated samples (the energy is given in arbitrary units).

The glass film did not contain alumina, which is not a realistic assumption, since the alumina and the glass form a reactive system. In a following study [22] two different alumina basal plane terminations were considered: oxygen and aluminum terminated. This work examined six different glass compositions including those with different alumina contents, and one composition of anorthite glass ($2SiO_2$-CaO-Al_2O_3), which is the low temperature eutectic phase of the system (see Table 1). At high temperatures the alumina atom positions were fixed (like before), but once the samples were quenched

below the melting temperature of alumina, the atoms were released to allow for relaxation and interchange of species with the IGF.

As in the first study, cage-like structures formed at the interface and were stabilized by Ca. No Al atoms were found within the cages in the simulations of the films that included Ca, confirming the findings from the previous work (Figure 4). Radial distribution analysis of the average Ca coordination number in the cage and the IGF gave values of ~6.5 and 5 respectively. The coordination number of Ca in CaO is 6 [72], which is probably the reason for the preferred segregation at these sites. However, the segregation of Ca to these sites is limited by charge compensation. Theoretically, the Ca can occupy a maximum of 50% of the terminating base sites for charge compensation reasons, and in fact it was found on average to occupy 51.7% of the sites in the 25% CaO glass for the aluminum terminated system; but not in all cases were the sites completely filled. The possible reasons for that are the need for charge compensation in the presence of Al atoms in the glass, and for kinetic reasons such as the difficulty to occupy additional sites once initial sites are filled. In simulations using film compositions containing Al_2O_3 and no CaO, the Al atoms were found in sites within the cages. The coordination number of oxygen atoms around aluminum ions for those sites was ~4.7 relative to ~4.2 in the glass. Aluminum ions are most stable at octahedral sites and therefore these sites are preferred relative to the glass tetrahedral sites, but they still result in a local violation of charge neutrality. This was seen to cause a disorder in the cage structure for the composition without CaO. The Si ions are more rigid with regard to their coordination number, which means the driving force for their occupation of sites inside the cages is lower than for Al and Ca.

In the oxygen terminated surfaces, the base sites were occupied by cations from the IGF forming cage structures. In the absence of Ca the cage structures were distorted with both Si and Al at base sites and some of the termination sites were occupied by Al. Once the Ca was added the relative amount of Al in the termination sites decreased.

Table 1. Glass compositions (in moles percent) used for molecular dynamic simulations [22].

#	SiO_2	Al_2O_3	CaO
1	100	0	0
2	87.5	0	12.5
3	75	0	25
4	75	25	0
5	62.5	25	12.5
6	50	25	25

If the structure and coordination number of the cations in the oxides composing the IGF are considered based on their stable crystalline structure, their tendency for occupying the available sites as observed in the simulation are reasonable.

1.4. Experimental Observations

(Experimental results and attempts to apply the models qualitatively and quantitatively).

Applying the model is not a simple task since the parameters needed in order to perform the calculations are not readily available (the dielectric permeabilities for all frequencies). Using the dependence of the optical properties on the electronic structure of the materials, the components needed for the calculation of the LD interaction can be obtained. The electronic structure of a material represents the interatomic ionic, covalent, and metallic bonds it forms. This information is found in the electron density of states and can be measured through experimental methods giving information on the optical properties of the material such as reflectivity, and energy-loss (performed on the surface) [61]. Through these measurements, both the real and imaginary optical components can be obtained.

The exact composition of the films is not easily measured due to the nanometer ranged width of the films, and therefore the properties of the films are not accurately known.

Based on a simplified assumption that the film consists only of SiO_2, the parameters needed for the model were estimated [15,50]. The use of scanning transmission electron microscopy (STEM) together with electron energy loss spectroscopy (EELS) now enables measurement of the valence EELS (VEELS) at a very high lateral precision of more than 0.5nm [61,73,74]. Measurement of accurate spectral data allows direct determination of the indices of refraction, from which the Hamaker coefficient for the dispersion force (via Lifshitz theory) can be calculated [61]. The difficulty with these measurements is they involve line-scans over the grain boundary or interfaces, and demand very stable working conditions to insure the measurements are performed at the precise point of interest (the interface, without drift). Another difficulty is the measurement of the elemental distribution within the film, and segregation to the crystal-film interface.

1.4.1. Film Thickness Dependence on Chemistry

In a work carried out by Tanaka *et al.* the dependence of the film thickness on Ca content was studied [50]. High purity Si_3N_4 samples were prepared by hot isostatic pressing at 1950°C with Ca doping of: 0, 80, 220, and 450 ppm. At all general grain boundaries analyzed, intergranular films were observed. Furthermore, different Ca contents resulted in changes in the film thickness. A minimum in the film thickness was observed for 80 ppm Ca doped samples (see Figure 6). No dependence of the IGF thickness on the grain boundary misorientation was found. Tanaka explained these findings qualitatively in terms of Clarke's model. In the case of the undoped sample there should not be any contribution from an electrical double layer (EDL). The thickness in this case will be controlled by a balance of the attractive van der waals force and the repulsive steric force. The addition of Ca to the intergranular film has two effects: modifying the silica network structure and adsorption to the interface with the grain surface forming an EDL. Based on their results they assumed that small amounts of Ca additions (80 ppm) modified the silica network, thereby decreasing the steric force and reducing the film thickness. With larger additions of Ca, an EDL formed leading to an increase in the film thickness. A semi-quantitative analysis was performed, based on the force balance in the undoped case using the equilibrium film thickness measured experimentally, and the correlation length was calculated. The

correlation length obtained was 0.22nm, which is a physically reasonable value. The only problem with the calculation is that the samples were prepared by hot isostatic pressure using 170MPa which was not accounted for in the calculations, and once this value is introduced the correlation length decreases by an order of magnitude (~0.024nm), which is not realistic.

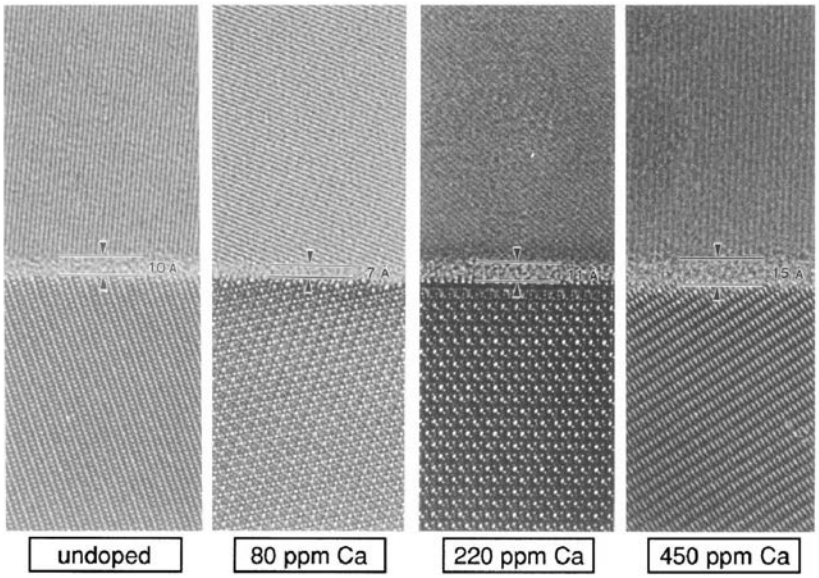

Figure 6. HRTEM images of grain boundaries in Si_3N_4 doped with different amounts of Ca (a) 0 ppm Ca, (b) 80 ppm Ca, (c) 220 ppm Ca, (d) 450 ppm Ca. An IGF can be seen in all the boundaries [50].

In a later study Gu *et al.* [75] performed HRTEM and STEM investigations on the same samples. Thickness measurements of the films using HRTEM confirmed the original findings. Chemical analysis of the grain boundary films showed an increase in the Ca content with an increase in the bulk Ca doping level for the 0, 80, 220ppm doped samples. However, no difference in Ca excess was found between the 220 and 450ppm doped samples. Both these samples showed a larger standard deviation in the thickness and chemical measurements compared with the rest of the samples. The Ca seemed to reach a saturation concentration in the film at a doping level of around 220ppm. The extra amount of Ca was observed to concentrate at the mouth of some of the films with the glass pocket.

The authors suggested that the large deviations may indicate two groups of films, with a difference in composition and thickness. This was not experimentally confirmed.

1.4.2. Film Thickness Dependence on Temperature

In a paper by Chiang *et al.* [53] the effect of Ti doping on the properties of ceramic composite resistors was studied. The resistor composite was based on ultra-fine ruthenate conductor particles in a silicate glass. It was found that the ruthenate particles agglomerate and thin equilibrium films are formed at the interfaces between the particles. Samples with 0, 4.28, and 8.44 mole % of TiO_2 were prepared and heat treated at temperatures between 600°C - 900°C. An increase in the resistance was measured for all the compositions treated at temperatures between 700°C - 750°C. For each temperature, the resistance increased with TiO_2 content. Film thickness measurements performed on the samples prepared at a temperature of 750°C (showing the highest resistance) indicated the film thickness increased with the TiO_2 composition. The increase in resistivity was explained by the reduction of the ruthenium solubility in the film together with film thickening following the TiO_2 additions. Both these effects lead to higher insulation between the grains. Analysis of the Ti:Si ratio in the grain boundary film, and the glass matrix, relative to the nominal ratio introduced into the samples showed an increase of the ratio in the intergranular films and a decrease in the glass matrix. The Ti and Si excess and Ti:Si ratio in the films were found to depend on the temperature in the samples prepared at 750°C and 850°C (for the samples with 8.44 mole % TiO_2). It is evident from these results that the film thickness was ultimately controlled by the temperature.

A similar behavior was reported in a recent study by Kleebe *et al.* [76], where a wetting-dewetting transition was observed in SiAlON. Samples quenched from 1380°C to room temperature were found to retain intergranular amorphous films, while samples slowly cooled to room temperature show no sign of IGF. In the latter samples, TEM analysis revealed the presence of mullite at the triple grain boundaries. It appears that the formation of the second phase during cooling to room temperature altered the glass composition, leading to "dry" (no IGF) grain boundaries.

In both of the papers reviewed in this section, it is obvious that temperature is critical, in that it governs the reactions kinetics, whether it is nucleation of a second phase (mullite), or the equilibrium composition of the film, which leads to alteration in the film thickness.

1.4.3. Film Thickness and Grain Orientation

In the original model proposed by Clarke [15], dependence of intergranular film thickness on grain boundary misorientation was not taken into account, since such a dependence was not observed in general grain boundaries. The only qualitative consideration of the grain boundary orientation was for low energy boundaries where the film was absent (Figure 2).

In a study by Knowles *et al.* [54] a dependence on the grain orientation was observed for an interphase boundary. In a Si_3N_4 – SiC composite with BN contaminations resulting from processing, intergranular films were found at SiC - h-BN (h-hexagonal) interfaces. Interfaces with a (0001) BN terminating plane had a thickness of 1.2±0.1nm, while at an interface with a 68° inclination relative to the (0001) plane the film thickness was ~ 0.85nm.

Using a generalized form of Clarke's model, Knowles managed to quantitatively model the three-phase system together with the orientation dependence (anisotropy effects). The Hamaker coefficient for the three-phase interface was based on an approximation given by Israelachvili (15) [63]:

(15) $$H_{132} \approx \frac{3}{4} k_B T \left(\frac{\varepsilon_1(0) - \varepsilon_3(0)}{\varepsilon_1(0) + \varepsilon_3(0)} \right) \left(\frac{\varepsilon_2(0) - \varepsilon_3(0)}{\varepsilon_2(0) + \varepsilon_3(0)} \right) + \frac{3\pi\hbar\nu_{el}}{4\sqrt{2}} \frac{\left(n_1^2 - n_3^2\right)\left(n_2^2 - n_3^2\right)}{\left(n_1^2 + n_3^2\right)^{1/2}\left(n_2^2 + n_3^2\right)^{1/2}\left\{\left(n_1^2 + n_3^2\right)^{1/2} + \left(n_2^2 + n_3^2\right)^{1/2}\right\}}$$

where $\varepsilon_{1(0)}$, $\varepsilon_{2(0)}$, and $\varepsilon_{3(0)}$ are the zero frequency dielectric permittivities of phases 1-3 (3 being the film), n_1, n_2, and n_3 are the refractive indices in the visible range, $\hbar$ is Planck's constant, and V_{el} is the characteristic electronic absorption frequency in the ultraviolet (assumed to be the same in all the phases based on an analysis by Israelachvili). From equation (15) it can be seen that the LD force may result in repulsion, if the change in properties (n and ε) across the interface behave in a monotonic fashion (for example $n_1>n_2>n_3$, since it will result in a negative value).

The anisotropy in the properties of the terminating plane was treated using a dielectric tensor. This treatment of the anisotropy resulted in modification of equation (15) where instead of n_1 and ε_1 an effective value was introduced ($n_{eff}(\theta)$ and $\varepsilon_{eff}(\theta)$) which was orientation dependent (basically a function of the misorientation angle θ). Using this

modified model it was possible to calculate the film thickness for the different terminating planes of the BN (the effect of anisotropy was treated only for the BN).

The dependence of the film thickness is probably more evident in the case of an interface between dissimilar materials, since then anisotropy of one of the phases will be more pronounced.

1.4.4. Film Thickness and Pressure

Jin *et al.* [51] reported the influence of tensile creep experiments on intergranular films found at commercial Si_3N_4 grain boundaries. The Si_3N_4 was processed with 4wt% Y_2O_3 as a sintering aid. The Y_2O_3 additions resulted in formation of secondary phases. Samples before and after creep testing at a temperature of 1430°C, load of 40MPa for 690h and a total strain of 0.65% were investigated for changes in the thickness of the intergranular films (only at the Si_3N_4 grain boundaries). The uncrept sample had a measured mean IGF thickness of 0.72±0.13nm, after creep a bimodal distribution was obtained, with a lower thickness of 0.52nm and a higher thickness of 1.33nm (Figure 7). The authors suggested two possible explanations for this. The first was inhomogeneous chemical composition distribution in the sample because of crystallization or oxidation during the high-temperature creep. This was ruled out, since the same thickness differences were observed at different locations checked within the sample. Therefore, they concluded the bimodal thickness distribution was a result of differences in the local stress applied on the films. According to the paper, viscous flow models predict that intergranular glass redistributes such that a third of the grain boundaries receive the amorphous phase from the remaining two thirds as a result of stress distribution during creep. The statistics from the film thickness measurements in the reported work support this assumption, since a larger number of grain boundaries possessed a thinner IGF.

There are other works in which modification of the IGF thickness was observed following the application of external forces. Complete *drying* of the grain boundaries was obtained in ZnO samples doped with Bi after applying pressures of up to 1GPa during HIP processing [52]. These findings indicate the importance of taking into account external pressure when calculating the equilibrium IGF thickness.

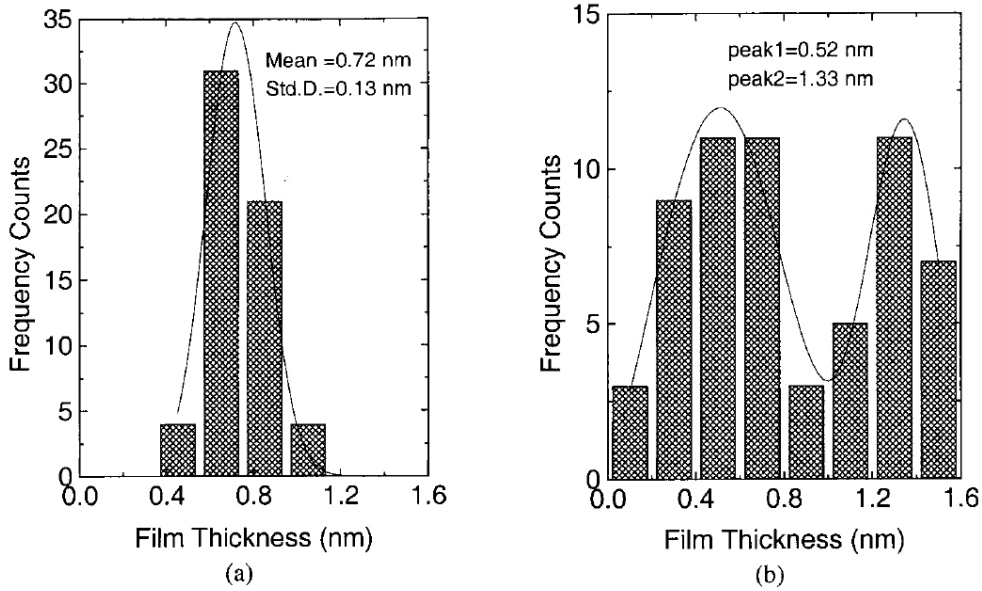

Figure 7. Experimental values of intergranular film thickness at Si_3N_4 grain boundaries (a) before creep and (b) after creep testing at 1430°C, 40MPa for 690h [51].

1.4.5. The Stability of Intergranular Films

The stability of the intergranular films will depend on whether their formation represents a minimum energy configuration or only a local minimum. Ackler and Chiang [77,78] examined the stability of retained IGF in the TiO_2 and SiO_2 system. They first examined a TiO_2 single crystal coated by high purity SiO_2 [77]. The sample was heat treated at 1600°C, 50°C above the eutectic temperature of the system to obtain a single-phase liquid and then quenched to retain the glass. It was then reheated to a temperature 100°C below the eutectic temperature to allow the liquid to crystallize. TEM analysis of the sample revealed a quartz crystal formed over the TiO_2 substrate but a 1.5nm thick intergranular film was retained at the interface. It is important to emphasize that in this system and configuration, for the film to crystallize there is no demand for dewetting involving long-range transport; the quartz crystal phase forms one of the interface boundaries. In the second study [78] two polycrystalline TiO_2 were used. The first was a pure dense polycrystalline TiO_2, which was dipped into a TiO_2-SiO_2 melt for 1 hour at a temperature of 1600°C. In the second, TiO_2 powder was coated by a SiO_2 layer and then sintered to obtain dense samples; these were held at a temperature of 1600°C for 5 and 10 minutes and then quenched. HRTEM analysis of the grain boundaries showed that in the pure sample dipped in the TiO_2-SiO_2 melt penetration occurred only through triple junction grain boundaries. In only 2 out of 50

boundaries analyzed a film was observed. In the samples sintered with an initial SiO_2 coating ~35-45% of the grain boundaries possessed IGFs. These samples showed a very wide variation in the film thickness, 0.6-5nm and 0.6-7nm, for the samples held for 5 and 10 minutes, respectively. Ackler and Chiang concluded from these results that the formation of the films is route dependent and there exists a barrier in the energy between the two states. Kinetic reasons for the differences were ruled out since the grains in the sample sintered with glass coarsened by a factor of 10 during the sintering process. The fact that not all the grain boundaries contained a film was explained as following: these interfaces were formed prior to the SiO_2 coating and sintering (in the raw powder, as agglomerates). The variation in the film thickness was regarded as an indication of structural or energetic differences in interfaces rather than incomplete evolution towards equilibrium (under the conditions of the experiments). However, when comparing the two works by Ackler and Chiang, a few questions need to be considered. Could the fact that the heat treatment was performed above the eutectic temperature rather than below be a factor in the wide film thickness distribution. Is it possible that kinetic factors are involved in the glass penetration to the grain boundaries, and longer treatments at 1600°C would result in higher ratios of boundary penetration?

This raises the question of what leads to film formation? However, this question is still unresolved. Clarke's model only offers a tool to predict the equilibrium thickness of the film, based on force balance. Cannon *et al.* [20] suggested multilayer adsorption as a possible mechanism leading to the film formation. It is important here to differentiate between two cases in which intergranular films are found. The first (reviewed in the present work) is characterized by a thickness of a few atomic layers (few nm), and is governed by a force balance described by Clarke's model [15]. The second is of microscopic dimensions (1μm range) and is a result of wetting of the matrix by the second phase. In this case, the film thickness depends on the amount of the second phase, these films have mostly been investigated in metallic systems. The latter can be explained based on classical thermodynamic considerations [79,80]. In such cases, the liquid penetrating the grain boundaries will be essentially the same composition as the bulk liquid.

1.4.6. Cu-Alumina Interfaces

In an investigation of Cu-alumina composites by Scheu *et al.* [23], intergranular films were found at the Cu-alumina interfaces. Two samples, with open pore diameters of 0.2μm and 0.8μm (otherwise the same), were analyzed. The samples were infiltrated with liquid Cu at a temperature of 1300°C [81]. Similar to Knowles *et al.* [54], a dependence of the film thickness on the alumina surface termination was observed. For (0001) alumina terminating planes, the film thickness was measured to be ~1nm in both samples. However, for the $(\bar{1}012)$ alumina terminating planes the measured thickness was 0.4nm and 0.6nm for the 0.2μm and 0.6μm pore size samples respectively. No films were found at alumina grain boundaries. Scheu's study is the first work reporting the presence of intergranular films at *metal-ceramic* interfaces.

These findings raise the question whether equilibrium intergranular films can form at metal-ceramic interfaces? The nature of the process used to form the composite, and the fact that surface films are known to exist [54] leads to the question whether these films are a result of surface films formed on the alumina prior to infiltration of the Cu? If equilibrium intergranular films at metal-ceramic interfaces are stable, how does this affect metal ceramic processing, and the interfacial energy and adhesion? Could a force balance, based on Clarke's model, be applied for the case of a metal-ceramic interface?

1.5. Research Goals

The formation of intergranular films at ceramic-ceramic interfaces has drawn considerable attention in past years. Their stability has been experimentally investigated for a wide range of materials and conditions. However, the stability of intergranular films at *metal-ceramic* interfaces has not yet been systematically addressed.

The equilibrium thickness of intergranular films is indicative of a force balance at the interface. Clarke's model of a balance between attractive van der Waals forces and various repulsive forces is widely accepted today, as the basis for explaining the film equilibrium thickness in ceramic systems. The question is whether a similar force balance is formed at *metal-ceramic* interfaces.

Very limited focus has been given to the influence of intergranular films on interfacial energy. The film presence was described simply in terms of interfacial energy reduction as $\gamma_{GB} > 2\gamma_{GF}$ (where γ_{GB} is the grain boundary energy and γ_{GF} is the grain-film interface energy). This treatment does not consider the fact that the two interfaces are in very close proximity and interact.

The primary goal of this research is to conduct a basic scientific study to determine whether intergranular equilibrium films are stable at *metal-ceramic* interfaces. This question is addressed both experimentally and theoretically. The structure, chemistry, and energy of *metal-ceramic* interfaces in the presence and absence of intergranular equilibrium films are addressed. The systems chosen for the investigation are Cu-Al_2O_3 and Ni-Al_2O_3 systems, due to the fact that the films were first observed in the Cu- Al_2O_3 system, while the Ni-Al_2O_3 serves as a comparison. At the same time, these systems are relatively well documented in the literature, and are of technological interest. The experiments are based on microstructural observations of metal-alumina composites, and sessile drop experiments of the same metals on sapphire to study the wetting behavior in the presence of glass.

The significance of this research is the development of a basic understanding of intergranular equilibrium films at *metal-ceramic* interfaces; a topic that has been almost entirely ignored in the past.

2. EXPERIMENTAL METHODS

This chapter describes the sample preparation methods and the characterization techniques. The first part of the research was performed using metal-alumina composites. This approach enabled the investigation of the influence of glass additives on the micro-structural evolution of metal-alumina composites and intergranular films stability. Model experiments were later performed using sessile drop experiments of the same types of metals (as used for the composites) on sapphire substrates.

2.1. Ultra-High Vacuum Wetting Furnace

Performing reliable wetting experiments requires precise monitoring of the working conditions, which include temperature, pressure and partial pressure of gases present during the experiment [12,13]. The wetting experiments in this study were performed in a dedicated wetting furnace (Figure 8).

This system enables *in-situ* characterization of the contact angles during high temperature (up to 1800°C) sessile drop experiments. The samples are placed on a stage with a diameter of 2.54cm. The furnace heater is located within the center of the chamber and is provided with tungsten heat shields, which screen the heated area from the surrounding chamber, and reduce heat loss during the experiment. The whole heater assembly is connected to a vertical lift that can be moved without opening the chamber. Wetting is monitored through a quartz window of the UHV chamber and a slit located at the side of the heater that may be opened during the experiments. A rotating platform is located within the chamber and can hold up to four samples. The different samples are changed using a manipulator arm, which allows for up to four sessile drop experiments without breaking vacuum.

Images of the sessile drops were initially (Cu on sapphire) recorded using a CCD camera (Avenir, Japan, with 150 DPI resolution) connected to a computer. Latter experiments were recorded with a digital camera (Nikon E995, 300 DPI with Nikon telescopic lens x3).

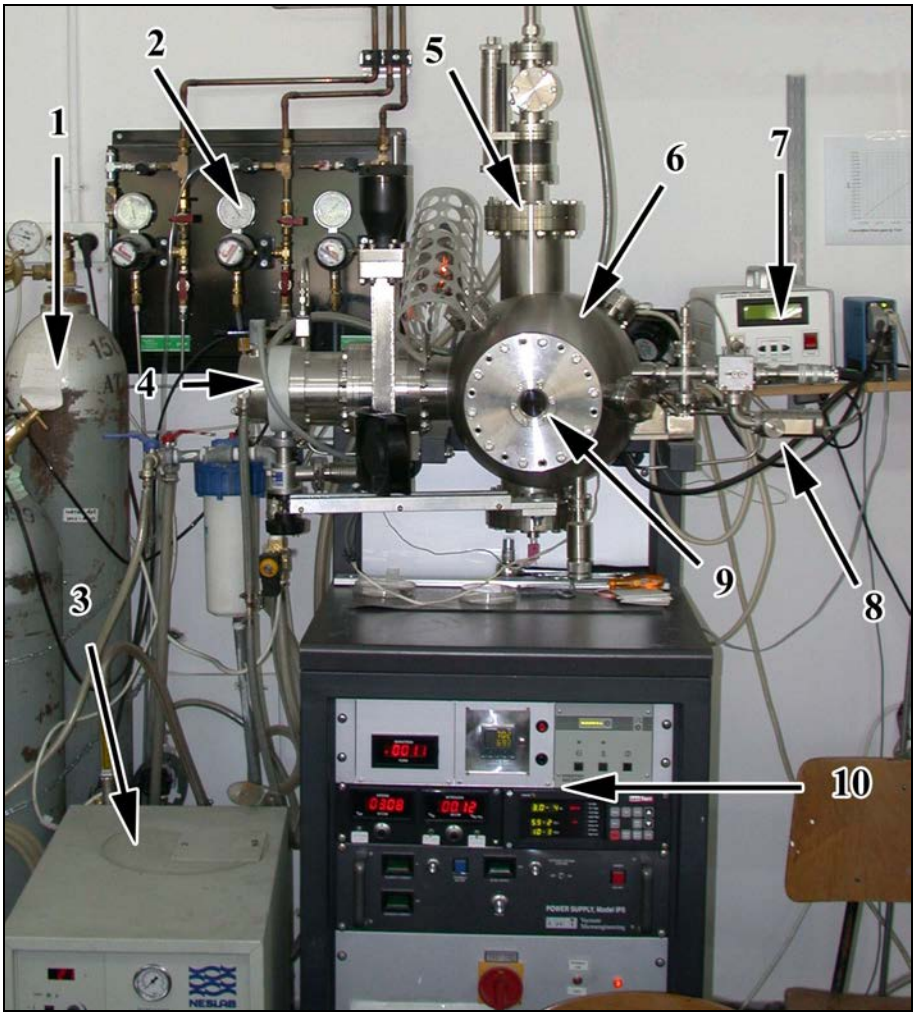

Figure 8. UHV wetting furnace used for sessile drop experiments. 1. gas tanks, 2. gas flow control and pressure gauges, 3. water cooling system, 4. turbo-molecular pump, 5. heater lift system, 6. UHV chamber, 7. Zirconia oxygen analyzer meter, 8. gas flow valve, 9. quartz window for in-situ contact angle recording, 10. furnace control system.

The furnace can be operated at total pressures ranging from 1000 Torr down to 10^{-10} Torr. The furnace has two *in-situ* gas monitoring systems. A micropole residual gas analyzer (RGA, Ferran Scientific, USA) equipped with an atomic mass spectrometer. This system can monitor the partial pressure of up to 8 different gases at the same time (pressures down to 10^{-9} Torr and after an upgrade performed in the system down to 10^{-11} Torr), but is limited to total pressures below 10^{-3} Torr. Using low pressures while performing high temperature wetting experiments results in a very high evaporation rate of the liquid metal drops. In order to reduce the evaporation rate by increasing the total pressure, and still be able to monitor the oxygen partial pressure, a zirconium oxygen analyzer (Rapidox 2000 Oxygen Analyzer, Cambridge Sensotec, UK) was installed with an oxygen detection limit of $<10^{-15}$ Torr.

2.2. Processing of Metal-Al_2O_3 Composites

The requirement from the composite materials was to obtain a significant number of equilibrated metal-alumina interfaces, for independent measurements of the intergranular film behavior. To obtain this a specific processing procedure was designed. The Cu-Al_2O_3 and Ni-Al_2O_3 nanocomposites were prepared using high purity alumina powder (Sumitomo AKP 50), to which predetermined amounts of dopants were added. The glass forming additives were added in two stages. A SiO_2 coating was introduced on the alumina powder during the slip preparation. This was achieved by adding (4.2g) tetraethylorthosilicate (TEOS - $Si(OCH_2CH_3)_4$) into the water based alumina slip (100g of Al_2O_3). Mixing the TEOS with water results in the following sol-gel reaction:

(16) $$Si(OCH_2CH_3)_4\ (liq.) + 2H_2O\ (liq.) \Rightarrow SiO_2\ (solid) + 4HOCH_2CH_3\ (liq.)$$

This leads to the formation of a thin SiO_2 coating on the alumina powder (Figure 9). The stoichiometry of the reaction requires two moles of water per mole of TEOS. In practice, this amount of water leads to incomplete reaction, therefore, a higher water ratio is required. The process can be accelerated by heating the solution. Mixing the TEOS and alumina water based slip provided a high ratio of water needed to speed up the reaction, and ultrasonic mixing (Model Vibra Cell 600, Sonics & Materials INC) was used at 25% power for 10min, providing additional heating of the mixture.

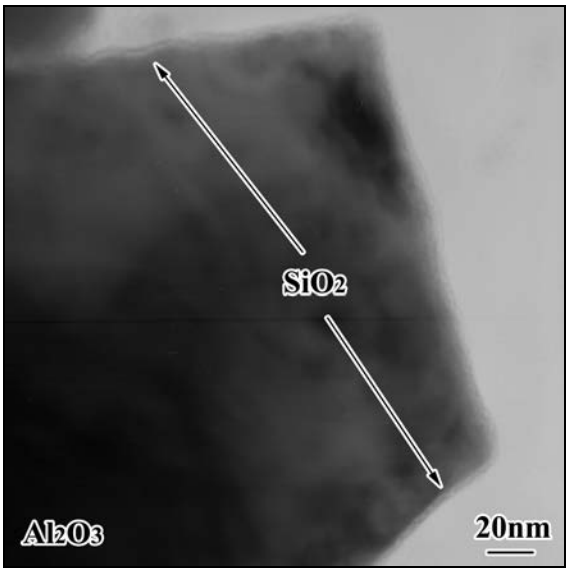

Figure 9. A bright field TEM micrograph of an alumina powder particle coated by SiO_2, using the sol-gel process.

The green alumina samples were prepared by pressure filtration using an Instron 1195. At first, a high bridge displacement speed was used, until the first sign of water emission was observed. The speed was then reduced to 2mm/min, which occurred at a load of ~1kN for specimens with a diameter of 4.4cm and ~1cm thickness. The bridge speed was further decreased, once the load began to show a sharp increase (~3kN), to 0.1-0.2mm/min. The force was allowed to reach a maximum load of 5kN which was then maintained for an additional 10min. The pressure applied on the samples under these conditions was 3.3MPa.

The samples were left to dry for two days in air and then fired at 900°C in air for 4 hours to obtain the minimum mechanical strength needed for further handling. Ca was then added by infiltrating the porous alumina with a water based solution of Ca-nitrate (water/Ca nitrate - 4/1.5 by weight). The infiltration process involves dipping the porous alumina green body into a metal-nitrate solution under low vacuum [6]. The samples were then dried and calcined at a temperature of 900°C for 2h. The metal-alumina composites were prepared in a similar manner adding Cu or Ni (water/Cu nitrate 10/7 by weight, water/Ni nitrate 2/1 by weight).

After infiltration the samples were dried and heat treated in a reducing atmosphere (Ar + 6% H_2) to obtain Cu or Ni metal particles [6]. Both composites were sintered in the UHV furnace (Figure 8). Sintering of the *Cu-alumina* composites was performed under a protective Ar atmosphere at a total pressure of ~10^{-3} Torr and a temperature of 1550°C for 4 hours (heating and cooling rates of 20° C/min). The partial pressures of O_2 ,H_2O, N_2 , Ar and CO_2 were monitored in-situ during the experiments, using a micropole residual gas analyzer. The $P(O_2)$ was measured to be lower than the detection limit ($<10^{-9}$ Torr). The *Ni-alumina* composites were sintered under an Ar protective atmosphere at a total pressure of 100 Torr at a temperature of 1500°C for 4 hours (heating and cooling rates of 20° C/min). The partial pressure of oxygen was monitored in-situ during the experiments, using a zirconium oxygen analyzer, and was below the detection limit ($<10^{-15}$ Torr).

2.3. Sessile Drop and Dewetting Experiments

The sapphire substrates for wetting and dewetting experiments with Cu were ground and polished to a surface roughness of less than 0.25μm. After polishing, the substrates were cleaned in acetone followed by ethanol absolute. To eliminate damage induced by the polishing process, the substrates were annealed at a temperature of 1600ºC in air for 2h. The wetting and dewetting experiments with anorthite and Ni were performed on sapphire substrate from GAVISH Industrial Technologies & Materials. Pure Ni (99.997 at.%) and Cu (99.997 at. %) (Johnson-Matthey, Materials Technology, U.K.) were used for the wetting experiments.

For dewetting experiments the substrates were coated with a 2μm layer of metal (Cu or Ni). The layers were coated by physical vapor deposition (PVD) in vacuum (10^{-6} Torr). The samples were heat treated in the same UHV furnace used to sinter the composites and conduct sessile drop experiments.

Anorthite (CaO-$2SiO_2$-Al_2O_3) for the wetting and dewetting experiments was prepared by ultrasonic mixing of 34g of Al_2O_3 powder (Sumitomo AKP 50) with 30.03g of $CaCO_3$, and 36.05g SiO_2 in 25g of H_2O. The paste was dried and then heat treated in air at a temperature of 1600°C for 4h to obtain anorthite glass. The process was conducted in an alumina crucible. Therefore, the alumina ratio used was slightly higher than the level required for anorthite, in order to minimize the amount of alumina take-up from the alumina crucible.

2.4. Characterization Methods

The microstructure and local chemistry of the sintered nanocomposites, and samples from wetting and dewetting experiments, was performed using X-ray diffraction (XRD), scanning electron microscopy (SEM), and transmission electron microscopy (TEM) techniques.

XRD measurements for phase identification of the composites were performed on polished samples in a conventional X-ray automatic powder diffractometer (PW-1820 goniometer, Philips, Eindhoven, Netherlands) with a C*u*Kα tube, operated at 40 mA and 40 kV. 2θ scans were acquired from 17° to 100° with a step size of 0.03° and exposure times of 10sec per step.

SEM was conducted on a FEI XL30 microscope equipped with energy dispersive spectroscopy (EDS) and wavelength dispersive spectroscopy (WDS) (Oxford Instruments, Oxford, England). High resolution SEM (HRSEM) was conducted on a LEO 982 Gemini microscope equipped with a field emission gun (FEG–SEM), EDS (Thermo Noran super-thin window Si(Li) EDS detector), and electron backscattered diffraction (EBSD) (Oxford Instruments, Oxford, England).

For the TEM studies, the samples were sectioned using a diamond-wafering disk followed by mechanical thinning to obtain 3mm diameter samples with a thickness of ~100μm. The samples were then mechanically dimpled and thinned by ion milling with Ar at 3-5 kV to perforation.

A detailed study of the microstructure of the specimen was carried out by conventional TEM. The chemical composition and structure of the phases and grain boundaries were analyzed by analytical TEM, scanning transmission electron microscopy (STEM) and high-resolution TEM (HRTEM). Conventional and analytical TEM were performed on a 200 kV microscope (Model 2000 FX, JEOL, Tokyo, Japan) equipped with an EDS (Model Link AN10000, Oxford Instruments, Oxford, England) and a parallel electron energy-loss spectrometer (PEELS) detector (Model 766, Gatan, Warrendale, PA). STEM was performed using a VG HB501 UX dedicated STEM with a beam diameter

of <1nm equipped with a Noran thin window Si(Li) EDS detector and a PEELS (Gatan 766). HRTEM was conducted using a 300 kV microscope (Model 3010UHR, JEOL, Tokyo, Japan) with a point resolution of less than 0.16 nm, and a 200kV microscope equipped with a field emission gun (Model 2010, JEOL, Tokyo, Japan) equipped with EDS (Oxford Instruments, Oxford, England).

Atomic force microscopy (AFM) was used to measure the surface roughness of the sapphire substrates before and after wetting experiments. AFM was conducted on a Park Instruments, Autoprobe CP, operated in both contact and tapping mode.

3. RESULTS

The main experimental results obtained in the present research are given in this chapter. The results are divided into three sections, according to the type of experimental method used to investigate the intergranular film behavior. The first are the metal-alumina composites, then the wetting samples of the same metals on (0001) sapphire, and finally dewetting experiments. Both wetting and dewetting experiments were performed in the presence and absence of an anorthite glass prepared specifically for these experiments.

Each section is subdivided into the general microstructural features, and the structural and analytical results obtained directly from the intergranular films.

3.1. Metal-Al_2O_3 Composites

The metal-alumina composites served as a comparison to the samples studied by Scheu *et al.* [23] to establish whether equilibrium intergranular films will form under conditions which ensure the possibility of the glass phase to stabilize. The Cu-alumina system was chosen, since the presence of intergranular films was first observed in that system by Scheu *et al.* [23]. Ni-alumina composites were included, to determine whether the phenomena is limited to Cu-alumina or occurs in other systems.

3.1.1. Cu-Al_2O_3 Composites

Phase Analysis and General Morphology

The aim of the present study was to investigate the formation of equilibrium intergranular films at *metal-alumina* interfaces and therefore it was important to avoid any oxidation of the metal or formation of aluminates. XRD phase analysis was performed to confirm that no reaction phases formed. XRD phase analysis performed on the undoped sample showed no reflections other than that of copper and alumina (see Figure 10a). However, the glass doped sample exhibited additional reflections, which were found to belong to $CaO{\bullet}6(Al_2O_3)$ (calcia-hexaluminate; CA6) (Figure 10b). Its presence was also confirmed by TEM analysis. Figure 11a, presents a TEM micrograph

of an alumina grain embedded within a CA6 grain. The CA6 phase was identified by both EDS and selected area electron diffraction (SAD) (Figure 11c,d).

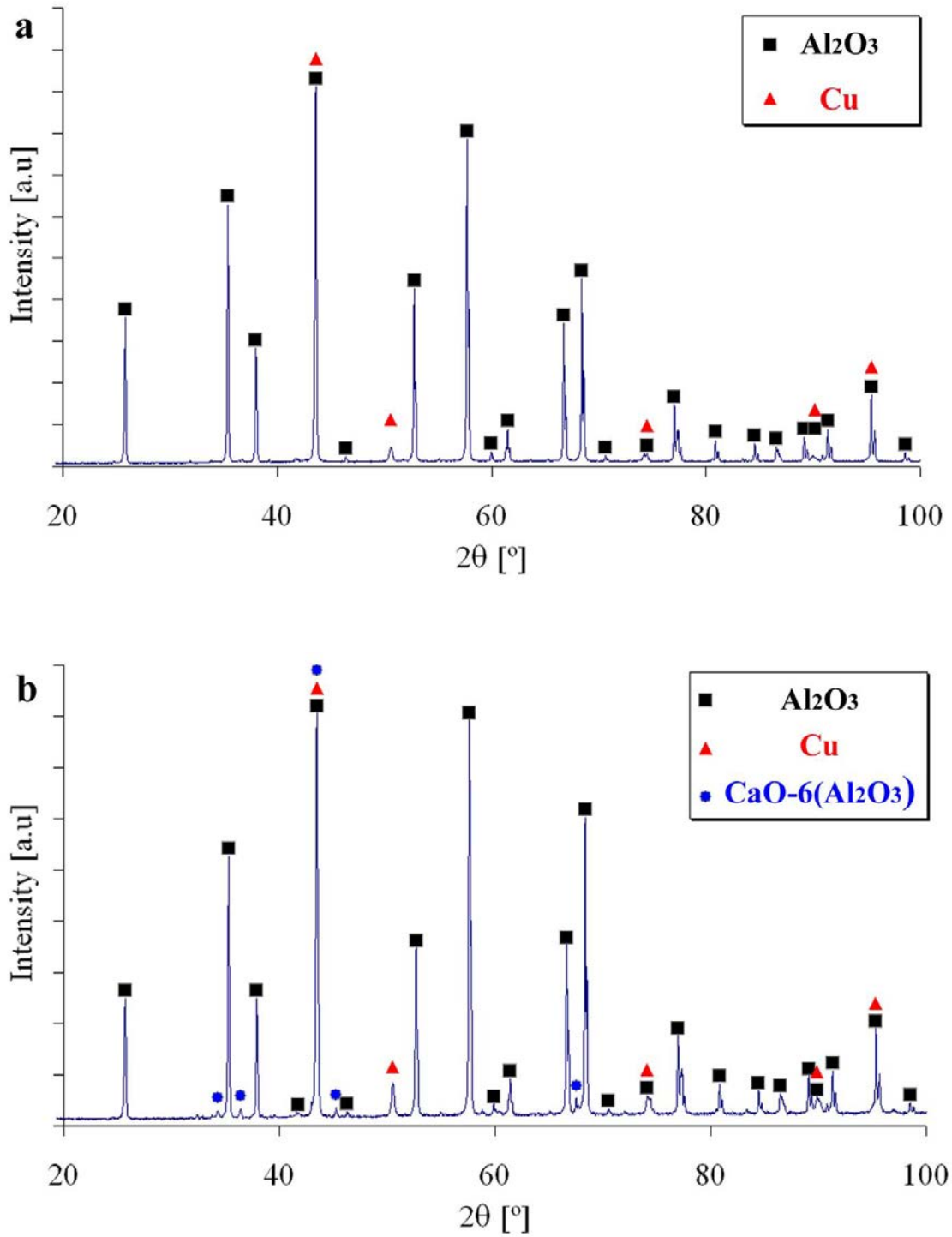

Figure 10. XRD pattern obtained from the a) Cu-alumina undoped sample. b) Cu-alumina glass doped sample.

The SAD pattern taken from the Cu and CA6 interface indicates the Cu (111) planes are parallel to the (0001) CA6 planes. Other interfaces found between Cu and CA6 did not share the same relative orientation. No reaction phases involving the Cu and alumina, or Cu oxides, were observed from the XRD results. This is in agreement with literature reports showing both thermodynamic calculations and experimental results that reaction produces are formed at partial pressures of oxygen above $5x10^{-5}$ Torr ($7x10^{-3}$ Pa) [82,83].

The dispersion of the copper particles in the doped sample was relatively uniform, except for a few areas where the copper did not penetrate. The areas not penetrated by Cu in the doped samples were probably a result of the process by which the glass additives were introduced, which blocked the pores between the alumina particles in some areas. Figure 12 presents a backscattered electron (BSE) SEM micrograph of the Cu alumina composites. Due to the higher Z value of Cu versus alumina, the Cu particles have a higher (brighter) contrast. The pores in the samples appear as dark spots in the image.

It can be clearly seen from Figure 12 that the Cu particles in the undoped sample are finer than in the doped sample, and that the doped sample has a higher level of porosity. The relative porosity and metal volume were estimated based on BSE SEM image analysis of the samples; from each sample 7-10 images were taken at a magnification of x1000 (image area ~150μm x 250μm) and at 20kV. The results of these measurements are given in Table 2. The values obtained for the Cu content are an over estimation due to the high energy used which yields a stronger contrast from Cu particles found under the surface of the sample.

Table 2. Relative porosity and metal volume measured from BSE SEM images of the samples. The measurement of the Cu was converted to at.% to compare to EDS measurements.

Sample	Porosity Vol. %	Cu Vol. %	Cu at. %
Undoped Pure Alumina	0.8 ± 0.3	-	-
Doped Alumina	3.7 ± 0.6	-	-
Undoped Cu-alumina	1.3 ± 0.4	4.2 ± 0.6	11.9 ± 1.8
Doped Cu-alumina	3.6 ± 0.6	3.5 ± 1.1	10.1 ± 3.2

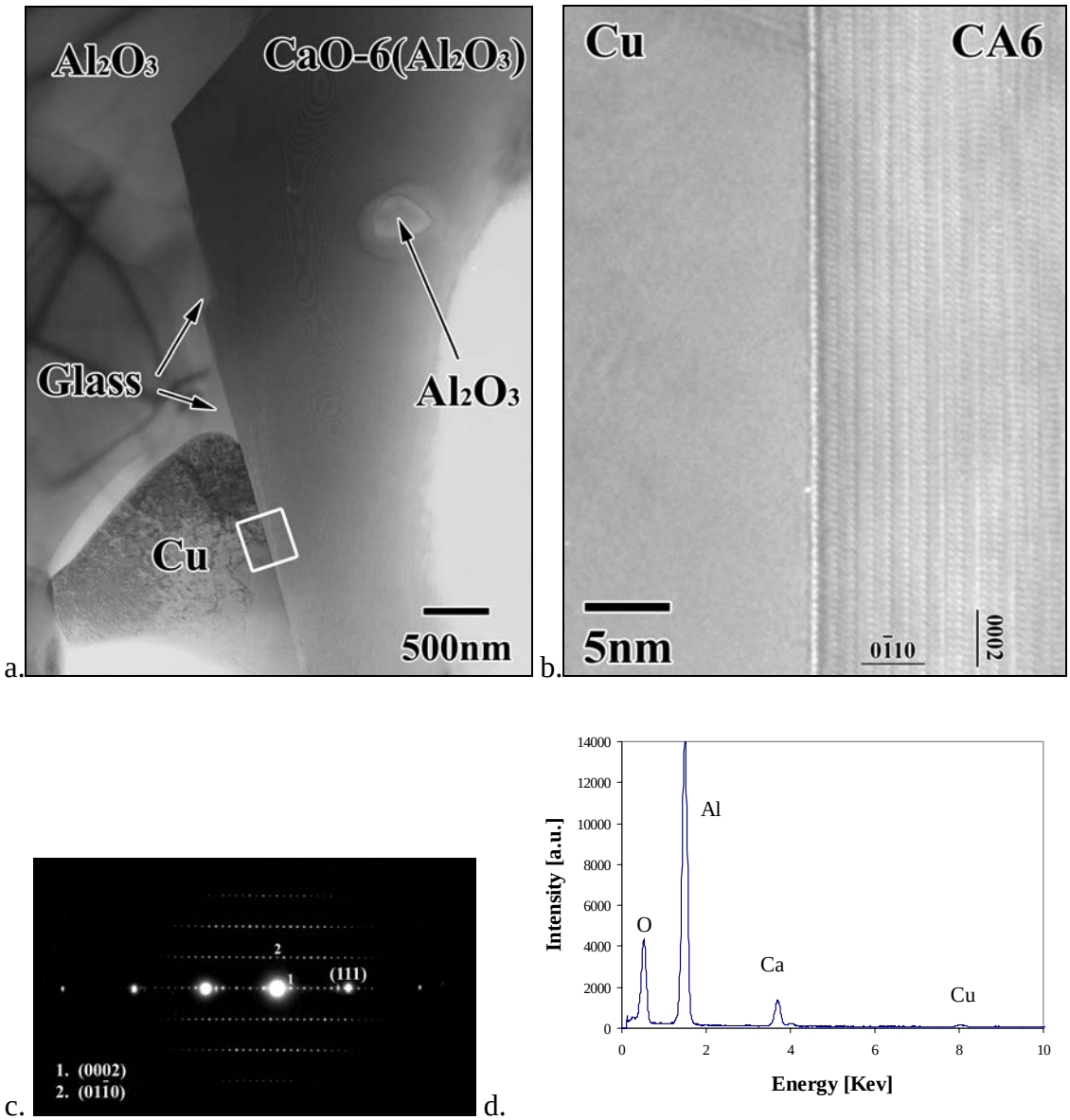

Figure 11. a) A bright field TEM micrograph of an interface between a Cu particle and a CA6 grain. The CA6 contains an occluded alumina grain. A high magnification micrograph of the Cu-CA6 interface is presented in (b) in the $[\bar{2}110]$ CA6 zone axes. (c) and (d) present the selected area electron diffraction pattern taken from the Cu-CA6 interface and EDS taken from the CA6 grain, respectively.

It should be emphasized here that the processing of the samples was not optimized, since the aim of the work was to investigate the metal-alumina interfaces. To obtain an improved microstructure requires ball milling of the slip to breakup residual agglomerates (this was avoided to reduce impurities), and a two stage firing process would have been used with a lower final temperature. In this work, high heating and cooling rates were used to minimize the influence of low temperature dwells.

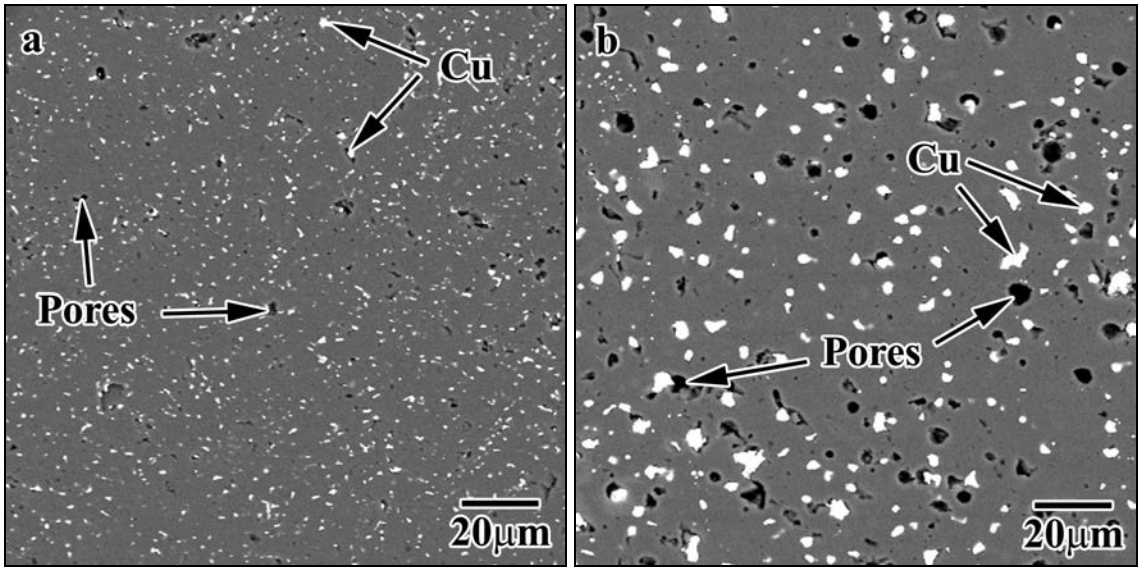

Figure 12. SEM micrographs taken in BSE mode showing the dispersion of Cu particles in the alumina matrix. a) undoped sample, b) glass doped sample.

Figure 13 presents secondary electron (SE) SEM micrographs of undoped and glass-doped Cu-Al_2O_3 composites, which serve to compare the alumina grain size and morphology. The SEM specimens for alumina grain size measurements were polished to 0.25μm and thermally etched at 1300°C for 2h under a protective atmosphere (Ar - 5%H_2). At this temperature the Cu is liquid and formed drops on the sample surface obscuring the alumina microstructure (see Figure 14). Therefore, the Cu was removed by a 5% HNO_3, 10% H_2SO_4 by volume water based etch.

An interesting feature seen in the micrograph of the doped sample (Figure 13b) is the material exuded from the grain boundaries following the thermal etching. Qualitative EDS measurements of the composition showed a higher Ca and Si content than the surrounding area. The difference in the alumina matrix grain size between the two samples can be seen from Figure 13a,b. The alumina grain size in the doped samples is on average 2-3 times larger than in the undoped sample. No secondary phase was observed at the grain boundaries of the undoped samples after thermal etching. It should be pointed out that although the doped samples contain a much higher amount of coarse porosity, their average grain size is larger than the undoped sample, indicative of the glass additives role in increased grain growth rate.

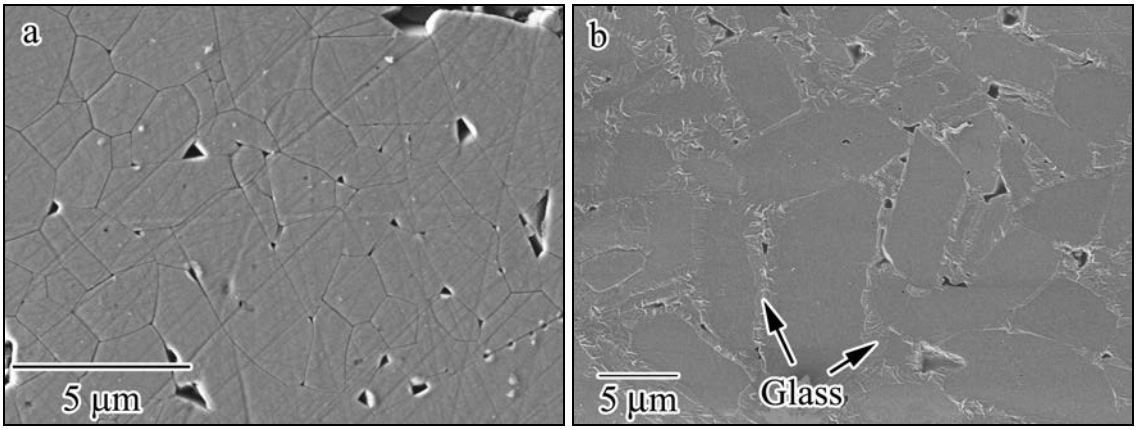

Figure 13. SEM (secondary electrons) micrographs showing the alumina grain size and morphology a) the undoped sample, b) the doped sample. The Cu is not visible in the images since it was chemically etched after thermal etching.

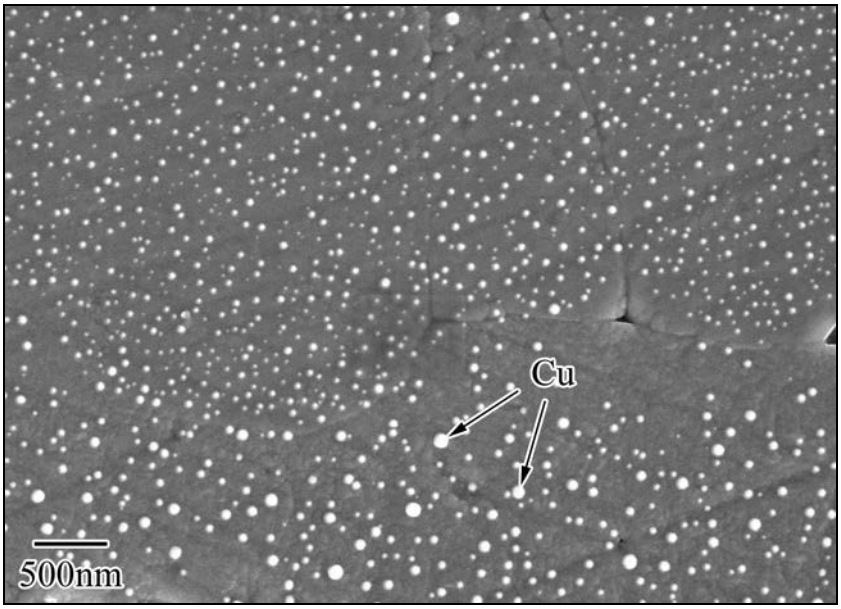

Figure 14. A HRSEM micrograph of the doped Cu sample after thermal etching, before chemical etching of the Cu.

TEM and STEM analysis were used in order to investigate the combined morphology of the alumina matrix grains together with the Cu particles (Figure 15). It was found that the Cu particles differ not only in size between the two composites, but also in shape and morphology.

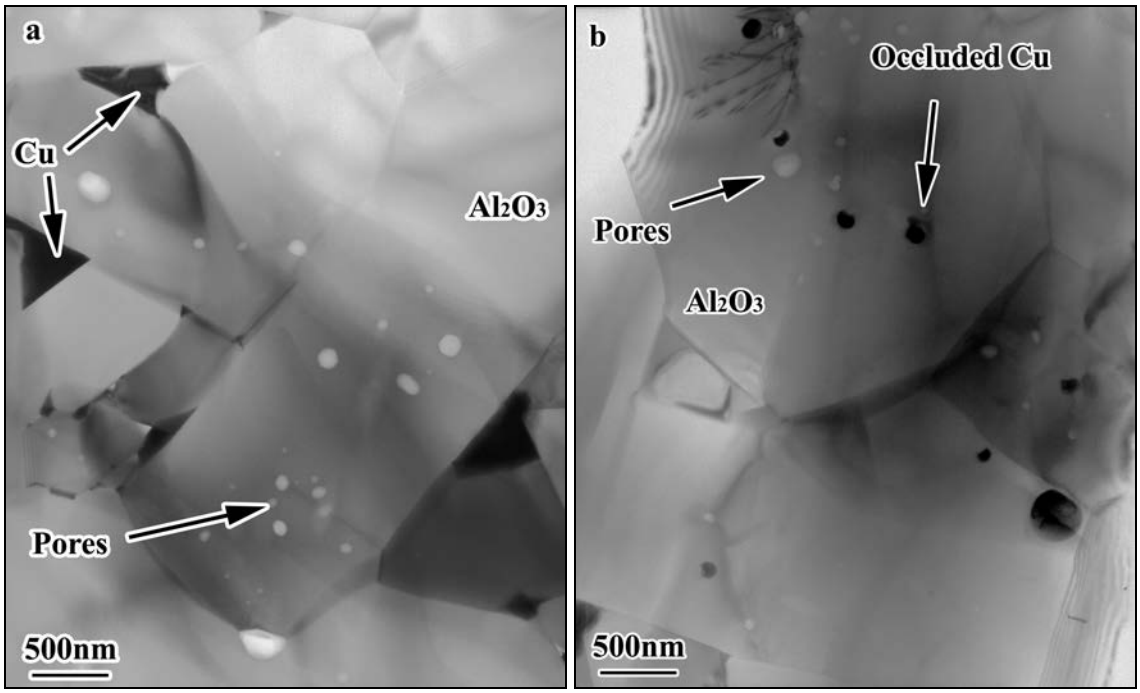

Figure 15. Bright field TEM micrographs showing the general morphology of the Cu-alumina composites a) undoped sample, b) the doped sample.

The copper in the doped sample was found *occluded* within alumina grains, and at alumina grain boundaries (seen in higher magnification in Figure 16a,b). The occluded particles were strongly faceted, and in most cases, a void was observed adjacent to the particle, as seen in Figure 16b. The presence of the void is due to the fact that the particles were occluded in the liquid state, and solidify within the alumina grains, leaving solidification voids. The void space was qualitatively evaluated by approximating its shape to an ellipsoid and the particle to a sphere. The volume ratio of the void was estimated to be around 10-15%, which is approximately the value expected from calculation of the volume change of a *liquid* Cu particle cooled from a temperature of 1550°C to room temperature 14.9% (the expected volume change in the alumina is around 3.5%) [84,85]. For all the occluded particles investigated, low-index alumina planes defined the facet planes. A similar morphology was found for occluded pores or glass pockets. Both the occluded particles and the particles located at triple junctions were found to be equi-axed, while the occluded particles have an aspect ratio closer to 1. Figure 17a presents the aspect ratio measured for the two Cu morphologies in the doped sample. The occluded particles have an average size of 250±20 nm. The particles at the grain boundary had an average size of 1.4±0.3 μm and a wider variation in size. The size distribution of both Cu particles is presented in Figure 17b. The measurement

of the Cu particles was performed using TEM in order to differentiate between the Cu particles found at the alumina grain boundaries from the occluded particles.

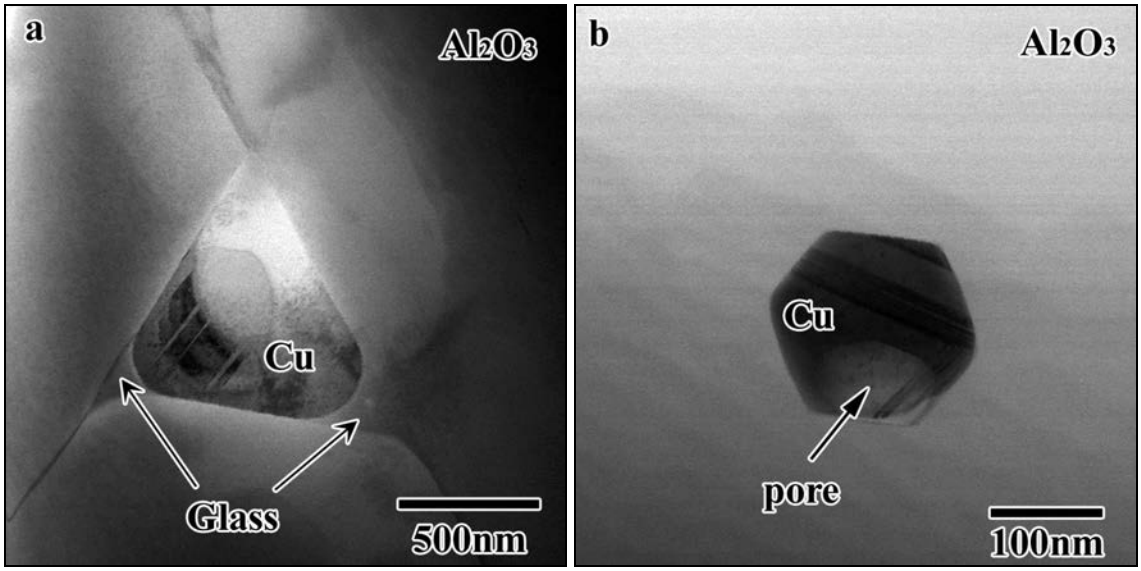

Figure 16. Bright field STEM micrographs showing the morphology of Cu particles in the doped sample, a) Cu particle at a triple junction, b) an occluded Cu particle.

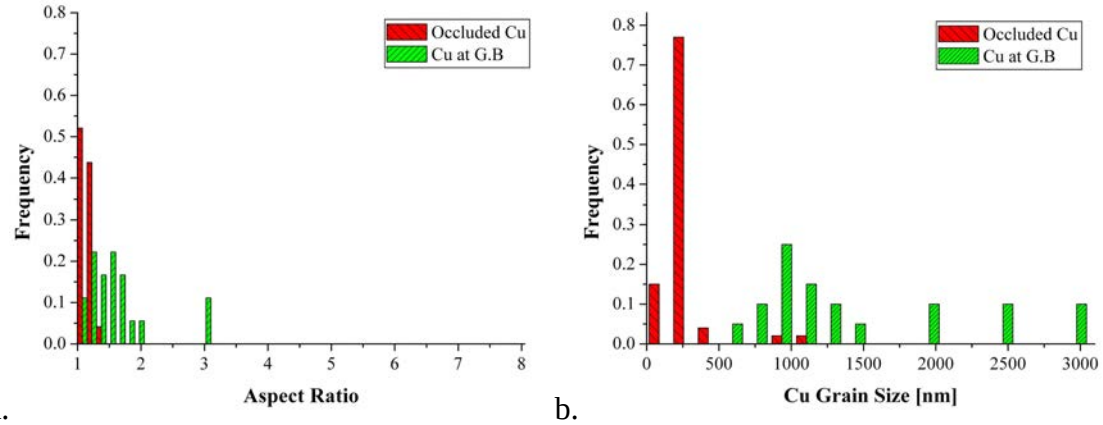

Figure 17. a) Aspect ratio between the long and short axes of the Cu grains in the doped sample. b) Cu particle size distribution in the doped sample. The two particle morphologies are presented in different colors to emphasis the bimodal distribution.

The Cu particles found at triple junctions in the doped sample had non-faceted interfaces with the glass pockets (Figure 16a). EDS measurements were taken from the center of the glass pockets located at the alumina triple junctions and the mean composition from 15 measurements is given in Table 3. The measured composition was found to be rich in Si. These measurements were performed in conventional TEM mode using a converged beam. Figure 18 presents an example of a glass pocket measured by

EDS before and after the measurement. The area measured can be seen as a dark spot resulting from contamination due to the intense focused beam and relatively low vacuum conditions in the microscope column. The diffraction pattern indicates the phase is amorphous. The size of the glass pockets measured ranged between 100nm to 1 μm, with an average size of 500nm. In contrast to the Cu-glass interfaces, the glass–alumina interfaces are strongly faceted.

Table 3. Glass pocket concentration at triple junctions as measured by EDS in TEM from the Cu-alumina glass doped sample. The results are an average from 15 measurements.

Sample	Al [at.%]	Ca [at.%]	Si [at.%]	Cu [at.%]
Cu-Al_2O_3	27.5 ± 4.8	13.4 ± 4.1	56.9 ± 8.8	2.2 ± 0.4

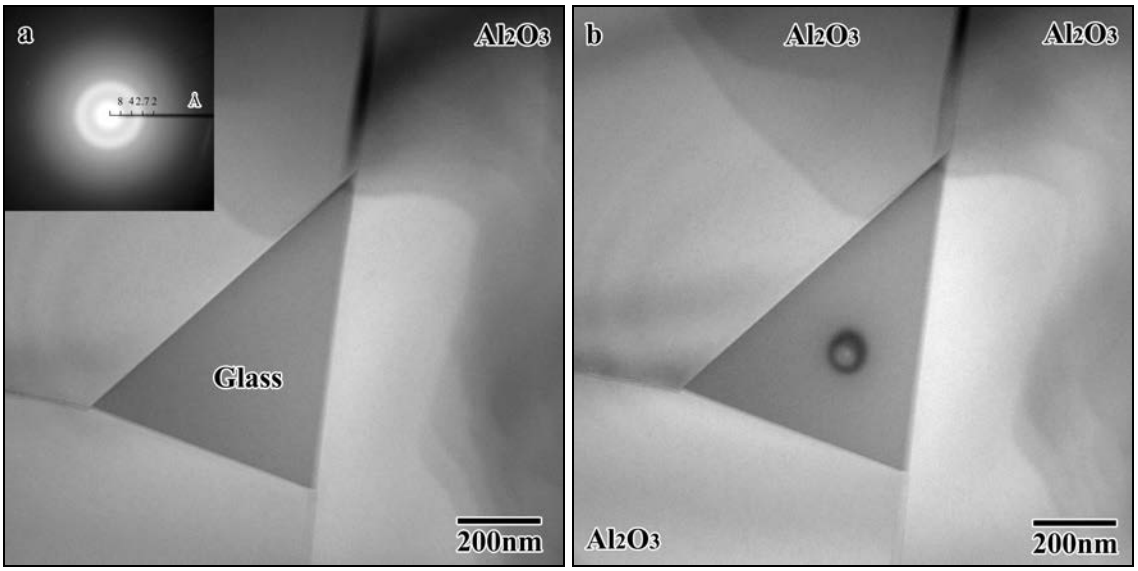

Figure 18. Bright field STEM micrographs of a glass pocket before and after EDS measurement showing the measured area was limited to the glass phase together with a diffraction pattern indicating it is an amorphous phase.

The CaO and SiO_2 content in the sample was calculated to be ~3.2 and 2.0 at.% respectively, based on the amounts of dopants added (relative to Al_2O_3 matrix). The calculation was performed assuming all the Si introduced using the sol gel process ended up *evenly* in the sample, and the Ca nitrate solution penetrated all the pores in the alumina green body at the same concentration as the original solution and dried evenly inside the pores. EDS and WDS measurements were performed on different samples at low magnifications (x1000) to evaluate the over-all impurities concentration. WDS was used for the undoped samples, since the impurities concentration in them was below the detection limit of the EDS measuring system. The measured values are given in Table 4.

It should be noted that performing the measurement over an area containing different phases may lead to relatively high errors since the methods assume a uniform concentration of the elements within the measured area for the ZAF (Z - atomic number, A -absorption, and F - fluorescence) corrections. The measurements indicated the SiO_2 distribution in the doped samples was more uniform than the CaO. The *undoped* samples turned out to have been contaminated during the processing. (This effect will be examined in detail in the next section.)

Table 4. CaO and SiO_2 atomic concentration in the different samples as measured by EDS and WDS.

Sample	SiO_2 at. %	CaO at. %	Cu at. %	Method
Undoped Alumina	0.05 ± 0.01	0.01 ± 0.003	-	WDS
Doped Alumina	1.0 ± 0.2	3.4 ± 0.9	-	EDS
Doped Alumina	0.45 ± 0.06	1.9 ± 0.2	-	WDS
Undoped Cu-alumina	0.04 ± 0.007	0.006 ± 0.003	-	WDS
Undoped Cu-alumina	-	-	3.7 ± 0.5	EDS
Doped Cu-alumina	1.1 ± 0.2	1.24 ± 0.7	4.8 ± 1.6	EDS
Detection limit	0.004	0.002	-	WDS

In the undoped sample, the copper particles were found only at triple junctions and along the alumina grain boundaries (see Figure 15a and Figure 19). These particles were smaller than the particles observed in the doped sample and in many cases were elongated (Figure 19b). Many of the triple junctions contained nanometer sized copper particles, an example of which can be seen in Figure 19a.

Occluded pores were found in both samples, although a significantly greater number of occluded pores were found in the doped sample (Figure 15).

The aspect ratio and the size distribution of the Cu particles in the undoped sample are presented in Figure 20a, and Figure 20b respectively. The average values for the short and long axes are 240 and 560nm, correspondingly. In contrast to the Cu particles in the doped sample, the Cu in the undoped samples formed sharp angles at the triple junctions and tended to penetrate deep into the alumina grain boundaries. In some cases the Cu particles actually formed elongated grains at the alumina grain boundaries (see Figure 19b).

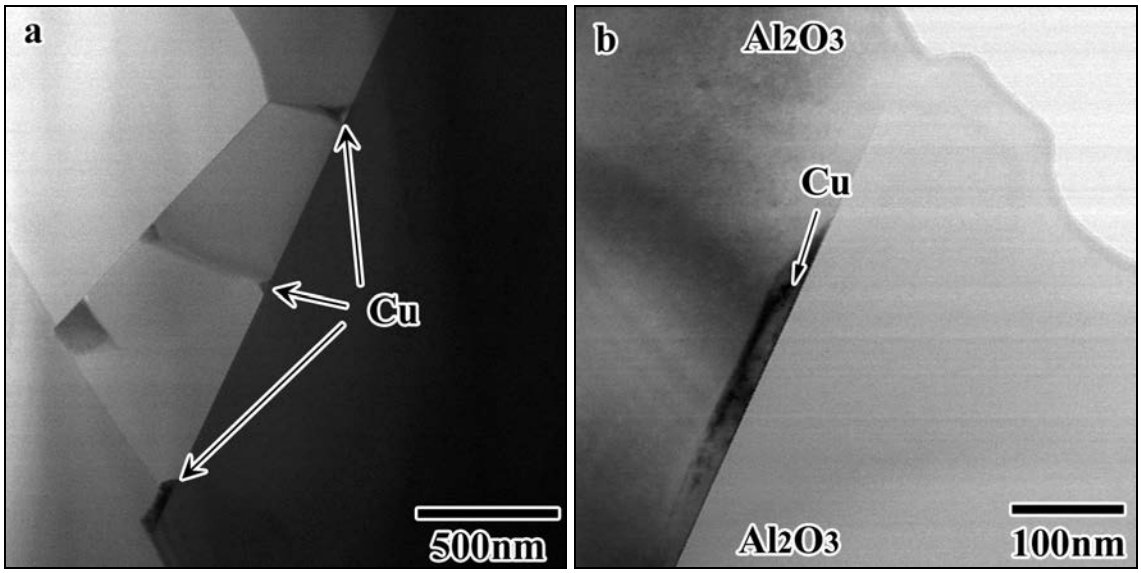

Figure 19. Bright field STEM micrographs showing the morphology of Cu particles in the undoped sample. a) Cu particles at alumina triple junctions, b) an elongated Cu particle at an alumina grain boundary.

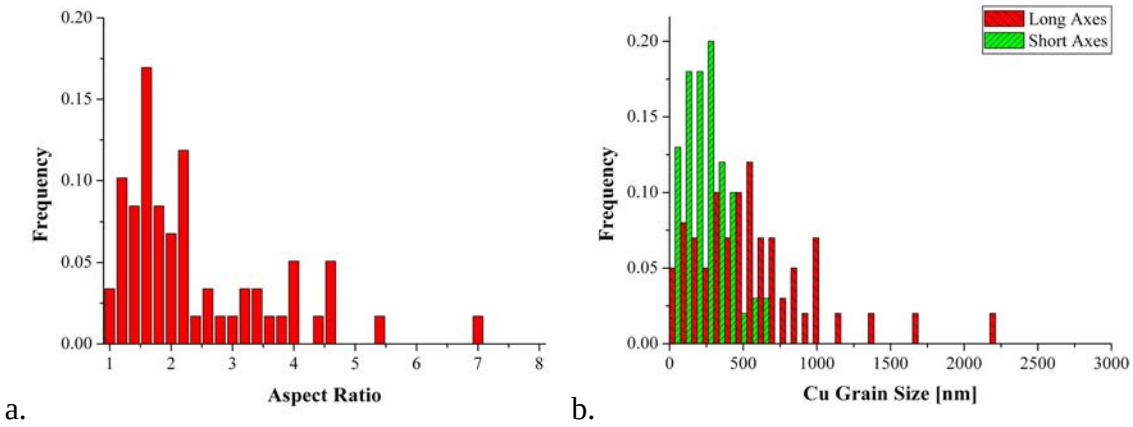

Figure 20. a) Aspect ratio between the long and short axes of the Cu grains in the undoped sample. b) Cu particle size distribution in the undoped sample. Both the long and short axes are presented.

Analysis of the interface structure was performed by HRTEM and STEM. To precisely measure the intergranular film thickness, the film's interfaces have to be parallel to the optical axis of the microscope (edge-on condition) as shown in Figure 21b, and the film-grain interface well defined by the lattice structure (a lattice image should be visible from the two grains). These prerequisites limit the imaging conditions considerably (especially at alumina grain boundaries). Alumina is anisotropic and its grain boundaries in many cases tend to be highly faceted and edge on condition are not possible, or the lattice image can not be obtained from both grains at the same time (as shown in Figure 21a and Figure 22).

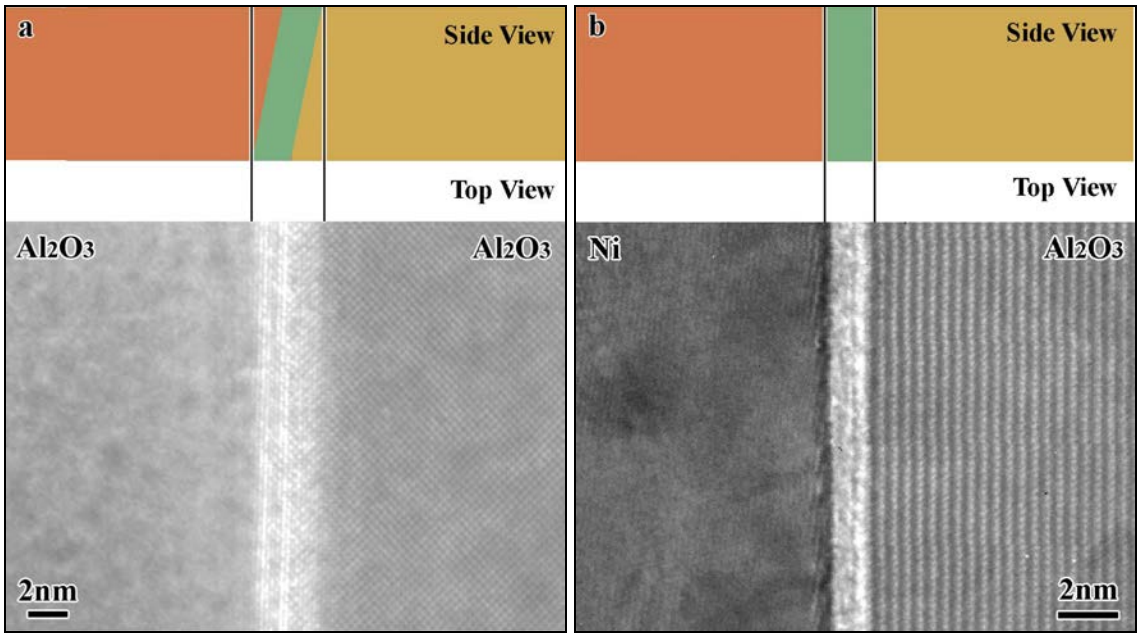

Figure 21. HRTEM micrographs of a) an inclined alumina grain boundary, and b) an "edge-on" Ni-alumina interface.

The tendency of the alumina interfaces to form faceted planes is actually beneficial in the case of *metal-alumina* interfaces, since in these cases the *edge-on* conditions will be predominately defined by the alumina terminating plane. An example of these imagining conditions can be seen in Figure 21b, where the lattice image from the alumina grain is clearly visible, while on the metal side only one set of fringes is observed (this is enough, in most cases, to measure the intergranular film thickness).

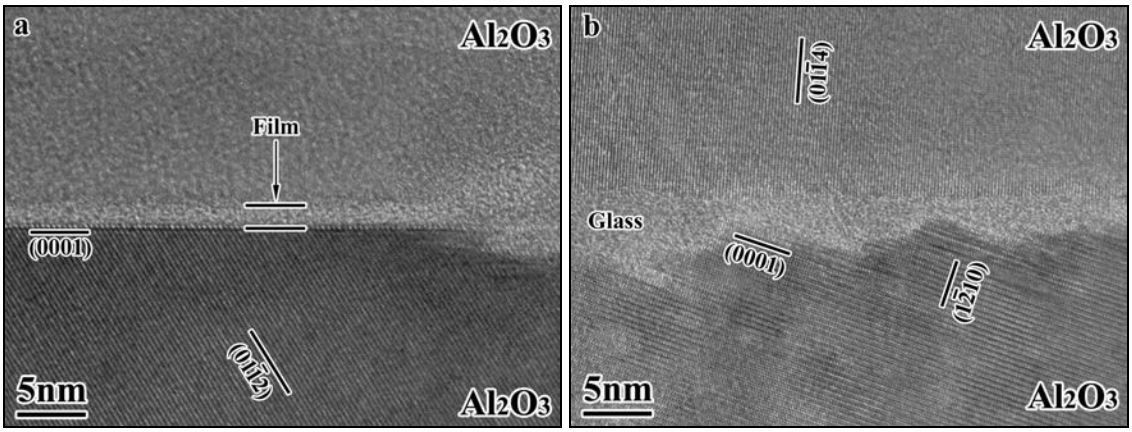

Figure 22. HRTEM micrographs of intergranular films at a) a flat, and b) faceted alumina grain boundaries in the doped Cu-alumina composite.

Figure 22 presents two examples of intergranular films at alumina *grain boundaries* in the Cu-Al_2O_3 doped sample. EDS line scans performed across such *alumina grain boundaries* indicated the presence of Ca and Si in the grain boundary films (Figure 23). Intergranular films were observed at all the *Cu-Al_2O_3* interfaces analyzed. Examples of these films between alumina grains and Cu particles found at the boundaries can be seen in Figure 24. EDS analysis conducted on an area including the Cu-alumina interface films confirmed they consisted of Ca and Si (Figure 25). An EDS line-scan performed across a glass pocket at a Cu-alumina triple junction (in STEM mode), indicates there is Al segregation at the Cu-glass interface, and Ca segregation at the alumina-glass interface (seen in Figure 26).

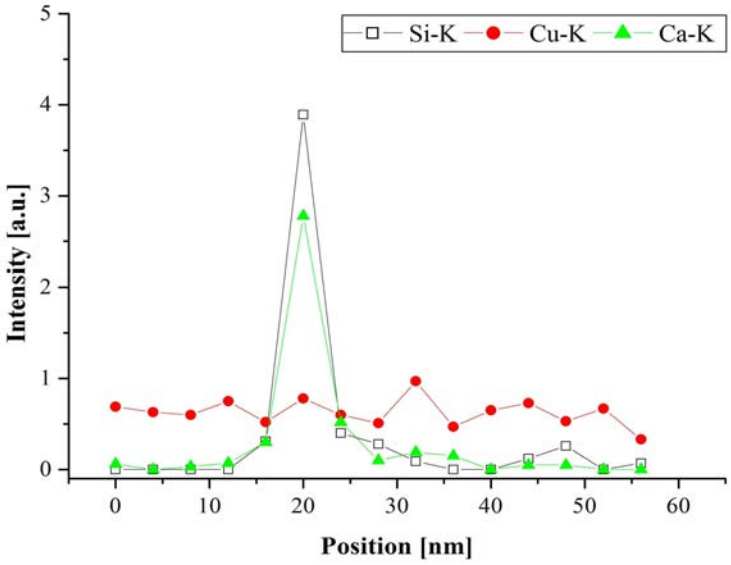

Figure 23. EDS line-scan acquired across an alumina grain boundary, showing the presence of Si and Ca at the grain boundary.

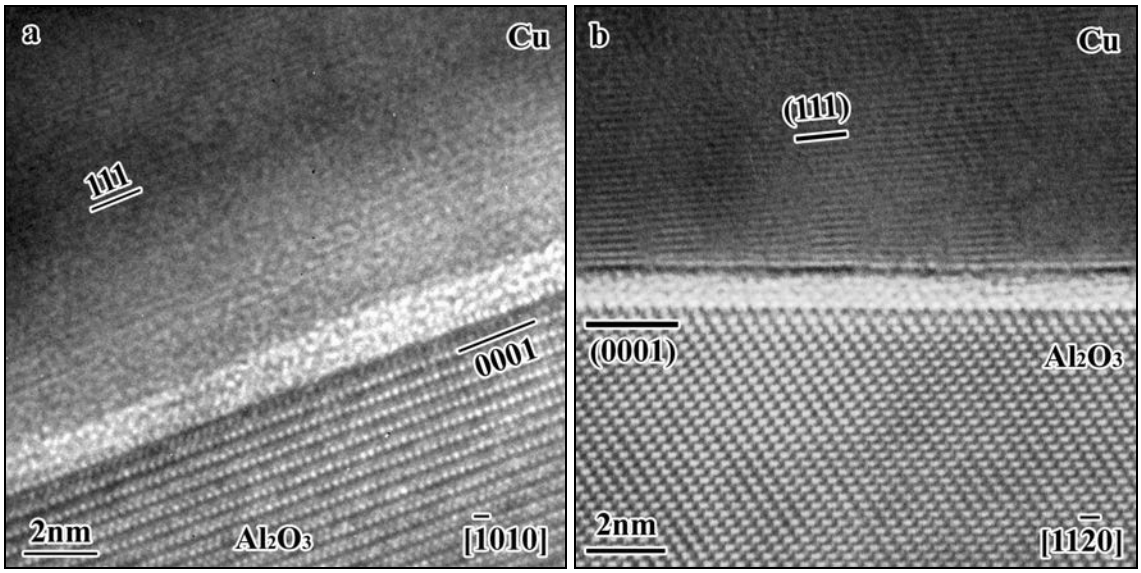

Figure 24. HRTEM micrographs of intergranular films at Cu-alumina interfaces (a) [$\bar{1}010$] zone axis and (b) [$1\bar{2}10$] zone axis. In both cases the alumina terminating plane is (0001).

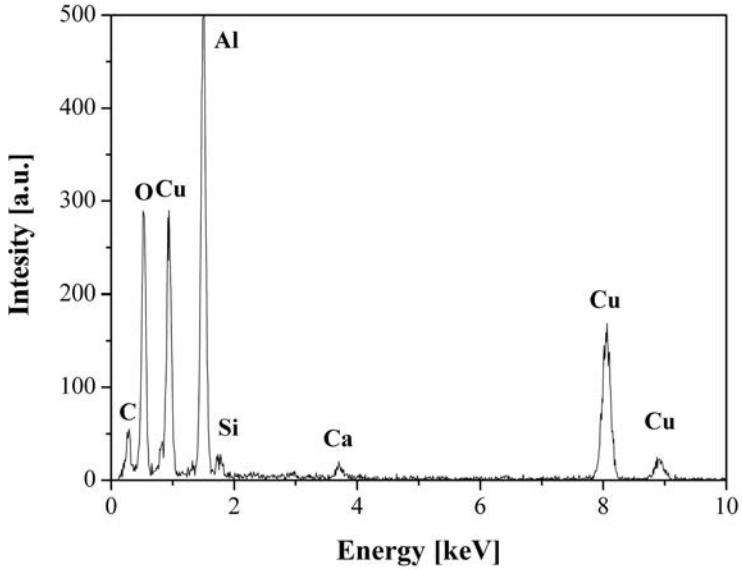

Figure 25. EDS analysis performed on an area including Cu-Al_2O_3 interface in the Cu-alumina doped composite.

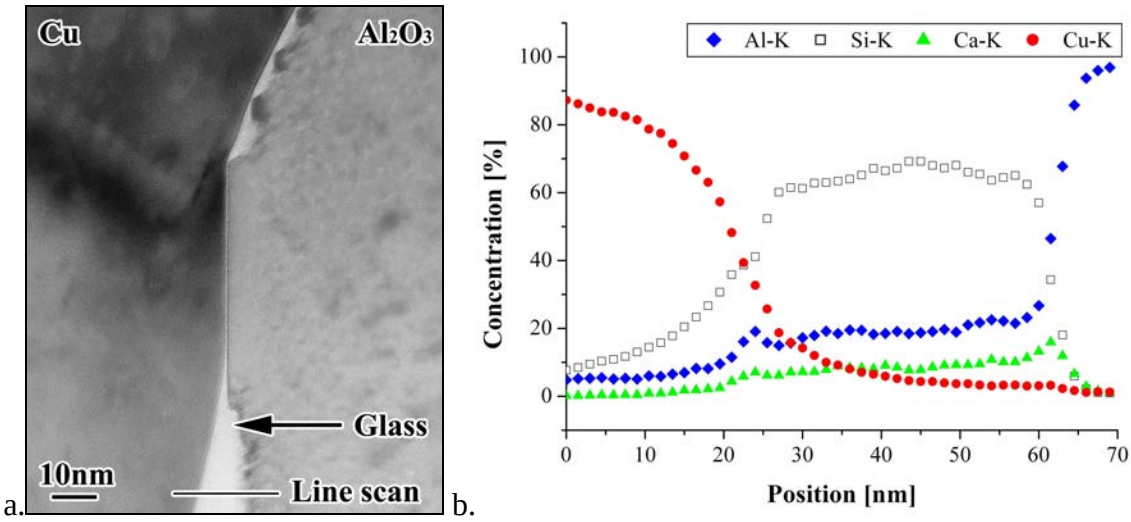

Figure 26. a) Bright field TEM micrograph of a Cu-alumina interface together with a glass pocket, and b) an EDS line-scan acquired across the glass between the Cu particle, and an alumina grain. The region from which the line-scan was acquired is indicated in (a).

The presence of the films *persisted* after occlusion of the Cu-particles by the alumina grains, and extended along all the facets, as shown in Figure 27, where the alumina grain is in a $[11\bar{2}0]$ zone axis and films are found at (0001) and $(1\bar{1}02)$ alumina terminating planes. Another example of a film found between an occluded Cu particle and the alumina matrix is given in Figure 28, this time with a $(1\bar{2}1\bar{3})$ terminating alumina plane (the alumina is in a $[3\bar{1}\bar{2}1]$ zone axis).

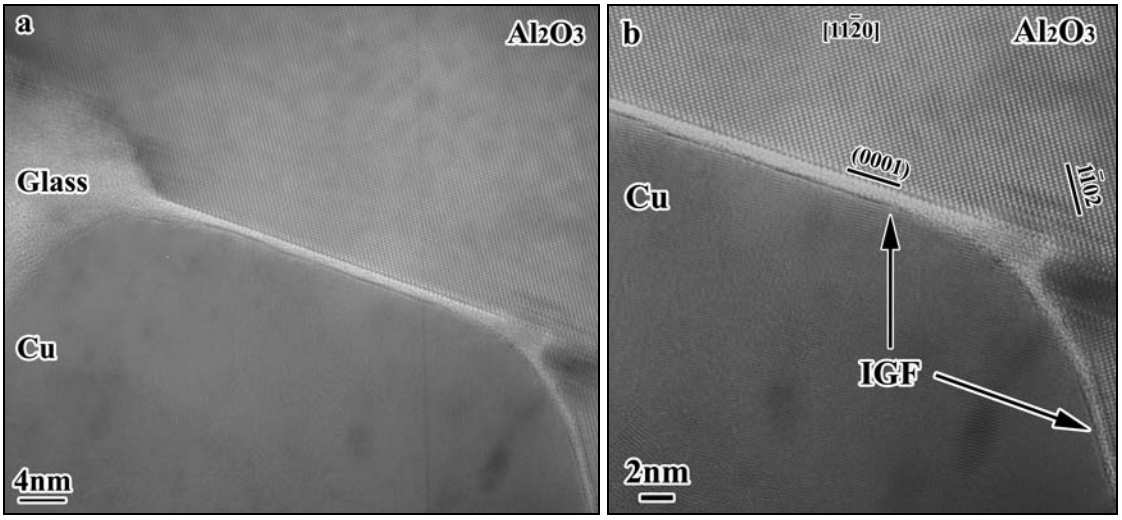

Figure 27. a) HRTEM micrograph of an intergranular film at an occluded Cu particle interface with the surrounding alumina grain in the doped Cu-alumina composite, b) a higher magnification of one of the corners of the Cu particle.

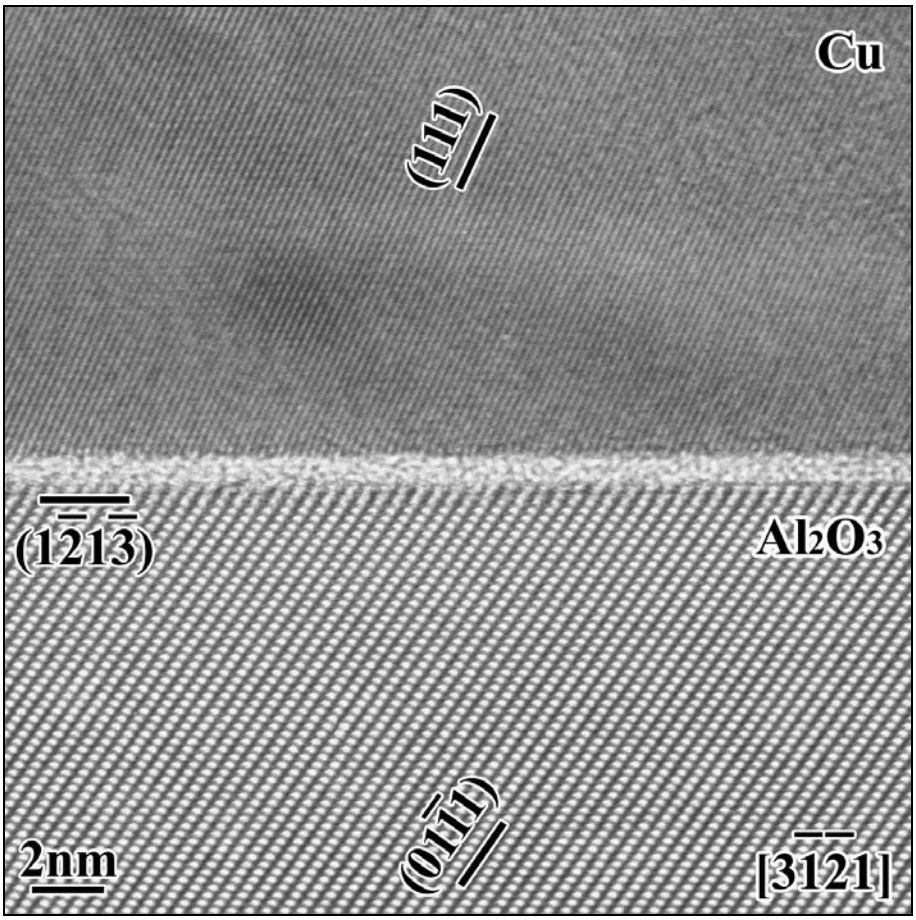

Figure 28. HRTEM micrograph of an intergranular film at an occluded Cu particle interface with the alumina grain in the doped Cu-alumina composite. The alumina grain is in $[3\bar{1}\bar{2}1]$ zone axis and $(1\bar{2}1\bar{3})$ terminating plane.

HRTEM analysis of the Cu-Al_2O_3 interfaces in the *undoped* sample did not reveal any intergranular films, but a strong contrast is seen at the interfaces (see Figure 29). This is probably due to contamination, that was detected both from EDS measurements conducted at the interfaces, as well as from WDS analysis of the bulk sample (see Table 4). No films were observed at the alumina grain boundaries in the undoped samples (Figure 30). It is important to emphasize here that although it is evident that the "clean" sample was not free from impurities, intergranular films did not develop, indicating a threshold amount of impurities is needed to form the films, which was not reached in this case.

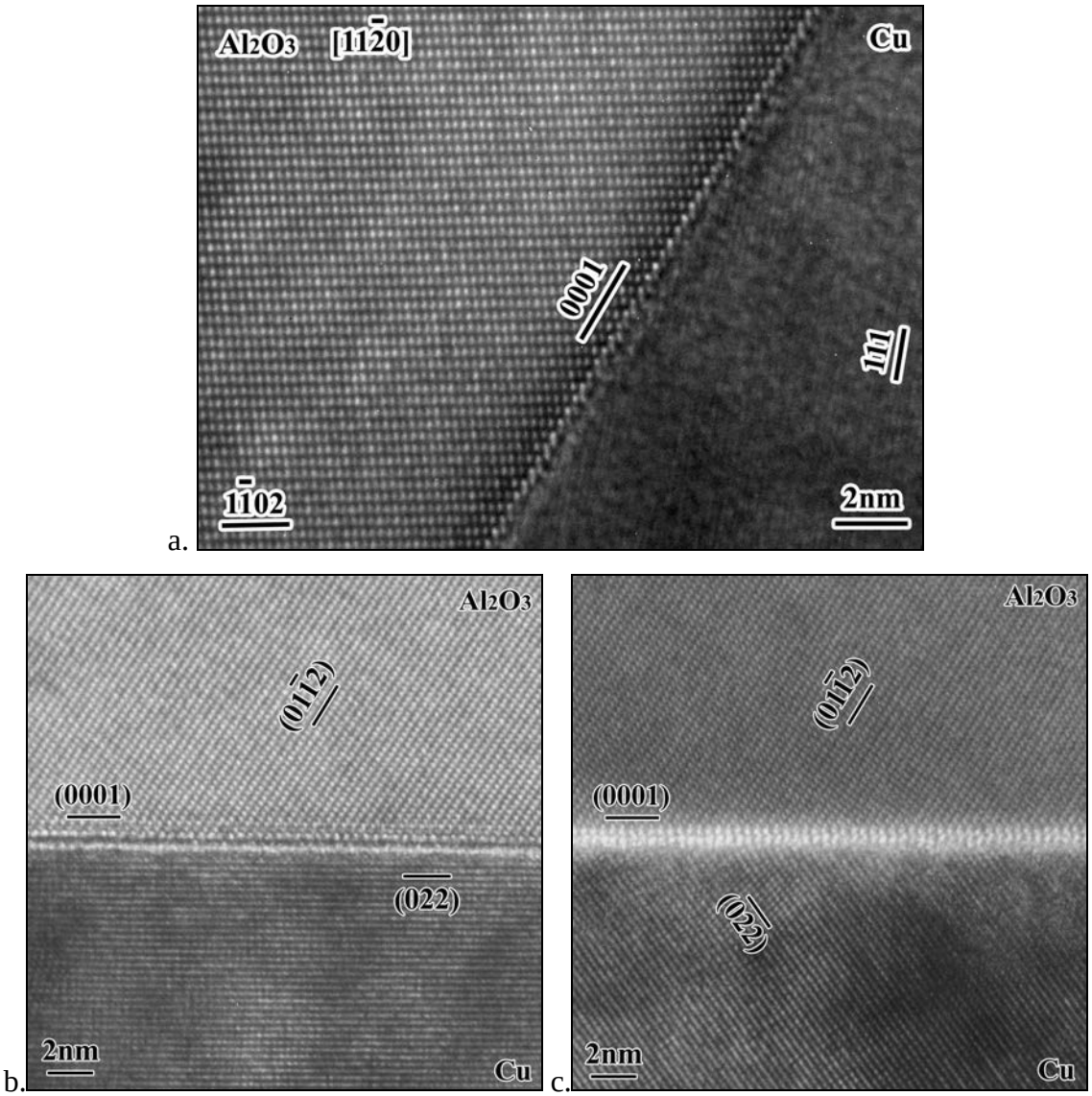

Figure 29. HRTEM micrographs of three Cu-alumina interfaces in the undoped Cu-alumina composite. In all three micrographs the alumina grains are in the $[1\bar{2}10]$ zone axis and the (0001) alumina plane is parallel to the interface.

Measurement of the intergranular film thickness was performed on all the interfaces recorded in edge-on conditions. Each interface was measured at 10 different locations along the film. The measurements were performed using Digital Micrograph, and the length scales were calibrated using the lattice spacing of alumina. The results from the measurements are presented in Table 5.

The Si and Ca excess were determined by EDS analysis. The data was acquired for 100s while the electron beam was scanning over a rectangular area of 4x3nm^2. One measurement was performed in the area containing the interface, and two in the nearby bulk materials. The impurity signal I_{imp} was obtained by:

$$(17) \qquad I_{imp} = I - \alpha I_1 - \beta I_2$$

where I is the spectrum taken at the region containing the interface, and I_1 and I_2 are the intensities in the spectra taken from the nearby bulk materials. The scaling factors, α and β, are determined relative to the scanned area from each of the nearby grains where no bulk signal is expected (due to very low solubility in the bulk). To obtain the relative atomic ratio the intensities were multiplied by the Cliff-Lorimer factor in at.%. The values of the Ca to Si excess ratios (atomic) measured at alumina grain boundaries, and Cu-alumina interfaces, is presented in Table 6. In the measurements performed at the grain boundaries some Cu excess was observed but was not quantified.

Ideally, the thickness measurement and chemical analysis should be conducted on the same interfaces, to enable correlation of the two parameters. This was not always technically feasible.

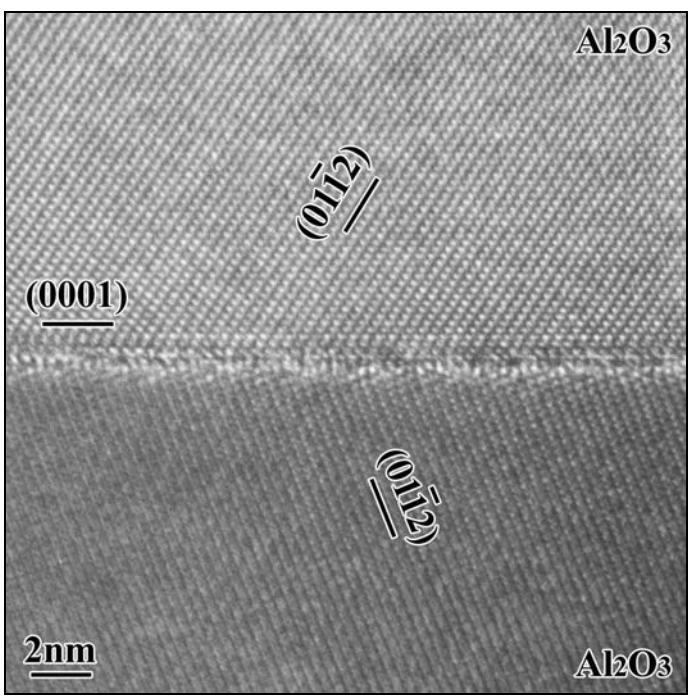

Figure 30. HRTEM micrographs of an alumina grain boundary in the undoped Cu-alumina composite.

Table 5 . Intergranular film thickness at Cu-alumina interfaces and alumina grain (GB) boundaries in the Cu-alumina doped sample.

Composite	Interface	Terminating Plane	Thickness [nm]	Number of Measurements
Cu-Al_2O_3 (Doped)	Al_2O_3-Al_2O_3	-	1.45 ± 0.15	(1)
	Cu-Al_2O_3	(0001)	1.0 ± 0.1	(5)
	Cu-Al_2O_3	$(1\bar{2}1\bar{3})$	0.8 ± 0.1	(1)
	Cu-Al_2O_3	$(10\bar{1}2)$	0.8 ± 0.1	(1)

Table 6. Ca to Si ratio measured for the alumina grain boundaries and Cu alumina interfaces (VG-STEM).

Composite	Interface	Ca:Si Excess Ratio	Number of Measurements
Cu-Al_2O_3 (Doped)	Al_2O_3-Al_2O_3	1 : 1.9±0.5	(4)
	Cu-Al_2O_3	1 : 2.1±0.3	(2)

3.1.2. Ni-Al_2O_3 Composites

Phase Analysis and General Morphology

The Ni-Al_2O_3 composites were analyzed in a similar manner to the Cu-Al_2O_3 composites. XRD phase analysis of the doped and undoped samples is presented in Figure 31. No phases other than Ni and alumina were observed for both composites. The absence of oxides or aluminates is in agreement with previous studies reporting the formation of such phases only above 2.9×10^{-5} Torr (3.9×10^{-3} Pa) [86,87]. No indication of CA6 formation was found in XRD or TEM analysis of the doped sample.

Figure 32 presents BSE SEM micrographs of the doped and undoped samples. The Ni particles were dispersed uniformly in the alumina matrix in both samples. A coarser microstructure was found in the doped sample, relative to the undoped sample. This kind of behavioriour was also observed in the Cu-alumina composites, although in the Ni composites the microstructure was finer. The Ni in the undoped sample is not clearly seen since the average particle size (~150nm) is below the resolution that can be resolved in the magnification of the image. The relative porosity and Ni volume is given in Table 7 based on image analysis of BSE SEM images taken at a magnification of x1000 at 20kV.

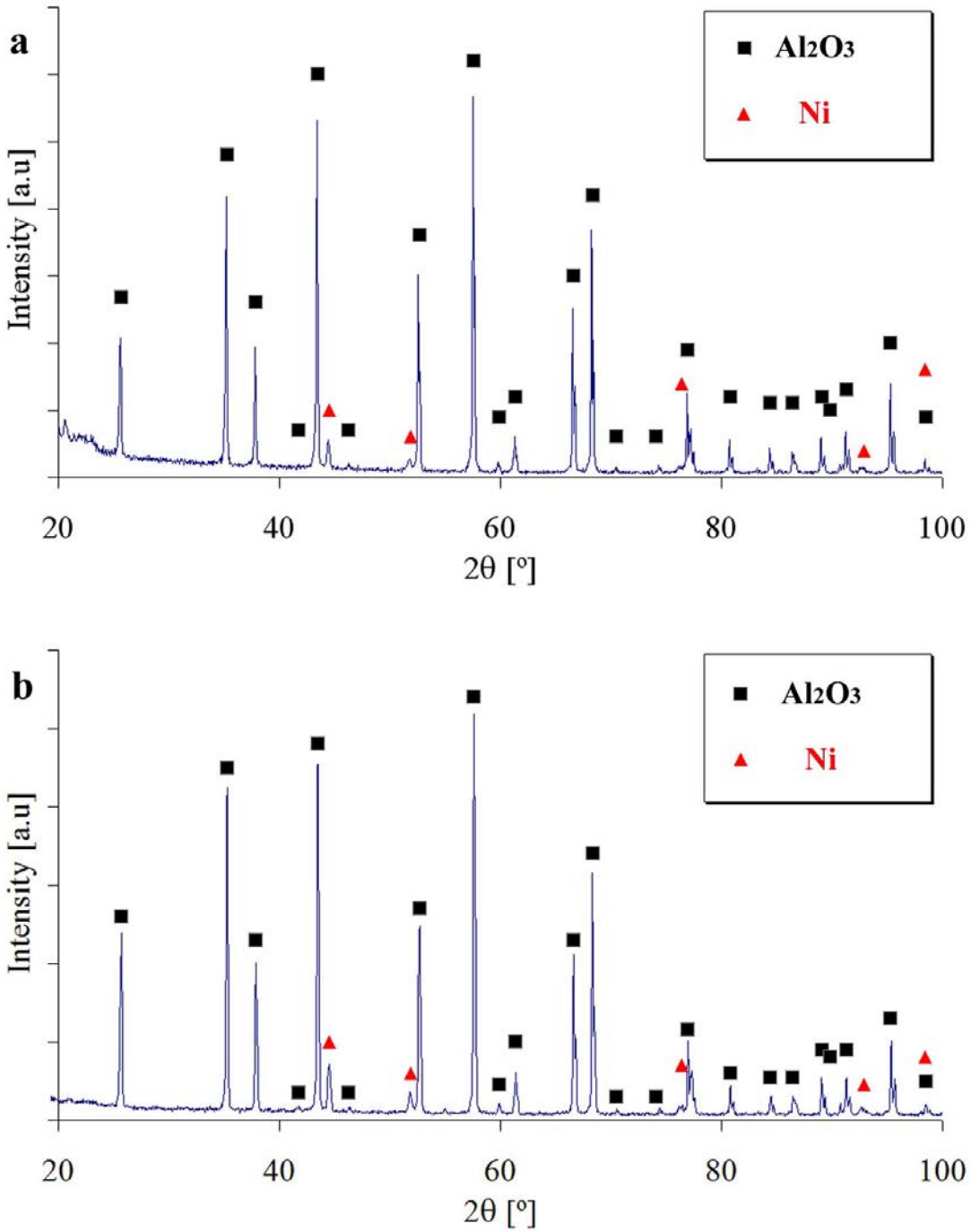

Figure 31. XRD patterns obtained from the a) Ni-alumina undoped sample, b) Ni-alumina glass doped sample.

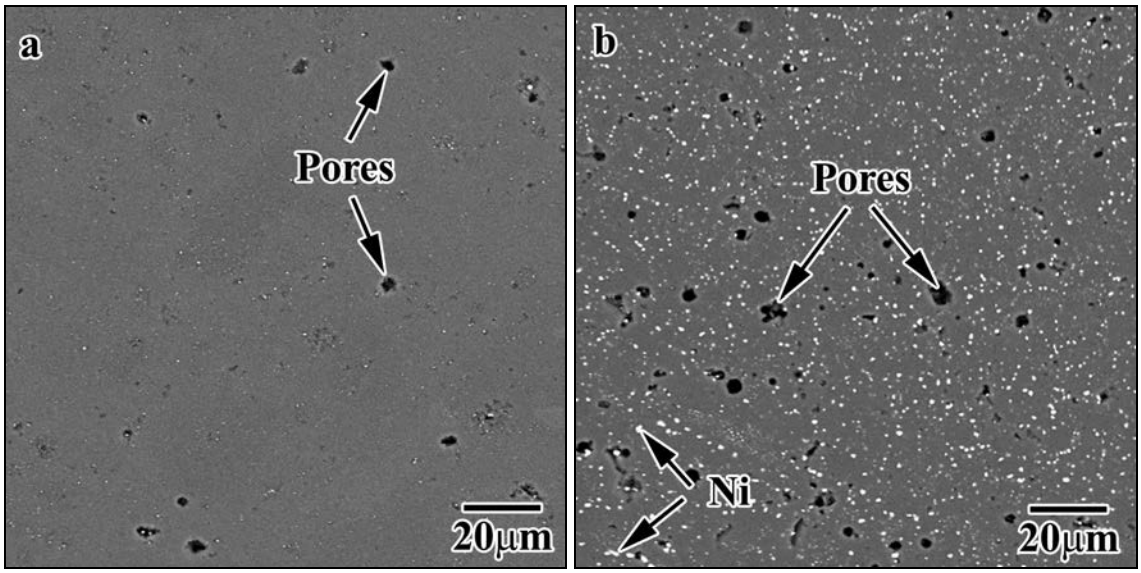

Figure 32. SEM micrographs taken in BSE mode showing the dispersion of Ni particles in the alumina matrix. a) undoped sample (the Ni particles size (~150nm) are below the resolution at this magnification), b) doped sample.

Table 7. Relative porosity and metal volume measured from BSE SEM images of the Ni-alumina composites.

Sample	Porosity Vol. %	Ni Vol. %	Ni at. %
Undoped Ni-alumina	0.7 ± 0.3	-	-
Doped Ni-alumina	3.4 ± 1.3	3.9 ± 0.5	11.3 ± 1.5

TEM investigation of the doped samples showed the formation of glass pockets at the triple junctions and occlusion of Ni particles (Figure 33). EDS measurements of the glass pockets indicated they are Si rich, but contained higher levels of Ca than found in the Cu-alumina doped composite (Table 8). The size distribution of the Ni particles in the Ni-alumina doped sample is given in Figure 34 (performed using TEM micrographs). Once again, a clear bimodal distribution of the particle size is evident. The occluded Ni had an average size of 260 ± 90nm, and the particles found at the alumina triple junctions and grain boundaries had an average size of 850 ± 350nm.

Table 8. Glass pocket concentration at triple junctions as measured by EDS in TEM from the Ni-alumina doped sample. The results are an average from 9 measurements.

	Al [at.%]	Ca [at.%]	Si [at.%]	Ni [at.%]
Ni-Al_2O_3	31.8 ± 6.7	26.6 ± 7.8	40.1 ± 11.6	1.6 ± 1.3

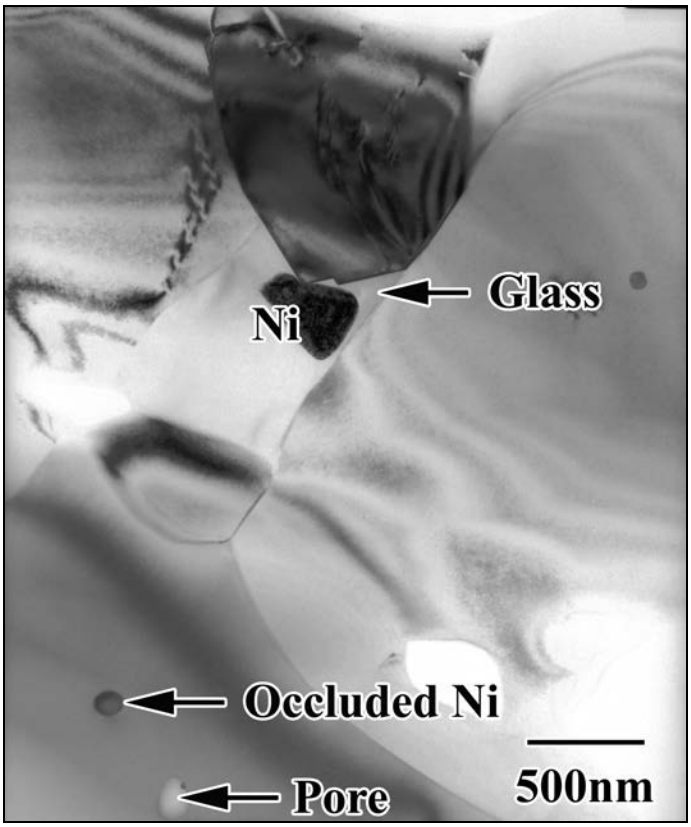

Figure 33. Bright field TEM micrograph showing the general morphology of the Ni-alumina doped composite.

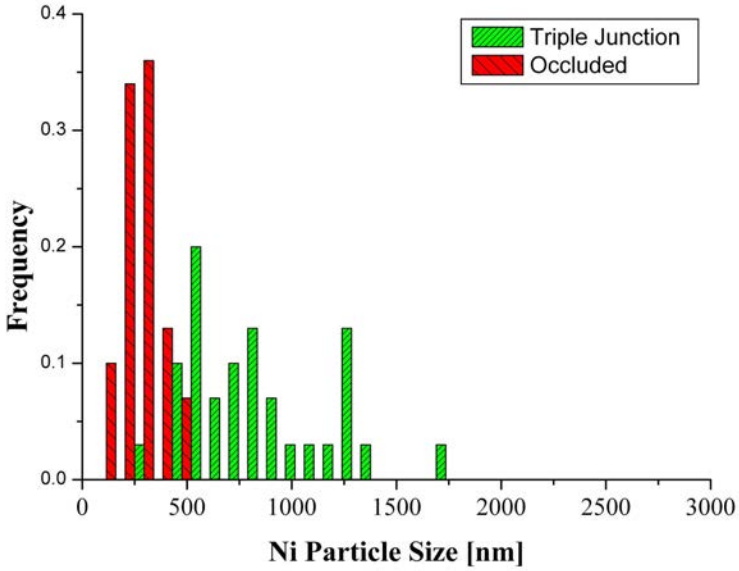

Figure 34. Ni particle size distribution in the doped sample. The two particle morphologies are presented in different colors to emphasize the bimodal distribution. 100 particles were measured.

As in the Cu-Al_2O_3 composites, the Ca and Si content in the samples was measured by EDS and WDS and is given in Table 9.

Table 9. CaO and SiO_2 atomic concentration in the different Ni-alumina composites as measured by EDS and WDS.

Sample	SiO_2 at. %	CaO at. %	Ni at. %	Method
Undoped Ni-alumina	0.06 ± 0.02	0.04 ± 0.01	-	WDS
Undoped Ni-alumina	-	-	3.6 ± 0.2	EDS
Doped Ni-alumina	0.9 ± 0.2	0.6 ± 0.1	4.8 ± 0.35	EDS
Detection limit	0.004	0.002	-	WDS

Interface Structure and Chemistry

Intergranular films were also found at Ni-alumina interfaces in the doped Ni-alumina composite. Figure 35 and Figure 36 show examples of intergranular films found at different alumina terminating planes. In Figure 35a the Ni particle was very close to the [101] zone axis, with the (111) Ni plane parallel to the interface with the film. The intergranular film at the Ni-alumina interface appears to be partially ordered. However, the contrast transfer function of the microscope can induce periodic variations in contrast regardless of the degree of periodicity in the sample. This effect remains to be investigated.

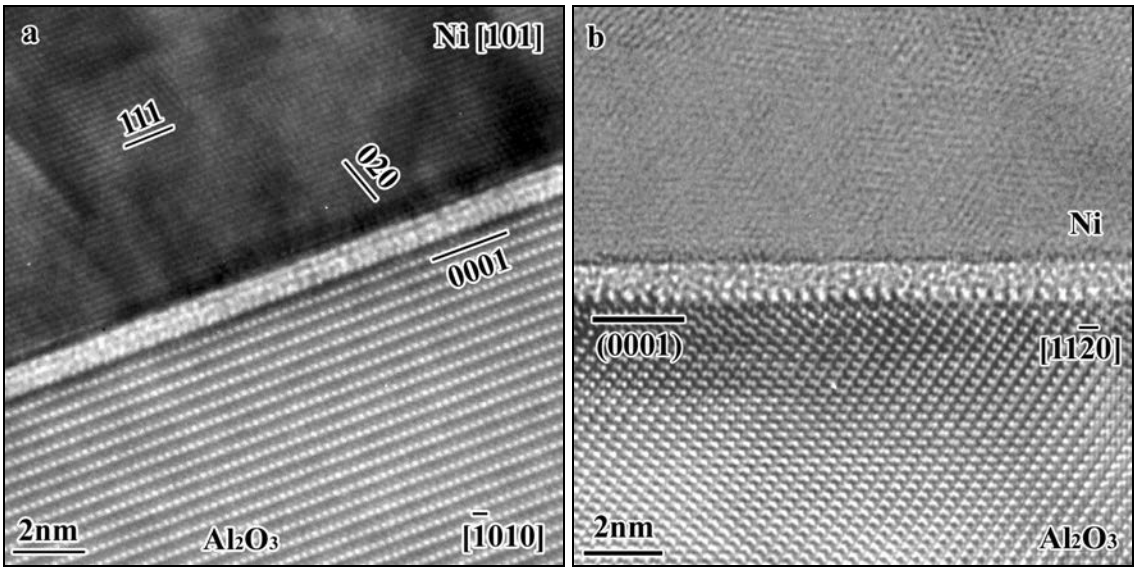

Figure 35. HRTEM micrographs of intergranular films at Ni-alumina interfaces in the doped Ni-alumina composite (a) $[\bar{1}010]$ zone axis and (b) $[11\bar{2}0]$ zone axis. In both cases the alumina terminating plane is (0001).

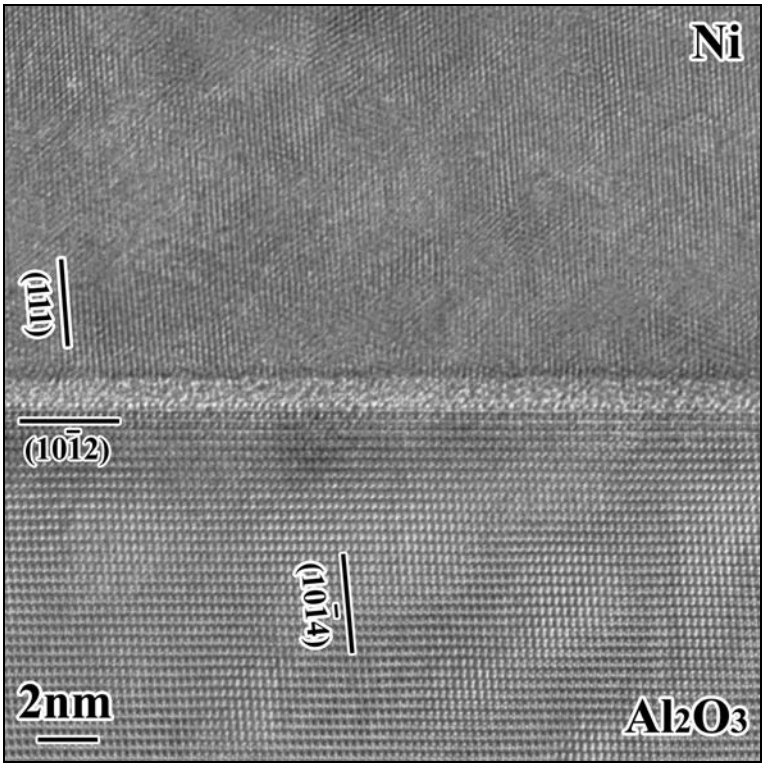

Figure 36. HRTEM micrographs of an intergranular film at a Ni-alumina interface in the doped Ni-alumina composite**,** with a $(10\bar{1}2)$ alumina terminating plane**.**

Intergranular film thickness at Ni-alumina interfaces, and Ca to Si excess measurements of the films in the Ni-alumina doped composite, are presented in Table 10 and Table 11, respectively.

Table 10. Intergranular film thickness at Ni-alumina interfaces and alumina grain (GB) boundaries in the Ni-alumina doped sample.

Composite	Interface	Terminating Plane	Thickness [nm]	Number of Measurements
Ni-Al_2O_3 (Doped)	Al_2O_3-Al_2O_3	-	1.0±0.1	(1)
	Ni-Al_2O_3	(0001)	0.87±0.1	(7)
	Ni-Al_2O_3	$(01\bar{1}2)$	0.96±0.1	(3)

Table 11. Ca to Si ratio measured for the alumina grain boundaries and Ni alumina interfaces. (VG-STEM).

Composite	Interface	Ca:Si Excess Ratio	Number of Measurements
Ni-Al_2O_3 (Doped)	Al_2O_3-Al_2O_3	1 : 1.5±0.2	(2)
	Ni-Al_2O_3	1 : 0.2±0.1	(2)

Figure 37 presents a HRTEM micrograph taken from an alumina Σ3 grain boundary [88]. This grain boundary is low-energy grain boundary and therefore was not infiltrated by the glass [15,40].

One Ni-Al_2O_3 interface was found with only a partial intergranular film (Figure 38). EDS analysis performed on the same interface in an area absent of the film showed the Ca content was below the detection limit. However, this EDS measurement was performed in TEM mode using a relatively large electron beam diameter and it was not possible to detect any Ca and Si excess. On the other hand, under these conditions in other Ni-alumina interfaces possessing an intergranular film the Ca and Si excess was clearly detected.

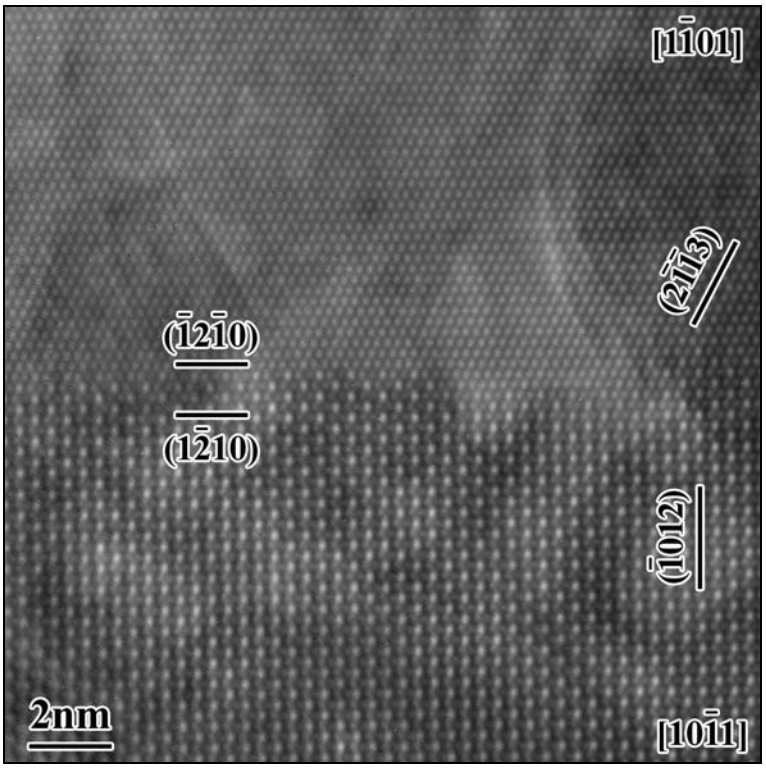

Figure 37. A HRTEM micrograph of a dry grain boundary (with a special orientation) in the Ni-alumina doped sample.

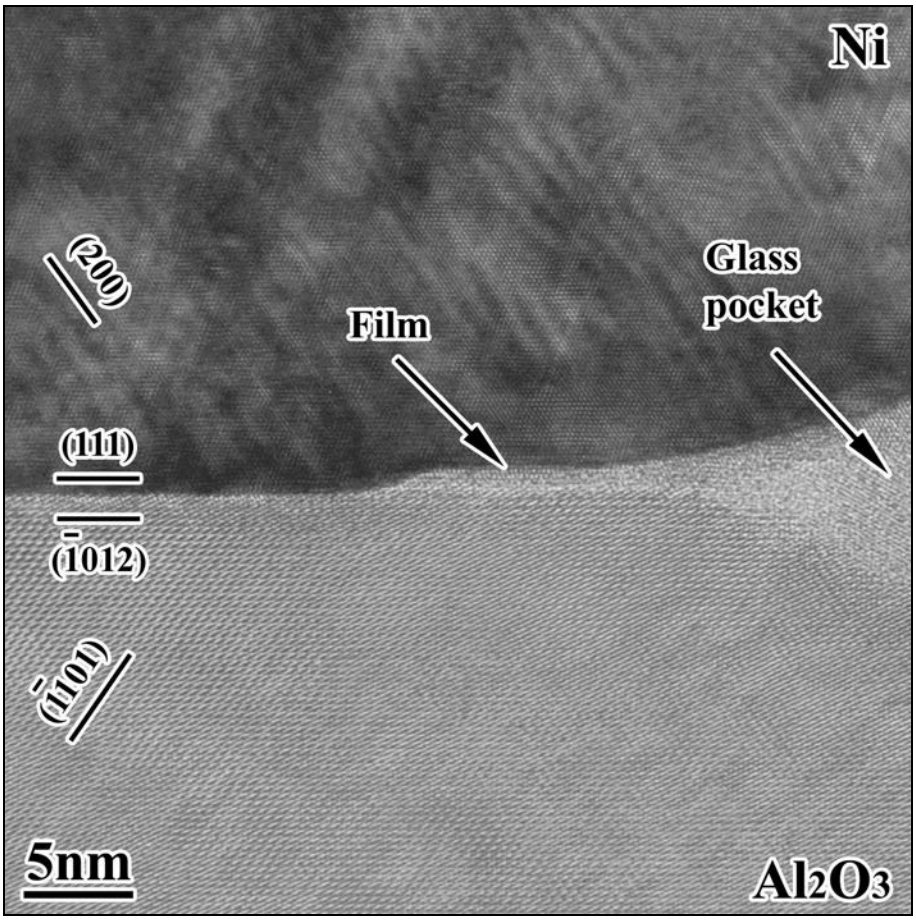

Figure 38. HRTEM micrograph of a partial intergranular film at a Ni-alumina interface. The Ni particle and alumina grain have the following orientation relationship $[01\bar{1}] \parallel [10\bar{1}1]$ and $(111) \parallel (\bar{1}012)$ correspondingly.

3.2. Sessile Drop Wetting Experiments

This section is dedicated to the model wetting experiments. The wetting experiments were performed on a predetermined sapphire plane using two metals (Cu and Ni), with and without the presence of an anorthite glass drop. The aim of these experiments was to determine the relative metal-alumina interface energy, and to determine whether the glass would penetrate the metal-alumina interface.

3.2.1. Wetting of Cu on Al_2O_3

The wetting experiments were performed on (0001) sapphire plane substrates. The contact angles were determined based on the drop shape as measured from CCD images taken *in-situ* during the experiments. Due to the relatively small size of the drops, the influence of gravity may be neglected, and the drop can be approximated to a spherical cap [83]. Figure 39a presents a CCD image of a Cu drop on (0001) sapphire, at a temperature of 1250°C. The contact angle was calculated using the following geometrical relations:

$$R_0 = \frac{H_d^2 + r_d^2}{2H_d} \tag{18}$$

$$\theta = cos^{-1}\left(\frac{R_0 - H_d}{R_0}\right) \tag{19}$$

where R_0 is the drop radius, r_d is the radius of the drop contact area with the substrate, H_d is its height, and θ is the contact angle (Figure 39b).

a. 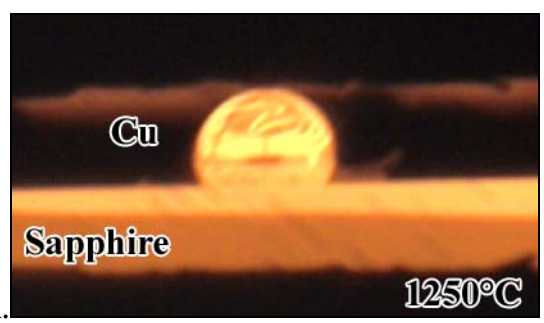

b. 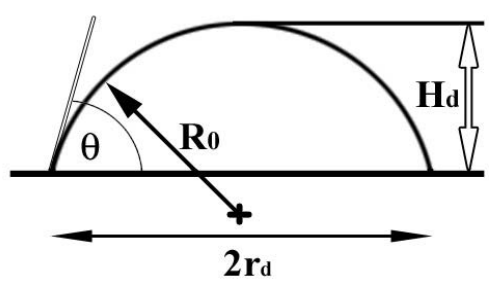

Figure 39. a) Image of a Cu sessile drop on (0001) sapphire recorded *in-situ* at a temperature of 1250°C. b) Schematic drawing of the geometrical parameters used to determine the contact angle.

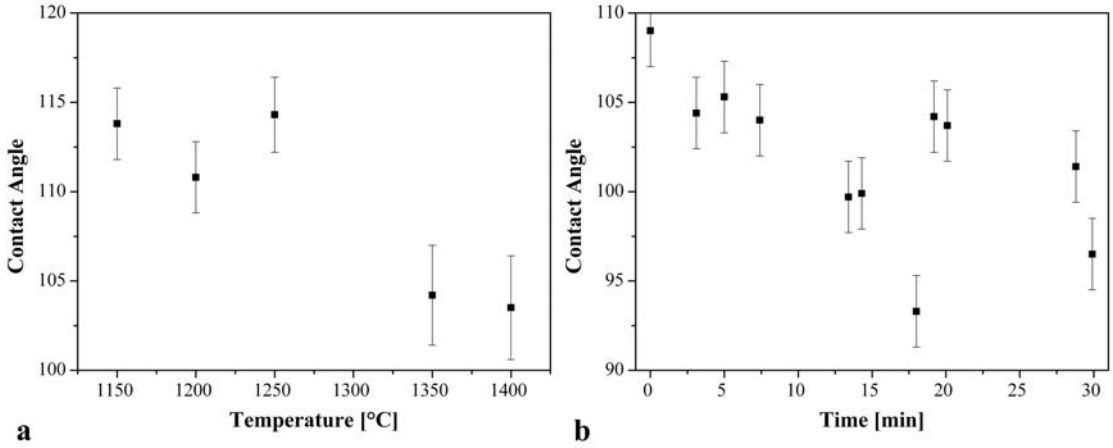

Figure 40. Graphs of Cu on sapphire (0001) contact angle as a function of a) temperature and b) time (at a temperature of 1400°C). These experiments were performed without anorthite glass.

The measurement of the Cu contact angle on sapphire as a function of temperature and time is given in Figure 40. There is a small decrease in the contact angle from 113° to 103° in the given temperature range (1150°C-1400°C). The measured contact angles are lower than ones reported for the Cu-sapphire system under non oxidizing conditions [10], however they fall in the range that may be expected under oxygen adsorption ($P(O_2)$ in the range of $8x10^{-13}$-$8x10^{-5}$ Torr) to the Cu-sapphire interface [12,13], which is below the detection limit of the system used in the experiment (~10^{-9} Torr).

The wetting experiments were performed under a vacuum of 10^{-3} Torr to enable measurement of the residual gases. These conditions, together with the high temperature, resulted in a high evaporation rate of the metal drop, and in some cases more than 2/3 of the initial drop mass was lost during the experiments. The evaporation of Cu resulted in the oscillatory behavior of the contact angle as a function of time seen in Figure 40. This is a known phenomenon [11,89] occurring due to evaporation and pinning of the metal drop to reaction rings, followed by retraction of the drop. The reaction rings are formed on the substrate during high temperature wetting [11]. In the optical micrograph presented in Figure 41, a number of reaction rings are visible. An example of the Cu pinned to a reaction ring is shown in Figure 42.

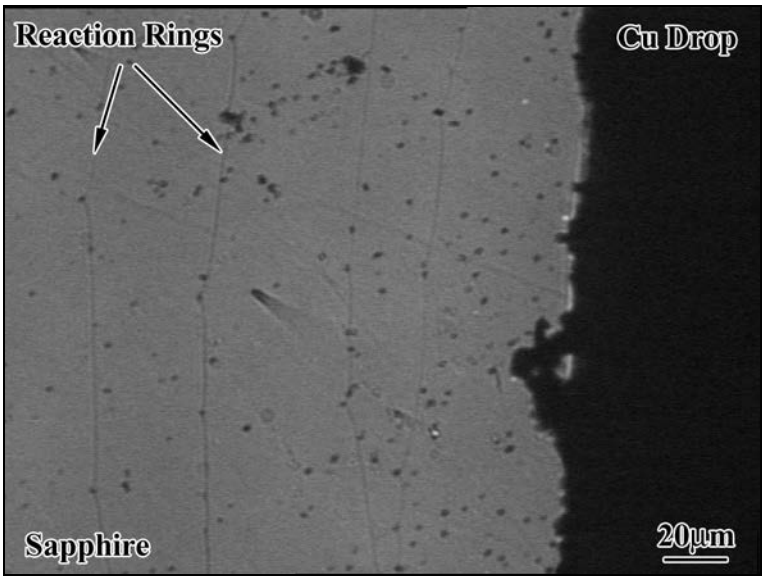

Figure 41. Optical light microscope micrograph of reaction rings formed on a sapphire substrate, observed in the areas where the Cu drop receded.

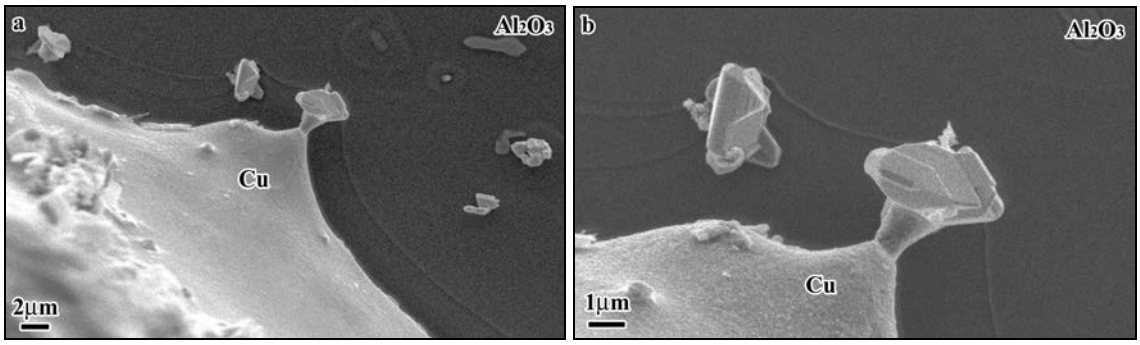

Figure 42. SEM micrograph showing the pining of the Cu drop to the sapphire substrate.

3.2.2. Wetting of Ni on Al_2O_3

Sessile drop experiments of Ni on sapphire (0001) substrates were performed in the presence and absence of anorthite glass. The results of the contact angle measurement as a function of temperature and time (at 1600°C) are presented in Figure 43. Similar to Cu on sapphire, a small decrease in the contact angle is observed with increase in temperature. The contact angles obtained fit well with results reported by Levi *et al.* [33] for this system under the same working conditions. The oscillating behavior, due to the evaporation and pinning of the drop, can be seen in the graph of the measured contact angle as a function of time (Figure 43b).

Anorthite glass was specifically prepared for the wetting experiments. The glass obtained after heat treatment was transparent in the center of the crucible, while adjacent to the walls of the alumina crucible the material was opaque. EDS measurements were performed on each one of the glass areas. Each area was measured at 15 different points. The results are presented in Table 12. For the wetting experiments glass pieces taken from the central area were used.

Table 12. EDS measurements performed on the anorthite glass taken from the center of the crucible and from the region immediately adjacent to the crucible wall.

Location	Al [at.%]	Si [at.%]	Ca [at.%]	Remarks
Central Area	40.5 ± 0.23	40.0 ± 0.66	19.5 ± 0.78	Experimentally Measured
Close to Wall	43.9 ± 1.6	35.8 ± 2.2	20.3 ± 3.5	Experimentally Measured
Anorthite	40	40	20	Theoretical Values

Figure 44 presents a series of images taken at different temperatures of a Ni drop together with anorthite glass. The melting temperature of the eutectic glass in air is 1500°C. In the conditions used in the experiment (total pressure of 10^{-3} Torr and $P(O_2)<10^{-11}$ Torr) the anorthite melted at ~1575°C. These experiments were repeated with very small amounts of glass in order to enable better observation of the Ni drop shape as a function of time. In the presence of glass, the drop shape does not show any oscillatory behavior, as seen in the absence of glass. It should be noted that the Ni drops in these experiments also lost 50-66% of their initial mass due to evaporation.

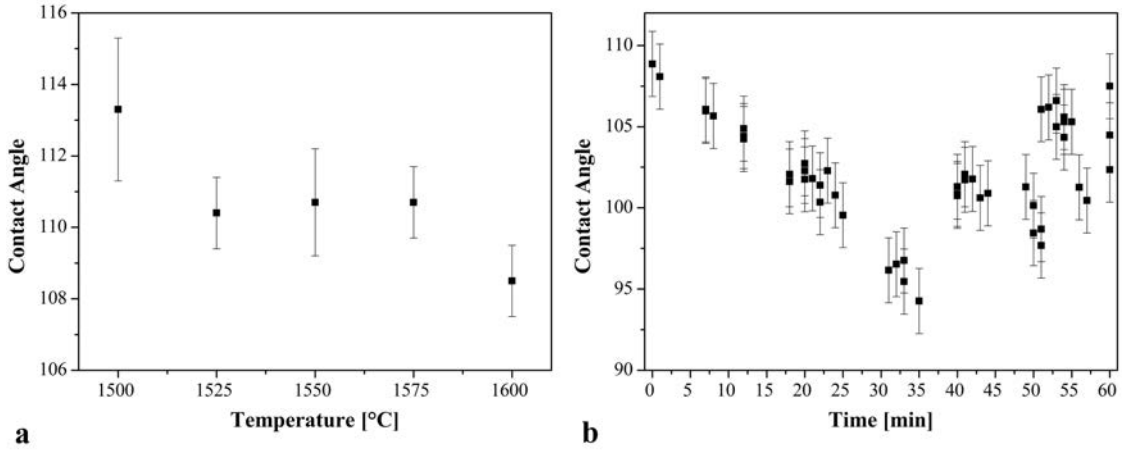

Figure 43. a) Dependence of the contact angle of Ni on (0001) sapphire as a function of temperature and b) time (at 1600°C), in the absence of anorthite glass.

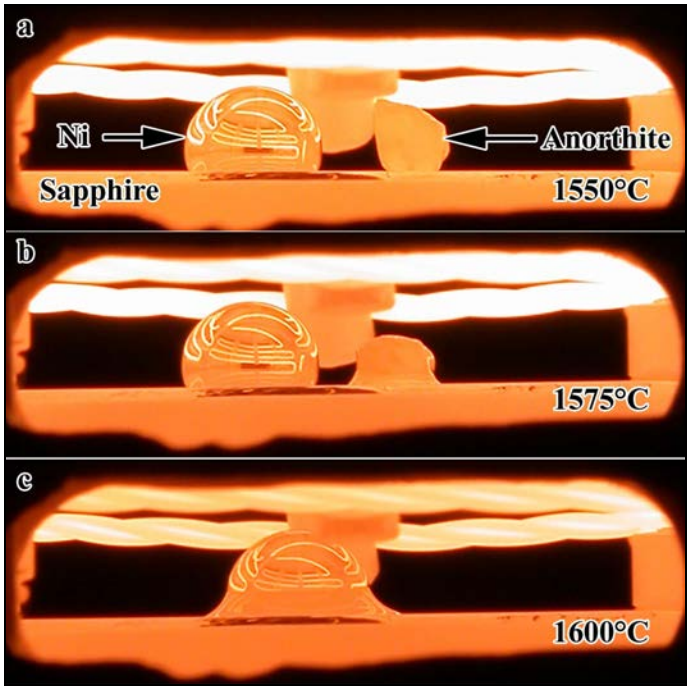

Figure 44. A series of images from a wetting experiment of a Ni drop next to a piece of anorthite glass as a function of temperature. The anorthite starts melting around 1575°C and surrounds the Ni drop.

XPS and Auger measurements were conducted on the samples to determine whether the glass spread on the surface of the sapphire (indication of a possible surface film) and as an attempt to measure "segregation" or evidence of a glass film at the metal-alumina interface. Samples of Ni drops on sapphire after sessile drop experiments were fractured to expose the interface for analysis (Figure 45). The Ni drop from the sample without glass was easily detached from the substrate, and the fracture occurred along the interface resulting in flat fracture surfaces (Figure 45). A few reaction rings are visible on the sapphire substrate. In the glass-containing samples, no reaction rings were

observed in the area from where the drop retracted. Attempts to fracture these samples at the Ni-alumina interface failed, and in two different samples that were fractured, the crack advanced through the sapphire substrate (Figure 45b), making it impossible to investigate the Ni alumina interface by XPS.

XPS analysis of the glass free sample detected the presence of a small amount of Ca and Ni (1.6at.% 1.35 at.% respectively) on the sapphire substrate in the area where the drop was originally located. These values are equivalent to 0.1ML and 0.05ML (monolayers) respectively. Measurements performed outside the area where the Ni drop was detached from, recorded only tungsten (other than Al, O and C), probably due to the tungsten heating elements. On the Ni drop surface no Ca, Si or Al were observed.

Auger and XPS analysis conducted on the glass-containing sample indicated the sapphire surface (surrounding the Ni drop area) contained Si and Ca segregation. To determine whether the Ca and Si presence on the surface was a result of surface diffusion or evaporation/condensation, another experiment was performed where a clean sapphire substrate was placed adjacent to a sapphire substrate with anorthite glass on top. The samples were placed 2mm apart without direct contact between the samples. The measurements on the clean sapphire revealed no Ca or Si (only W was detected).

Values measured in each one of the methods were different. This may be due partially to charging of the alumina when performing the Auger analysis, as well as the use of different samples. The Auger measurements of the Ca/Si ratio measured far from the glass drop (>50μm) showed a Ca/Si ratio of 0.54±0.14 averaged from 5 measurements.

The XPS measurements also indicated that Ca and Si spread on the entire sapphire substrate upon which the anorthite was placed, although the concentration and the Si to Ca ratio was not constant. In all the XPS measurements the combined value of the Si and Ca in terms of layers fluctuated around 0.3±0.1ML (3-5at.%). This value seems low, but the measurements on the glass drop as well resulted in low concentrations ~0.6ML (11at.%). These results may indicate that a surface layer was formed on the sapphire. (The detection limit was an order of magnitude lower than the reported values).

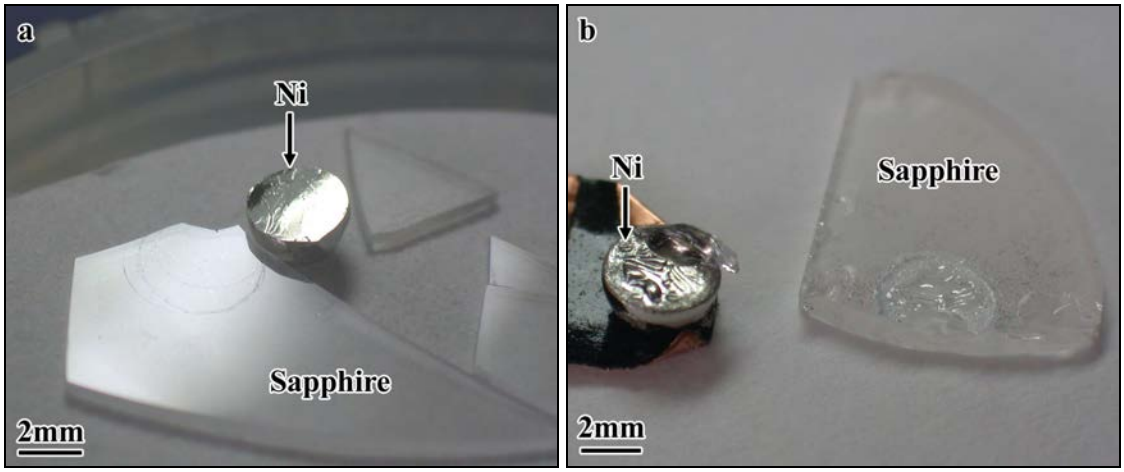

Figure 45. Images of the fractured samples after sessile drop experiments used for XPS measurements of the Ni-alumina interface chemistry; a) a sample after an experiment without anorthite, and b) a sample after an experiment in the presence of anorthite glass.

In order to measure the influence of Ca and Si on the contact angle of Ni on sapphire, a sessile drop experiment was conducted with a *small* anorthite glass particle placed relatively far from the Ni drop (5mm), and the gradual change in the contact angle was monitored (Figure 46). The contact angle measured as a function of temperature (Figure 47a) does not reflect the equilibrium contact angle, but the momentary value measured during heating to 1600°C (at each point the temperature was held for 2 minutes to obtain the image, and then the heating was resumed). Once a temperature of 1600°C was reached the contact angle was measured for 30 min (Figure 47b). No oscillatory behavior of the contact angle was observed. The contact angle decreased as a function of time from ~99° to ~80° within the measured time. SEM images taken from the area where the Ni drop receded (due to evaporation and retraction upon solidification) showed only one reaction ring (Figure 48a). The area exposed contained faceted Ca rich particles (qualitatively measured by EDS due to the electron interaction volume) having an average size of a few microns (Figure 48b). These particles were investigated by AFM (Figure 49) and EBSD.The faceted morphology can be clearly observed in Figure 49. The height of the investigated particles ranged from 0.2-0.4μm. EBSD analysis of the particles indicated they have a hexagonal symmetry, and they share the same (0001) normal direction as the sapphire substrate. Between the different particles measured, only the normal direction is maintained.

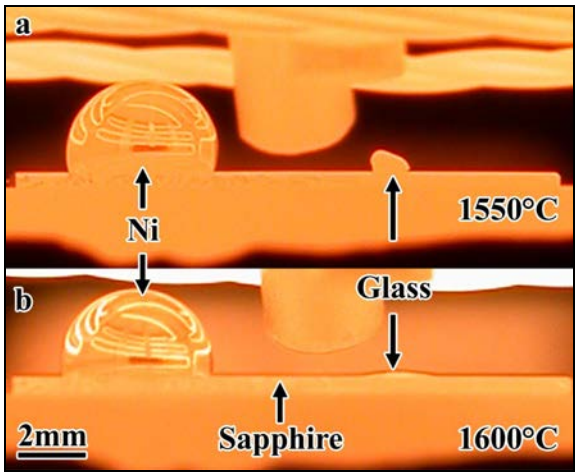

Figure 46. Image of a sessile drop in the presence of a glass anorthite placed far from Ni drop (about 5mm) a) before the melting of the anorthite glass and b) after the glass melting at 1600°C.

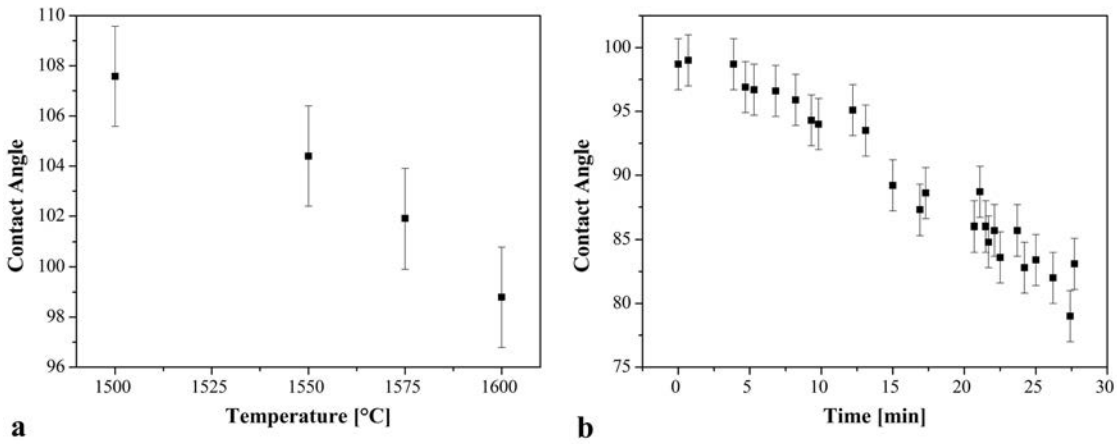

Figure 47. Graph of contact angle as a function of time and temperature with anorthite glass present far from the Ni drop.

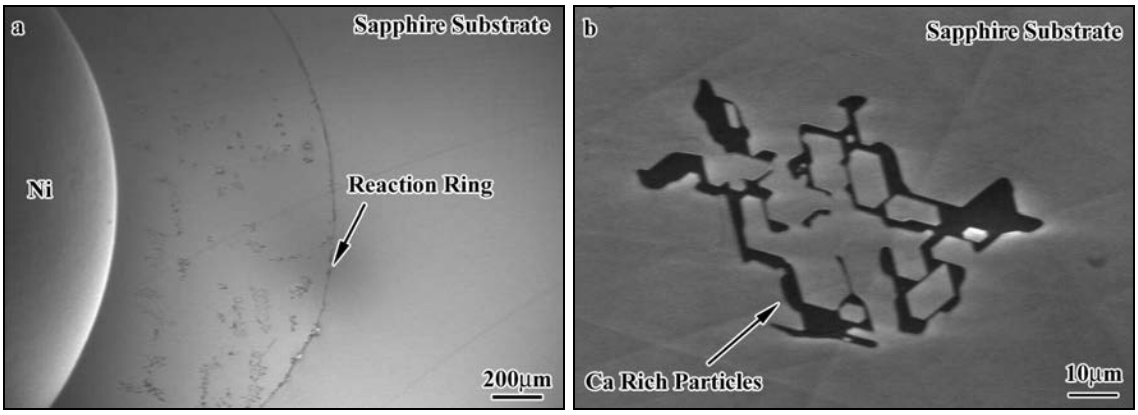

Figure 48. SEM micrographs of a) part of the Ni drop together with one reaction ring where the original drop extended (particles formed in the area exposed by the receding Ni drop can be seen), b) a high magnification image of the Ca rich particles observed within the area exposed under the Ni drop.

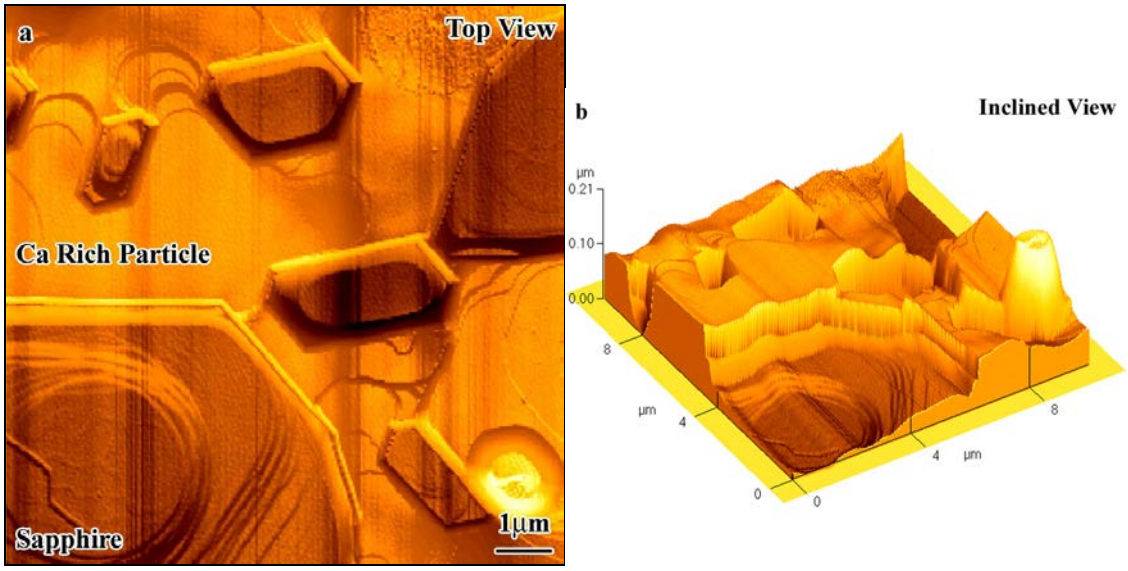

Figure 49. AFM scan of a Ca rich particle a) a top view showing the faceting of the particle, b) an inclined view of the same area showing the 3D morphology of the particle.

3.2.3. Wetting of Anorthite on Al_2O_3

Wetting experiments of anorthite on sapphire were conducted both in air and in the UHV furnace. Sessile drop experiments of anorthite glass on (0001) sapphire in the absence of the metal drop were performed, and the contact angle was measured as a function of time at 1600°C. Figure 50 presents a series of images taken of the anorthite glass on sapphire at different temperatures (conducted in the UHV furnace). The contact angle stabilized after 15 minutes at 9°±2° (Figure 51). Flaitz *et al.* [90] performed a wetting experiment with a slightly different glass composition on sapphire, cut at a 60° angle from the c-axis, at a temperature of 1500°C and obtain a contact angle of 10°. Although the conditions are not identical to the ones used in the present study, the values are in the same range.

The wetting experiments of anorthite on sapphire usually resulted in fracture of the sapphire substrate (for both atmospheres) after cooling. This behavior is most probably due to differences in the expansion coefficients between the two materials.

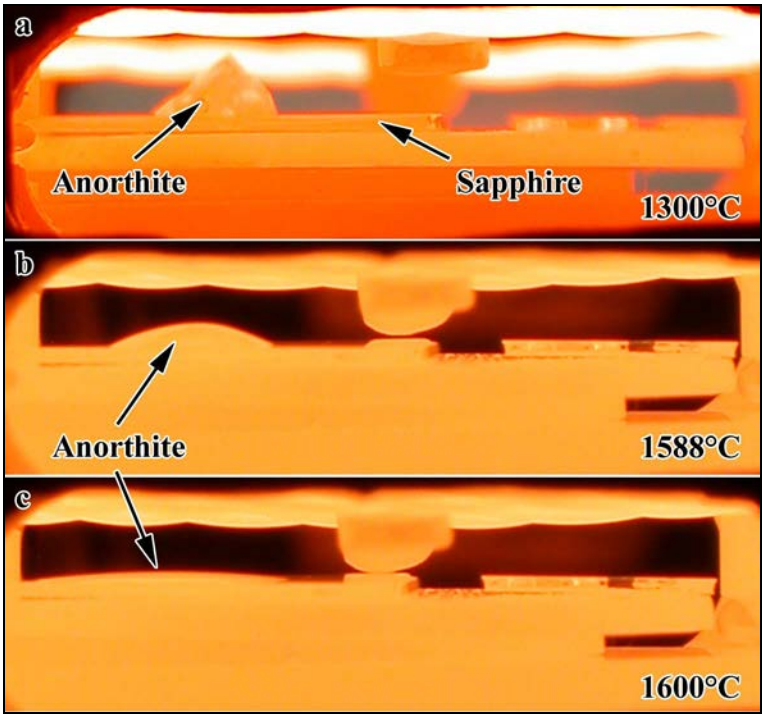

Figure 50. A series of images from a sessile drop experiment of anorthite glass on a (0001) plane sapphire as a function of temperature.

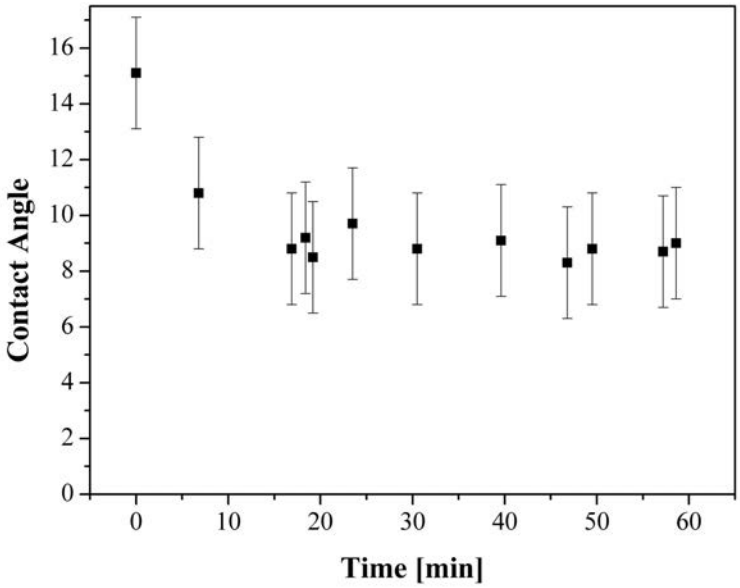

Figure 51. Dependence of the contact angle of anorthite glass on (0001) sapphire as a function of time at 1600°C.

3.3. Dewetting Experiments

The advantage in dewetting experiments is that they enable us to stabilize the system at lower temperatures due to the smaller amount of material involved. This allows for the investigation of interface behavior in the *solid –solid* regime. This section presents some preliminary results from dewetting experiments carried out with Cu, and Ni + anorthite glass on $(1\bar{2}10)$ and (0001) sapphire substrates respectively.

3.3.1. Dewetting of Cu on Al_2O_3

The dewetting experiments of Cu on sapphire focused mainly on determining the working conditions (temperature and time) suitable for carrying out the heat treatment. Working under vacuum (total pressure of 10^{-3} Torr), and a large surface area results in a high evaporation rate of the metal. For the Cu dewetting experiments, 2μm layers were sputtered on sapphire substrates. The experiments were performed at temperatures of 800°C, 900°C, and 1000°C for various times (the Cu was in the solid state). At a temperature of 800°C treatments of up to 21h resulted mainly in grain growth and faceting of the Cu (Figure 52a). After 4 hours at 900°C the Cu layer partially dewetted (Figure 52b) and after 7 hours fine micron size Cu drops were formed on the sapphire surface (Figure 52c). Heat treatments for 4 hours at 1000°C resulted in evaporation of almost the entire Cu layer (Figure 52d), resulting in features resembling the reaction rings on the sapphire surface.

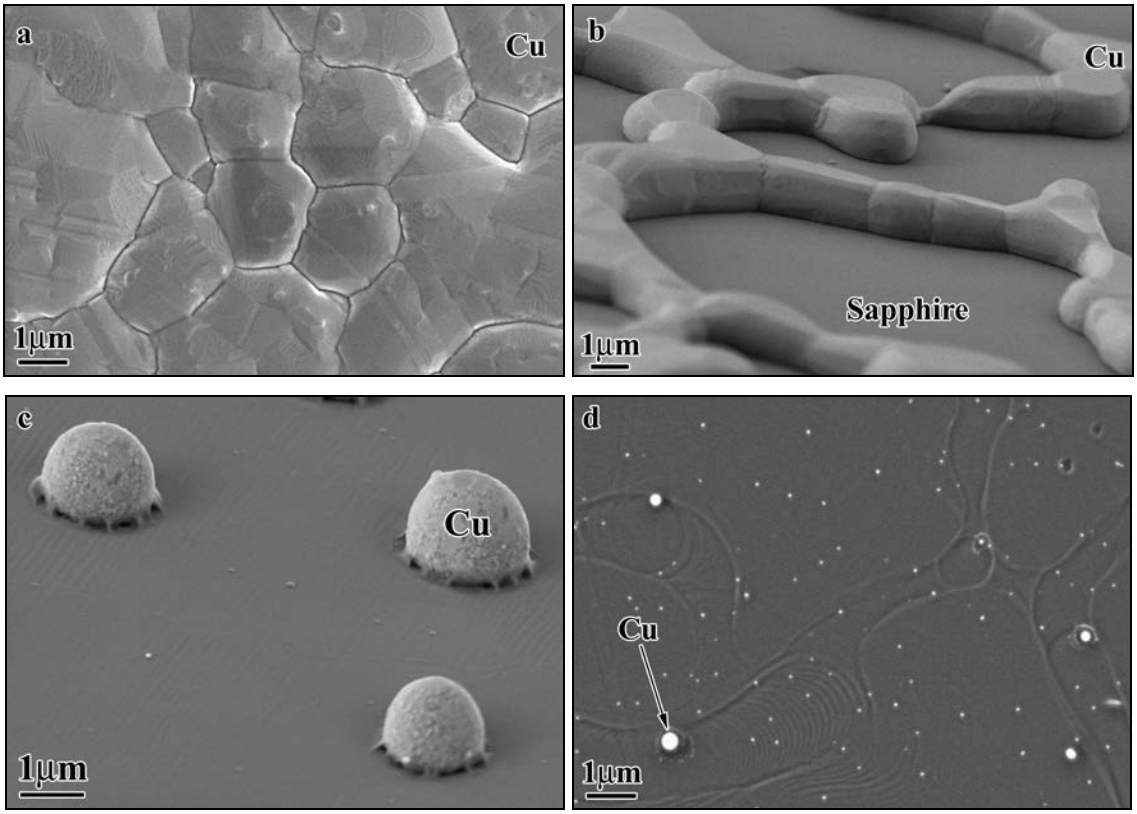

Figure 52. SEM micrographs of Cu dewetting on $(1\bar{2}10)$ sapphire substrates carried out at a) 800°C for 4 hours, b) 900°C for 4 hours, c) 900°C for 7 hours, and d) 1000°C for 4 hours (the small white spots are due to the carbon coating).

3.3.2. Dewetting of Ni on Al_2O_3 + Anorthite

For the Ni dewetting experiment in the presence of anorthite a (0001) sapphire substrate was prepared with an *equilibrated* anorthite glass drop (1600°C). A 2μm Ni layer was then sputtered over the entire surface. The heat treatment was carried out at 1600°C and a total pressure of 100 Torr. The Ni layer was only partially dewetted, and formed glass tendrils extending along the Ni particles' boundaries (Figure 53). Some drops were observed on the Ni particles. Qualitative EDS analysis taken from these areas showed they consisted of the glass elements (Figure 54). Two distinct contact angles were measured from seven such particles; three with $\theta = 63° \pm 2°$ and four $\theta = 75° \pm 2°$. Since EDS analysis of these particles was only qualitative, it was not possible to relate the behavior to drop composition. However, it is clear that their formation involved the dissolution of glass on the substrate and diffusion to the Ni surface. This resembles observations reported in wetting of Ni on sapphire where alumina particles were observed at the Ni drop surface [89].

At the edge of the original anorthite drop (not shown in the image), small drops, and flat faceted particles were formed (at the right side of the Ni particles seen in Figure 53).

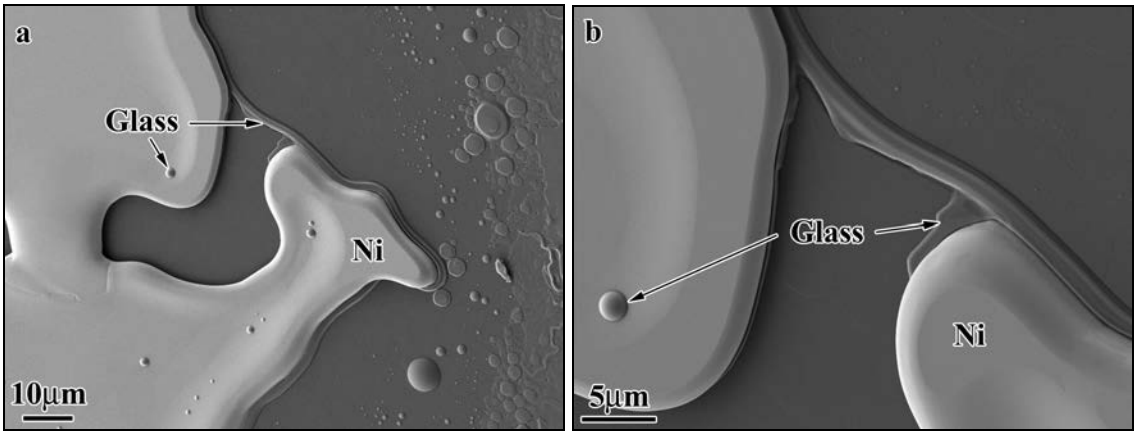

Figure 53. SEM micrographs of Ni dewetting on sapphire in the presence of anorthite glass. a) the Ni particle is seen together with a glass tendril surrounding the original boundary of the particle, on the right side of the particle the glass formed drops and faceted particles on the sapphire surface, b) a high magnification of the Ni particle boundary and the glass tendril, and glass drop formed over the Ni particle.

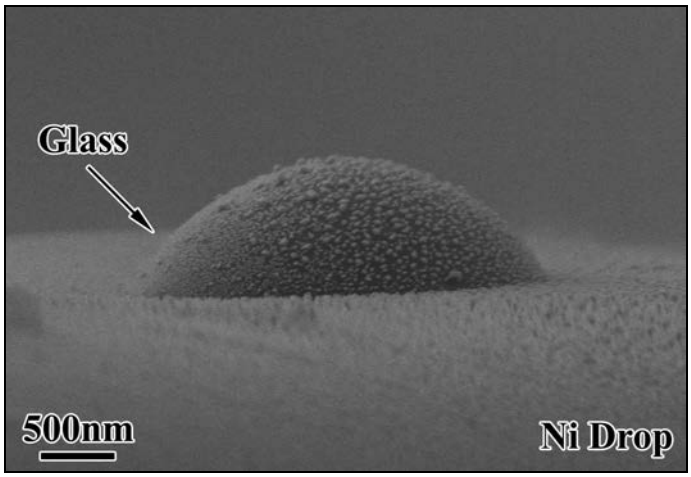

Figure 54. A SEM micrograph of a glass drop formed on a Ni drop. The glass drop formed a 63° ± 2° contact angle with the Ni surface. Small gold particles from the conducting coating can be seen over the entire area.

A *cross-section* prepared by focused ion beam (FIB) through a Ni drop in this sample is shown in Figure 55. The glass ridge (tendril) formed at the triple junction can be seen at a higher magnification in Figure 55b. The Ni forms an angle of 150° ± 5° between the ridge/tendril and the sapphire substrate. A few glass tendrils, which detached from the receding Ni particles, were measured and found to be ~130nm high.

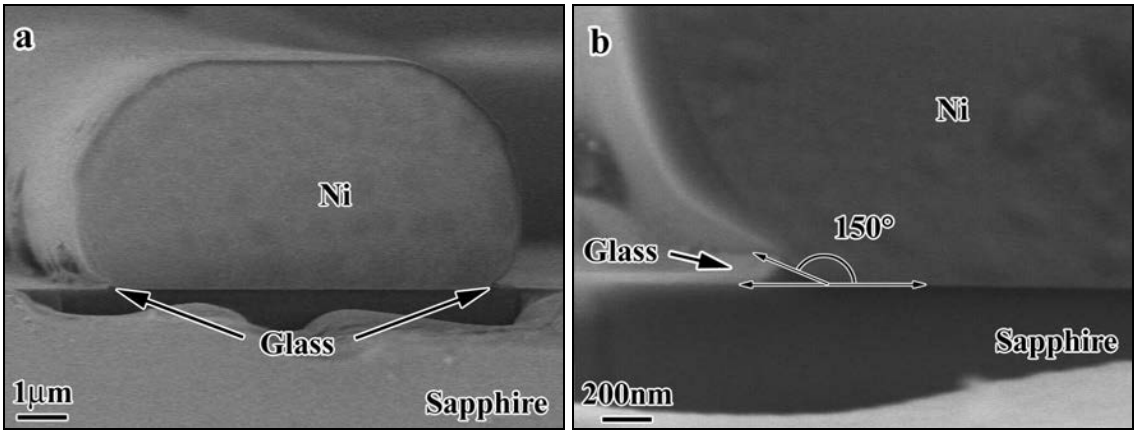

Figure 55. SEM micrographs of a cross-section from the Ni dewetting droplets for measurement of the dihedral angle between the sapphire substrate and the Ni particle.

4. DISCUSSION

In this chapter the results and models regarding intergranular film formation at metal-ceramic interfaces are discussed. The first section is dedicated to the experimental findings relevant to the film stability. The second section is dedicated to a theoretical calculation based on Clarke's model, modified to treat the metal-ceramic interface. The discussion will conclude with examples of the influence of intergranular films on the microstructural evolution in composite materials.

4.1. Equilibrium Films at Metal-Alumina Interfaces

Equilibrium intergranular films are reported in a growing number of *ceramic* systems [14,15,24,50,52,54]. However, as a result of the report by Scheu *et al.* [23] on intergranular films at Cu-alumina interfaces, the question was raised whether these films are in fact limited to ceramic systems, or if equilibrium films can exist at metal-ceramic interfaces.

4.1.1. Intergranular Film Stability in Metal-Alumina Composites

Structural Aspects

The experimental results shown in this work clearly indicate the stability of intergranular films at metal-alumina interfaces (in the doped composites). HRTEM analysis of *both* (Ni and Cu) types of metal-alumina interfaces revealed the presence of intergranular films with a constant film thickness at all metal-alumina interfaces (Figure 24, Figure 35, and Figure 36), with the exception of only one case where a partial film was found (Figure 38). Films were found at the metal-alumina interfaces for particles located at alumina grain boundaries, *and* particles located (occluded) within alumina grains (Figure 27, Figure 28). It should be emphasized that the sintering process was performed at a high temperature, involving significant mass transport and grain growth (from a 0.3μm powder to 5-10μm size grains), so the presence of intergranular films at the end of the sintering process is an indication of their stability. The fact that these films persist even after occlusion of the metal particles by the growing alumina grains

supports this conclusion. In addition, the composites were prepared using different sintering conditions (temperature, total pressure and $P(O_2)$).

The Ni-alumina interface that was observed with a partial film was an interface defined by a low-index orientation relationship between the alumina and Ni grains. From reports on films in ceramic systems, it is known that at "special" (low-energy) grain boundaries no films are formed [15,40]. In fact the same behavior was observed in the present study, where general high-energy alumina grain boundaries were found to possess an intergranular film (Figure 22), while a Σ3 alumina grain boundary (Figure 37) was found without a film.

In Si_3N_4 composites reinforced with SiC particles, it was found that for some low energy interface orientations no films were formed, whereas for high energy interfaces an intergranular film was present [91]. Kaplan *et al.* [92,93] reported the presence of Ca segregation at Al-alumina interfaces as well as at a basal twin in a composite prepared by infiltration of Al into a porous alumina sample. However, these samples did not contain a high enough concentration of glass forming additives to form glass pockets and intergranular films. Both interfaces are known to have a lower energy than Ni-alumina interfaces [10,89]. The partially dry Ni-alumina interface in the present study may have had some Ca and Si segregation. However, due to the large electron beam diameter used for its characterization, it was not possible to detect any excess.

This still leaves as an open question whether a dry Ni-alumina interface with a special orientation relationship has a lower interfacial energy than an interface with a film?

Normally the answer would be no, since the Ni-alumina is a high energy interface. However, if the results report by Levi [89] of Al enrichment at the Ni-alumina interface due to dissolution of the sapphire are taken into account, this could lower the interfacial energy and together with the observed orientation relationship may result in a further decrease in the interfacial energy. On the other hand, it could very well be that the interface was in the process of being infiltrated by the film, since this interface was the only case observed of a partial film.

HRTEM analysis of the films revealed only a slight difference in the film thickness between the two types of metal. The average thickness of the films at Ni-alumina interfaces and Cu-alumina interfaces was 0.87±0.1nm, and 1.0±0.1nm respectively (for the (0001) α-Al_2O_3 terminating plane). In the Ni-alumina doped composite, films at rhombohedral terminating planes were found to be thicker than alumina basal-planes. However, in the Cu-alumina doped sample the results were reversed, the rhombohedral and prismatic-planes had thinner films than the basal-plane. In Scheu *et al.'s* [23] study, the films found at the Cu-alumina interfaces showed a similar behavior to the Cu-alumina interfaces in the present study, although the thickness measured for the rhombohedral-planes was significantly lower than in the present work (0.4-0.6nm and 0.8nm respectively). This issue is discussed in the following.

Some of the intergranular films at Ni-alumina interfaces appeared to be partially ordered (Figure 35), although the contribution of the microscope operating conditions (objective lens defocus and lens aberrations) to the appearance of partial ordering remains to be investigated. Ordering at interfaces between crystalline and amorphous (liquid) phases has been experimentally demonstrated [68], and has recently been investigated in depth by molecular dynamic studies [29,30]. In particular simulations performed by Garofalini and co workers showed ordering of SiO_2 at the glass-alumina interface, which was increased by additions of Ca which segregated to the interface and stabilized cage-like structures of SiO_2 tetrahedras [21,22]. However, more observations are needed to confirm that the structure seen at the interface is a result of ordering of the IGF rather than an imaging effect.

In the undoped samples no glass pockets or intergranular films were observed at the alumina grain boundaries or metal-alumina interfaces. However, EDS analysis of the interfaces performed in STEM, and WDS measurements conducted on the bulk material in SEM, indicated the presence of Si and Ca impurities. These were probably the cause for the bright contrast observed at the interfaces in the HRTEM micrographs (Figure 29). The fact that the low levels of impurities did not result in an interfacial film indicates the need of a threshold amount of bulk impurities to form intergranular films.

Scheu *et al.* [23] reported that no films were found at the alumina grain boundaries, only at Cu-alumina interfaces. The samples investigated by Scheu *et al.* had a slightly higher

impurity level (SiO_2 0.08 at% and CaO 0.04 at%) than found in the undoped samples in the present work (SiO_2 0.04 at% and CaO 0.006 at%). These results may imply that intergranular film formation at the metal-alumina interfaces was preferred over the grain boundary, possibly due to a larger reduction of the free energy. However, to confirm this assumption the stability of the films under the reported [23] working conditions would have to be investigated. It is interesting to point out that thermal etching performed on the Cu-alumina doped samples (Figure 13) resulted in exudation of glass from the sample to the grain boundary grooves at a temperature very similar to the one used to infiltrate samples investigated by Scheu [23]. Kleebe *et al.* [76] and Luo *et al.* [24] showed in different systems that the film stability in some cases depends on the temperature, and changes in thermodynamic parameters causes the film to withdraw from the interface. It is possible that under the sample preparation conditions in Scheu's study the films at the alumina grain boundaries were not stable, and only the films at the Cu-alumina interfaces were retained. In studies of model alumina grain boundaries [94,95], a wetting-dewetting transition was suggested to occur at the free surface of alumina. Exudation of glass from the boundaries was observed to occur at temperatures above ~1600°C, possibly forming a surface film, and on cooling glass droplets formed on the surface due to instability of the film. Thermodynamic calculations performed by Brada *et al.* [58] suggested as well the possibility of such a behavior.

Could grain boundary films withdraw at a temperature of 1300°C and stabilize at the Cu-alumina interfaces? The answer is probably yes. At these temperatures exudation of glass to grain boundary grooves was observed in the current study, and the film at the Cu-alumina interface should be able to form via enhanced diffusion in the presence of liquid Cu [12]. This effect was observed in the dewetting experiments of Cu on sapphire, where even at a temperature of 1000°C there was dissolution of the sapphire substrate (Figure 52).

Chemical analysis of the interfacial films indicated they consisted of Ca and Si, resulting from the introduced dopants, since no films were observed in the *undoped samples* although they were contaminated during processing. EDS analysis of the *alumina grain boundaries* in the Cu-alumina and Ni-alumina *glass-doped* composites showed a small variation in the Ca:Si excess concentration ratio: 1:1.9 and 1:1.5 respectively. The *Cu-alumina* interfaces in the doped samples showed a similar Ca:Si excess ratio (1:2.1) to the grain boundaries (Si rich). This is comparable to the Ca:Si concentration ratio of anorthite, and a similar result was reported by Powell-Dogan *et al.* [16]. On the other hand, the *Ni-alumina* interfaces were found to be significantly *Ca rich* with a Ca:Si ratio of *1:0.2*. However, unlike the Cu-alumina samples there is a very significant difference in the Ca:Si ratio between the alumina grain boundaries and the Ni-alumina interfaces within the same sample. This result is important since it indicates that the metal has an influence on the film chemistry. The difference in interface behavior between the Ni and Cu may possibly be a result of the low $P(O_2)$ which was maintained during the experiment with the Ni-alumina composite. For both Ni and Cu there is a dependence of the contact angle with alumina on the $P(O_2)$, even below pressures needed to form oxides or aluminates, due to oxygen adsorption to the metal-alumina interface [10,12,13]. The fact that the $P(O_2)$ at which the two composites were prepared was in different regimes (the Cu–alumina in the oxygen adsorption regime while the Ni-alumina was in the reduction regime) may have influenced the segregation behavior at the metal-film interface, thereby modifying the film composition.

It is interesting to note, that although bulk EDS analysis of the samples showed a wide distribution in the Ca composition within each sample, as well as between the samples, the alumina grain boundary Si:Ca ratio in both composites was relatively constant. This is emphasized, since both composites originated from the same initial doped alumina sample, which was cut into three parts and then infiltrated by the metal. The sol-gel process used to introduce the SiO_2 resulted in a uniform distribution in the samples. However, Ca infiltration resulted in a wide distribution in concentration. The glass doped alumina and Cu-alumina composite were Ca rich, resulting in the formation of CA6. In the glass doped Ni-alumina composite, which was Si rich, no CA6 was observed.

The EDS analyses revealed that for both composites the triple junction pockets consist of a Si rich glassy phase containing Al and Ca. In the Cu-alumina composite the glass pocket composition was richer in Si (see Table 3 and Table 8). An EDS line-scan performed between an alumina grain and a Cu particle across a glass pocket confirmed the EDS spot measurements (Figure 23). In the Ni-alumina samples the glass pocket composition was found to have a higher Ca concentration than the Cu-alumina sample. This can be readily understood, since the reaction of Ca with alumina to form CA6 reduced the Ca concentration in the glass phase, and left the triple junction pockets richer in Si. In the Ni-alumina sample, no CA6 formed and the glass pockets had a higher Ca/Si ratio. Figure 56 presents a ternary phase diagram of CaO-Al_2O_3-SiO_2 together with the compositions of the triple glass pockets measured for both composites.

Tanaka *et al.* [50] showed that changing the bulk concentration of Ca resulted in alteration of the equilibrium film thickness at Si_3N_4 grain boundaries. Gu *et al.* [75] investigated the same samples and found that increasing the Ca bulk concentration up to a threshold of 220ppm increased the Ca concentration in the film. However, above this value, the Ca concentration in the film remained constant although the film thickness continued to increase. There appeared to be some dependence of the thickness on the N:O ratio but it was not precisely confirmed. Due to the high level of doping used in the samples in the present study, it is possible that all samples are above this kind of threshold segregation.

Some similarity may be found with the study reported by Gülgün *et al.* [96], in which different levels of doping were added to alumina samples and the resulting grain boundary composition was measured. An increase in yttrium doping resulted in an increase in yttrium grain boundary segregation, until a plateau value was reached, which correlated to the formation of a second phase (YAG). This is analogous to the glass reservoir or CA6 formation in the present study. A dependence of the film thickness on the film chemistry was also observed for grain boundary films in ruthenate resistors [53]. In the present study, a difference in alumina grain boundary film thickness was measured between the two composites. However, since only one film was measured for each case it is not possible to conclude if this represents a general behavior.

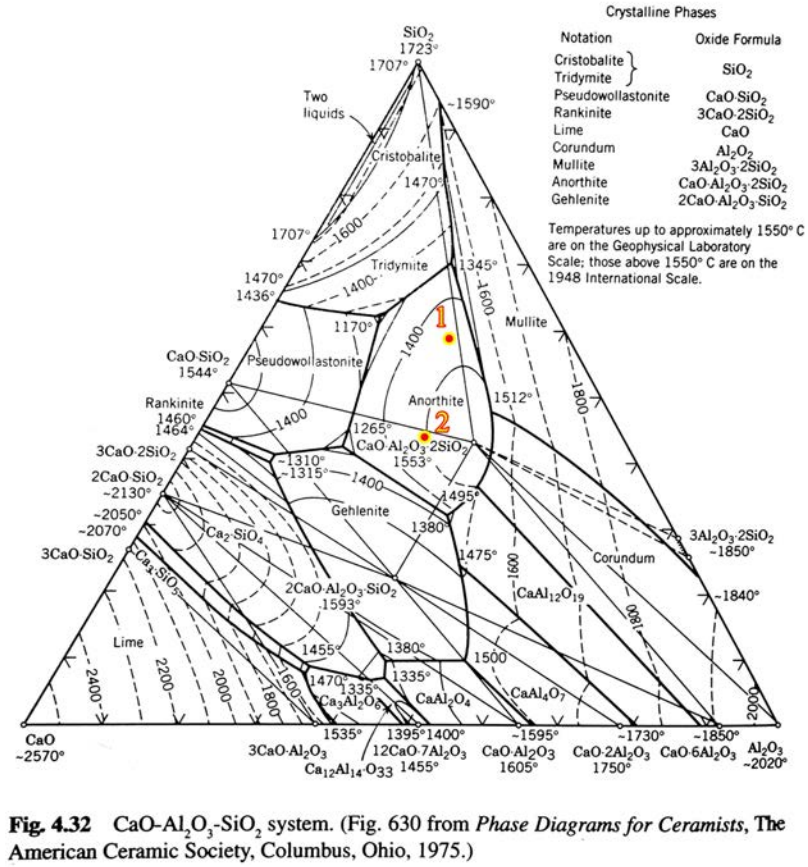

Fig. 4.32 CaO-Al_2O_3-SiO_2 system. (Fig. 630 from *Phase Diagrams for Ceramists*, The American Ceramic Society, Columbus, Ohio, 1975.)

Figure 56. Ternary phase diagram of CaO-Al_2O_3-SiO_2 system [47]. Points 1 and 2 represent the measured glass pocket composition in the Cu-alumina and Ni-alumina doped samples, respectively.

These results indicate that the film thickness cannot be merely explained based on the alumina surface anisotropy, but a more intricate behavior exists, including the influence of the metal on the film through modification of the chemical composition. In this sense it is very important to correlate the thickness measurements to the composition of the film (this wasn't technically possible in the present study).

In a line-scan performed between a Cu particle and an alumina grain across a glass pocket it was found that Ca segregated to the alumina surface, while Al and possibly some Ca segregated to the Cu particle surface. The same behavior of Ca segregation to the Cu and alumina surfaces was reported by Scheu *et al.* [23]. Molecular dynamics simulation performed by Bolonski *et al.* and Litton *et al.* [21,22] predicted such segregation of Ca to the alumina-film interface. This type of measurement should be repeated on the Ni-alumina doped sample to determine a possible difference in segregation behavior.

4.1.2. Intergranular Films in Wetting Samples

In the composite samples the processing was such that the powder was first coated by a thin SiO_2 layer; due to the sol-gel process, and only later was the metal introduced into the sample. Based on the results from the composite samples it is evident that the films at metal-alumina interfaces are stable; however one may question whether the film formation may be route dependent, as was suggest by Ackler and Chiang [77,78].

The wetting experiments of Ni on sapphire in the presence of anorthite glass carried out in this study were designed to address this question. To date no direct observation (HRTEM imaging) of the Ni-sapphire interface from the wetting experiments was obtained. However, the results reported in this study hint towards the presence of such a film at the interface.

In the wetting experiment of both metals on sapphire in the absence of glass, the wetting behavior (contact angles, multiple ridge formation) was similar to that reported under similar working conditions [10-13,89]. However, once the glass was introduced an important difference in behavior was observed; the lack of reaction ring formation, and consequently no oscillatory behaviour. The Ni drop shape was stable throughout the experiment, although there was a weight loss of more than 60%. A cross-section taken from one of the Ni drops in the presence of anorthite showed a “ridge-like” feature at the triple point between the Ni and sapphire. EDS mapping and spot measurements indicated the feature was glass, with a composition of 30.4% at. Al_2O_3, 42.1% at. SiO_2, 27.5% at. CaO. The deweting experiments showed a similar result. The tendrils seen in plan-view in Figure 53 serve as an example, and a cross-section view of one such tendril is seen at the triple point with the Ni and sapphire in Figure 55. The penetration of the glass into the triple junction resembles the morphology observed at metal-alumina triple junctions in the composite samples. Another indication of the penetration of glass elements to the Ni-sapphire interface is the contact angle measured as a function of time in the wetting experiment performed with a glass drop located 5mm from the Ni drop (Figure 46). The contact angle measured for Ni on sapphire in the absence of glass is l08°±2° (at a temperature of 1600°). In the presence of glass, the angle decreased to 80°±2° within 30 minutes (Figure 47). A change in contact angle from non-wetting (θ>90°) to partial wetting (θ<90°) cannot occur without a reduction in

the interfacial energy. Such a behavior may occur due to pinning [11,89], which is not the case in the present study. According to Young's equation any absorption to the drop surface reducing the surface energy would result in an increase of the contact angle (provided the γ_{SV} and γ_{SL} are constant). A reduction in γ_{SV} will also result in an increase of the contact angle. It is actually expected that both these energies were reduced during the experiments. XPS measurements indicated Ca and Si spreading on the sapphire surface, and the presence of glass drops on the Ni in the dewetting experiment (Figure 54). In the wetting sample of Ni with glass located away from the metal drop (Figure 46), only one reaction ring was formed at the original triple line, which was probably due to the lower melting temperature of Ni relative to the glass, and the time needed for the glass elements to diffuse to the edge of the Ni drop. Evidence of the fact that glass elements reached the Ni drop was found in the form of crystalline particles on the sapphire surface in the area exposed by Ni evaporation. These particles were relatively large, a few microns across and a thickness of 100-200nm. The particles may have formed due to destabilization of the film once the Ni drop retracted. EDS analysis of these particles indicated they were Ca rich and contained some Si. A Ca:Si ratio of ~1:0.2 was measured (based on two such particles). From the EDS results the exact composition of the particles cannot be determined since a 10kV beam was used, resulting in an interaction volume extending ~0.7μm into the sample, which is more than three times the particles thickness. Given this limitation, the value does correlate to the Ca rich layers found in TEM observations in the Ni-alumina composite. The wetting experiments were performed under the same pressure used to prepare the Cu-alumina composite (unlike the Ni-alumina composite). This is significant, since one possible explanation given for the difference in film composition between the Cu and Ni interfaces was the $P(O_2)$. If however, the pressure does not effect the concentration it indicates the Ni presence determined the film composition. However, the analysis was from a bulk phase on the sapphire surface, therefore this value should be taken with some reservations.

The nature of the intergranular films found at the metal-alumina interfaces in the present work is similar to that observed at grain boundaries. The presence of the films is always associated with glass pockets found at triple junctions, from which the film extends. The intergranular film composition differs from that of the glass pockets. Most importantly, the film thickness along the interfaces is constant, with a standard deviation of ±0.1nm

[14,15,50,55]. According to Clarke's model the equilibrium film thickness in ceramic systems can be modeled using a colloid-like force balance [15]. The experimental results shown in the present study clearly show the stability of the films, but can the Clarke model be applied to a metal-ceramic interface as well?

4.2. Forces at Metal-Alumina Interfaces

The van der Waals (vdW) force is considered as the dominate attractive force in Clarke's model, while the dominant repulsive force is a steric disjoining force resulting from ordering induced on the amorphous film by the crystalline grains at both sides of the interface, with possible contributions from electrical double layers and/or other repulsive forces. This model was used as the basis for calculation of the force balance for a number of different systems [15,50,54,56,97], using various approaches to estimate the Hamaker coefficient [61,64-66].

To date, the calculation of the van der Waals force in the context of intergranular films has been performed *only* for ceramic systems, but it is by no means limited to them. The London dispersion force is active between any two atoms [61,63]. In fact, the force was calculated between parallel metal plates by Casimir [61] (at T=0°K) before it was applied to bulk ceramic systems. The van der Waals contribution to the adhesion of "dry" metal-ceramic interfaces has been estimated by Lipkin *et al.* [38] and Didier *et al.* [39].

4.2.1. Hamaker Coefficient Calculation

Israelachvili [38,63] showed, that using the Lifshitz continuum approximation of the van der Waals force, the Hamaker coefficient for the case of two solids interacting through a third medium can be expressed by an integral in the following manner:

$$(20)\quad H_{\alpha\beta\gamma} \approx \frac{3}{4}kT\left(\frac{\varepsilon_{\alpha(0)}-\varepsilon_{\beta(0)}}{\varepsilon_{\alpha(0)}+\varepsilon_{\beta(0)}}\right)\left(\frac{\varepsilon_{\gamma(0)}-\varepsilon_{\beta(0)}}{\varepsilon_{\gamma(0)}+\varepsilon_{\beta(0)}}\right)+\frac{3\hbar}{2}\int_{\nu_1}^{\infty}\left(\frac{\varepsilon_{\alpha}(i\nu)-\varepsilon_{\beta}(i\nu)}{\varepsilon_{\alpha}(i\nu)+\varepsilon_{\beta}(i\nu)}\right)\left(\frac{\varepsilon_{\gamma}(i\nu)-\varepsilon_{\beta}(i\nu)}{\varepsilon_{\gamma}(i\nu)+\varepsilon_{\beta}(i\nu)}\right)d\nu$$

where $\varepsilon(i\nu)$ is the frequency dependent dielectric constant for the different (α, β, γ) phases, ν is the frequency, k is Boltzmann's constant, T is the absolute temperature, and $\hbar$ is Planck's constant divided by 2π. The frequency dependent term is integrated from the thermal frequency ν_1 to infinity (practically it is performed up to ~100eV since above this value the retardation length is of the same order of the atomic spacing and its contribution becomes negligible) [61,63,98]. The first term in the expression is the zero frequency term and consists of the Debye and Keesom contribution to the van der Waals

force. The second term in equation 20 is the frequency dependent term and accounts for the London dispersion interactions [38,63]. Using the equation in this form demands knowledge of the dielectric properties over the entire integration range. These values are not readily available for most materials. However, the calculation may be performed by use of the Ninham-Parsegian representation [61,63,64]. This calculation yields a relatively accurate value of the Hamaker coefficient by representing the frequency dependent dielectric constant with a set of oscillators at specific adsorption frequencies [61,63,64,66,99]. For alumina and a SiO_2 based glass film it is sufficient to use only two frequencies; one in the infrared (IR) and one in the ultraviolet-visible (UV) range to calculate the Hamaker coefficient [63,64]:

$$(21) \qquad \varepsilon_{ceramic}(i\nu) = 1 + \frac{\varepsilon_{ceramic}(0) - n_{ceramic}^2}{1 + \nu / \nu_{rot,ceramic}} + \frac{n_{ceramic}^2 - 1}{1 + \left(\nu / \nu_{e,ceramic} \right)^2}$$

where $n_{ceramic}$ is the refractive index, $\nu_{rot,ceramic}$ and $\nu_{e,ceramic}$ are the absorption frequencies in the IR and UV, respectively. However, since the integration is performed from the thermal frequency, the infrared term can be neglected, which results in an expression depending on the refractive index of the material and the adsorption frequency in the ultraviolet-visible range [38,63]:

$$(22) \qquad \varepsilon_{ceramic}(i\nu) \approx 1 + \frac{n_{ceramic}^2 - 1}{1 + \left(\nu / \nu_{e,ceramic} \right)^2}$$

For the metal, the static dielectric constant is infinite, thus its zero-frequency term cancels. The frequency dependent dielectric permittivity can be calculated based on the jellium approximation [38,63]:

$$(23) \qquad \varepsilon_{metal}(i\nu) = 1 + \left(\frac{\nu_{e,metal}}{\nu} \right)^2$$

where $\nu_{e,metal}$ is the plasmon frequency. The plasmon frequency can be obtained experimentally or calculated [100,101]:

$$(24) \qquad \nu_{e,metal} = \left(\frac{n_e e^2}{\pi m} \right)^{\frac{1}{2}}$$

where n_e is the free electron density, m is the electron mass, and e is the electron charge.

For the metal-ceramic case the Hamaker coefficient may be written as (α – being the ceramic material, β the film and γ the metal):

$$(25) \qquad H_{\alpha\beta\gamma} \approx \frac{3}{4}kT\left(\frac{\varepsilon_{\alpha(0)}-\varepsilon_{\beta(0)}}{\varepsilon_{\alpha(0)}+\varepsilon_{\beta(0)}}\right)+\frac{3\hbar}{2}\int_{\nu_1}^{\infty}\left(\frac{\varepsilon_{\alpha}(i\nu)-\varepsilon_{\beta}(i\nu)}{\varepsilon_{\alpha}(i\nu)+\varepsilon_{\beta}(i\nu)}\right)\left(\frac{\varepsilon_{\gamma}(i\nu)-\varepsilon_{\beta}(i\nu)}{\varepsilon_{\gamma}(i\nu)+\varepsilon_{\beta}(i\nu)}\right)d\nu$$

Once the frequency dependent dielectric constants for the different phases are expressed by the given approximations, the Hamaker coefficient can be calculated. The plasmon frequency of the metals used for the calculation are presented in Table 13. These were obtained both from the literature and calculated for comparison. Table 14 contains parameters from the literature, needed to calculate the Hamaker coefficient for alumina, and some possible film compositions. The values chosen to represent the alumina for the calculations in this work are from Lipkin *et al.* [38], since they represent up to-date values of the refractive index and absorption frequency [61]. The values used for the bulk materials (metals and alumina) have been used in a number of other studies, and do not vary much. The difficulty is in the choice of parameters for the intergranular film. Clarke *et al.* [15,56] used SiO_2 parameters for the intergranular films at alumina grain boundaries. However, the results presented in this study and others [14,16,23,55,75] clearly indicate the presence of Ca and Al in the film. Reported measurements of the film thickness at alumina grain boundaries range between 1.2-2nm [14,55] (the grain boundary film thickness measured in the present study fall in that range). Brydson *et al.* [14,55] reported a 4-12 atom/nm^2 Ca+Si excess for these alumina grain boundaries. Given these values, it is clear the film consists predominantly of Al cations, since in a volume of 1nm^3 there are 47 Al atoms in bulk alumina or in SiO_2 ~23 Si atoms. A few more examples of cation number per 1nm^3 of other phases are given in Table 15. Therefore, the dielectric constant, the refractive index and absorption frequency should be modified.

The calculation of the Hamaker coefficient was first performed based on the properties of a SiO_2 film, and compared to results reported in the literature for alumina grain boundaries, and then the consequence of films consisting of different compositions (that include CaO and Al_2O_3) are discussed.

Table 13. Plasmon frequency values used for the calculation of the Hamaker coefficient.

Material	$\nu_{e,metal}$ [1/s]		
Cu	3.70×10^{15}	4.6×10^{15}	4.66×10^{15}
Ni	3.84×10^{15}	4.7×10^{15}	5.00×10^{15}
Reference	Calculated	[38]	[100]

Table 14. Parameters of different materials needed to calculate the Hamaker coefficient.

Material	Formula	$\nu_{e,ceramic}$ [1/s] UV	Refractive Index	ε(0)	Ref
Alumina	Al_2O_3	3.0×10^{15}(est)	1.75	11.6	[63]
Alumina		3.2×10^{15}	1.77		[38]
Alumina			1.77		[61]
Alumina			1.76-1.768		[102]
Alumina		3.21×10^{15}	1.752		[66]
Alumina		3.18×10^{15}	1.753	10.1	[64]
Fused Quartz	SiO_2	3.2×10^{15}	1.448	3.8	[63]
Fused Quartz		3.23×10^{15}	1.536	4.29	[64]
Fused silica		3.24×10^{15}	1.448	3.82	[64]
Anorthite crystalline	$CaAl_2Si_2O_8$		1.572-1.588		[102]
Anorthite crystalline			1.585		[70]
Anorthite crystalline				5.47-8.76*	[103]
Anorthite Amorphous				7.5*	[103]
Mullite	$Si_2Al_6O_{13}$		1.64	6.2	[70,104]
Lime	CaO		1.84	12	[72]

est – estimated *Values measured at 1MHz, $\nu_{e,ceramic}$ are the absorption frequencies in the IR and UV

Table 15. Number of cation per nm^3 of a few Al_2O_3-CaO-SiO_2 based phases.

Phase	Ca at./nm^3	Si at./nm^3	Al at./nm^3	O at./nm^3	Total # Cations at./nm^3
SiO_2	0	23.40	0	46.80	23.40
$CaAl_2Si_2O_8$	5.97	11.94	11.94	47.75	29.84
Ca_3SiO_5	23.86	7.95	0	39.77	31.81
Al_2O_3	0	0	47.33	70.99	47.33

The calculations were performed using Mathematica 4.2 (Wolfram Research, Inc.). To confirm the calculation procedure they were first performed for a "dry" metal-alumina interface following the work of Lipkin *et al.* [38]. The results are presented in Table 16. The values calculated here are in good agreement with the ones reported in the original work by Lipkin *et al.*, and the small differences are probably due to the approximations used by Lipkin *et al.* for the solution of the Hamaker coefficient (in the present study the Hamaker coefficient was calculated analytically based on equation 20).

Calculations were then performed for an *alumina grain boundary* in the presence and absence of a SiO_2 based film. These results were compared to values found in the literature, and are presented in Table 16. The calculated Hamaker coefficient for the alumina grain boundary are in very good agreement with the values reported in the literature by French [61] and Bergström [51]. It is interesting to note that the van der Waals contribution for the force in the case of a metal-alumina interface is actually higher than the alumina grain boundary (see Table 16).

Table 16. Comparison between Calculated Hamaker Coefficients and values taken from the literature. ($zJ=10^{-21}J$)

Geometry	French [61] [zJ]	Bergström [64] [zJ]	Lipkin [38] [zJ]	Present work Calculation [zJ]
H [Al_2O_3-Vac- Cu]			244	241
H [Al_2O_3-Vac- Ni]			247	245
H [Al_2O_3-Vac- Al_2O_3]	164.9	150-160		163.7
H [Al_2O_3-SiO_2- Al_2O_3]	26.2	26.9 - 27.1		28.3

As was pointed out, some uncertainty exists concerning the absolute composition and elemental distribution within the intergranular films, which of course influence the parameters used. for the computation. The calculation of the Hamaker coefficient (given the approximation used in this work) demands three parameters: the static dielectric constant, the refractive index (n), and the UV absorption frequency. The possible effect on the Hamaker coefficient due to changes in each one of them will now be considered.

The static dielectric constant determines the contribution of the zero frequency term, which at most may reach 0.75kT. This term was neglected in some works [15,38,50,56] since it is relatively small, especially for the case of an interface/grain boundary interacting across a vacuum medium at room temperature. Even in the presence of an intergranular film, it usually contributes less than 10% to the Hamaker coefficient. However, for a metal-ceramic interface at high temperatures its absolute contribution can be significant. In the zero frequency term, the term belonging to the metal has a value of 1, since the metal has an infinite static dielectric constant. Consequently, the value of the zero frequency term is left at its maximum, and only the ceramic interaction with the film may reduce it. However, if the refractive index of the film is high (decreasing the contribution of the frequency dependent term as will be shown) and a large difference exists in the static dielectric constant between the film and bulk ceramic, the term may become significant (0.75kT at the sintering temperatures used in the present study can reach ~20zJ). Nevertheless, for a given set of materials parameters the calculated Hamaker coefficient dependence on temperature is weak (as will be shown later).

The refractive index and the UV absorption frequency determine the frequency dependent term. First, the influence of the refractive index was investigated. The refractive index of various compositions of SiO_2-CaO and SiO_2-Al_2O_3 are presented in Figure 57 [85]. The dependence of the refractive index on the composition is almost linear. Once added to SiO_2, both, CaO and Al_2O_3 contribute to the *increase* of the refractive index. In Figure 58 the refractive indexes taken from another source are presented as a function of the ternary composition [102]. Although the dependence of the refractive index on the composition is less obvious in Figure 58, it can be seen that an increase in CaO and Al_2O_3 results in an increase of the refractive index.

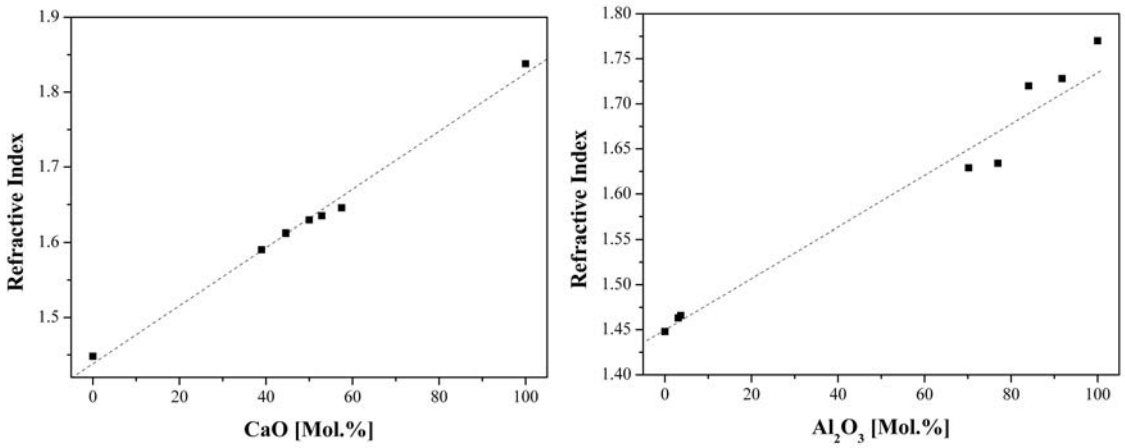

Figure 57. The refractive index dependence on (a) SiO_2 - CaO and (b) SiO_2 - Al_2O_3 relative composition [**85**].

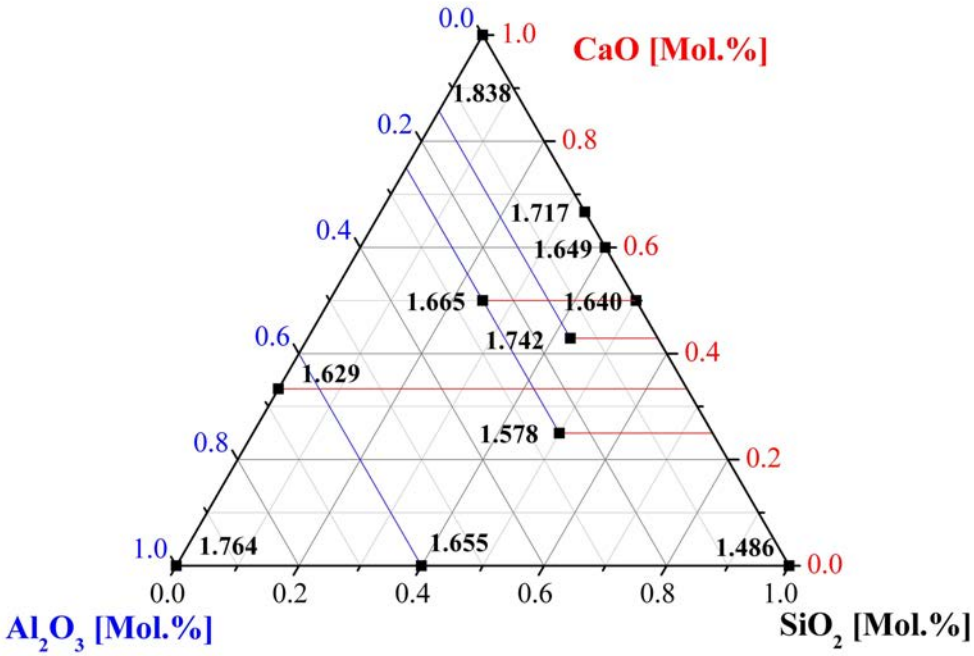

Figure 58. Refractive index values for different SiO_2 - CaO - Al_2O_3 compositions [102].

The dependence of the Hamaker coefficient on the refractive index was evaluated using amorphous SiO_2 parameters for the dielectric constant and UV absorption frequency and a range of refractive indexes that may be expected (Figure 59). The most significant implication arising from the resulting calculation is the fact that the Hamaker coefficient is positive. This means an *attractive force* exists at the metal-alumina interface containing an intergranular film. Such a force is the prerequisite for the formation of an equilibrium intergranular film, according to Clarke's model.

Similar to "dry" interfaces, the Hamaker coefficient for the metal-alumina interface in the presence of a SiO_2 film is higher than for the alumina grain boundary for any given film. In fact, even the lower values of the metal-alumina interface Hamaker coefficient (for higher refractive index of the film) are still higher than most of the alumina grain boundary values. This is significant, since the intergranular films at metal-alumina interfaces were observed to be *thinner* than the grain boundary films, in this work and for values reported in the literature for grain boundary films in alumina [14,55]. From Figure 59 it is clear that an increase in refractive index results in a decrease of the Hamaker coefficient.

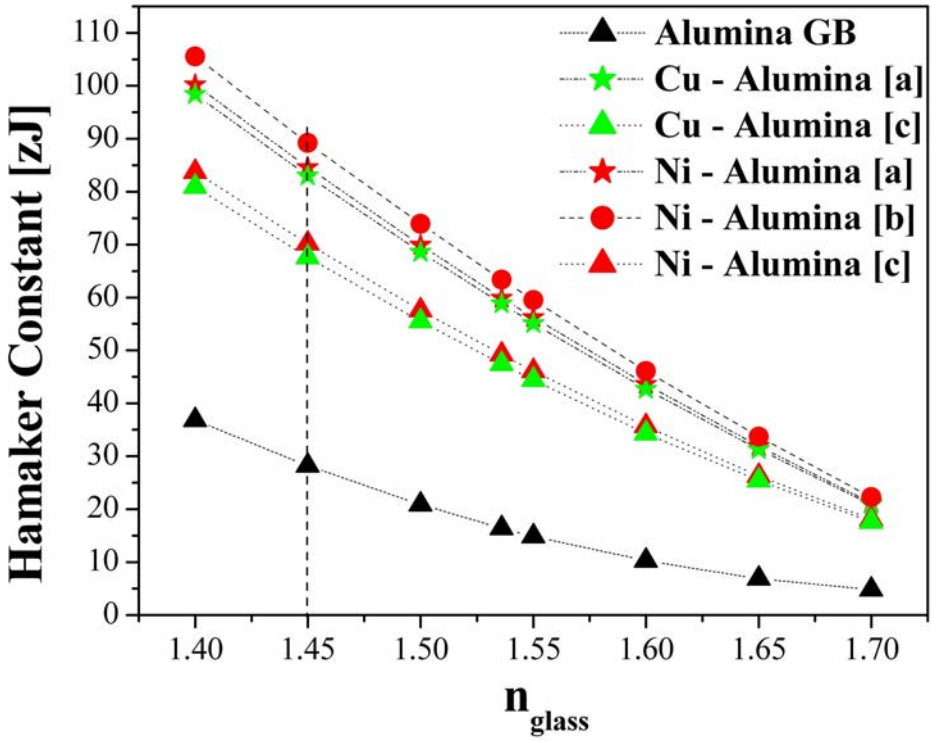

Figure 59. Calculated Hamaker coefficient versus refractive index of the intergranular film for the alumina grain boundary and the two metal-alumina interfaces, using different plasmon frequencies taken from different sources (a - Lipkin *et al.* [38], b – Egerton [100], and c – calculated).

There is practically no difference in the Hamaker coefficient between Cu-alumina and Ni-alumina interfaces. The values obtained by using the calculated plasmon frequencies resulted in slightly lower values than the ones taken from the literature. This may be a result of known deviations in the calculated values relative to the measured ones [101]. (The Cu-alumina interface curve based on the plasmon frequency from Egerton [100] was not drawn, since it is identical to the one based on Lipkins *et al.* [38] values).

Absorption in the UV range is related to electronic excitation and the band gap of the material [65,72,105]. SiO_2 and Al_2O_3 have very similar band gaps; 8.3-8.5eV and 8.8eV respectively [47,72] and their adsorption frequencies are 3.21×10^{15} and 3.24×10^{15} Hz respectively [64]. To evaluate the dependence of the Hamaker coefficient on the absorption frequency, values between 2×10^{15}- 4.1×10^{15} Hz were used. This range was chosen since it represents boundary values of possible intergranular film chemistries. For the lower boundary we assume the film has a composition similar to anorthite. Based on its optical properties (and a fast photospectroscopic scan which was performed) its absorption should be above 6eV ($\lambda \approx 200$nm). Since Y_2O_3 and ZrO_2 have band gaps in that range, their adsorption frequencies were taken as the lower limit. At the upper limit it is expected that the band gap would not be much higher than alumina. Since the upper limit is more critical, a band gap of 12eV was chosen. LiF and MgF_2 have band gaps in that range, and therefore their absorption frequencies were taken. All the values of the different phases are presented in Table 17.

Table 17. Upper and lower boundaries of absorption frequencies used for the Hamaker coefficient calculation [47,64,72].

Phase	Band Gap [eV]	Absorption Frequencies [Hz]
Y_2O_3	5.5	2.15×10^{15}
ZrO_2	5.8	2.13×10^{15}
LiF	12	4.03×10^{15}
MgF_2	11.8	4.06×10^{15}

For the calculation of the Hamaker coefficient as a function of the absorption frequency, the refractive index of quartz (1.536) was chosen to represent the intergranular film, since some degree of ordering in the film is expected, and since both Al and Ca contribute to an increase in the refractive index.

It can be seen from Figure 60 that even for a relatively large range of adsorption frequencies the Hamaker coefficient for the metal-alumina interface in the presence of an intergranular film still results in a positive value. As an extreme estimate, the Hamaker coefficient was calculated assuming a refractive index of 1.7 and an adsorption frequency of 4.0×10^{15}Hz, which resulted in a value of 10zJ. Although this a

low value, it is still positive, however it is probably a large *under* estimation of the coefficient.

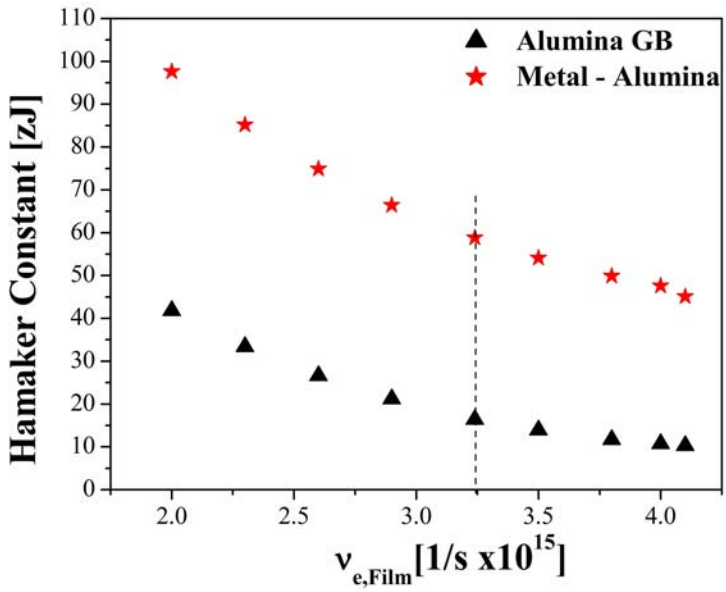

Figure 60. Calculated Hamaker coefficient versus absorption frequency of the intergranular film for the alumina grain boundary and metal-alumina interface. The absorption frequency value used for the previous calculations is marked by a dashed line on the graph.

The dependence of the Hamaker coefficient on temperature for a given interface is very weak as can be seen from the calculation performed for the alumina grain boundary and metal-alumina interface in Figure 61. It is important however to clarify that this does not imply the temperature will not affect the film behavior, but merely that the force is not expected to change as a function of temperature for a stable film composition.

It is quite clear from these calculations that the van der Waals force for the metal-alumina interface in the presence of an intergranular film will be an attractive force, and allow a force balance that may equilibrate the film. Moreover, the attractive force at a metal-alumina interface is stronger than for an alumina grain boundary, and this is in good agreement with the film thickness measured in the present study (and by Scheu *et al.* [23]).

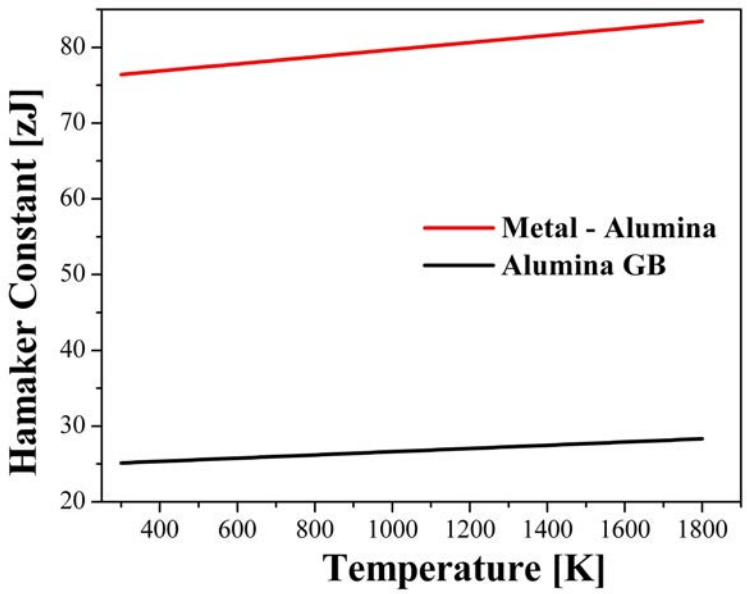

Figure 61. Calculated Hamaker coefficient versus temperature for the alumina grain boundary and metal-alumina interface in the presence of an intergranular film.

An alternative calculation was preformed by Johnston and Finnis [106] based on an image force approach for the Cu-alumina interface using a density functional method. In the same study, they performed a simplistic calculation attempting to obtain the van der Waals force for the Cu-alumina interface. However, their calculated value is too low by an order of magnitude, based on the calculation performed in the present work. On the other hand, the value they obtained from the image force model was an order of magnitude higher than the value presented in the current work. If their image force calculation is correct, this would mean the image force is the dominant attractive force at the metal-ceramic interface. However, two questions should be raised; in what way do the image and van der Waals force differ, and is the force obtained in their calculation realistic?

The difference between the image force approach and the van der Waals calculation is not entirely clear. The van der Waals interaction clearly emerges from electrostatic considerations, as does the image force. The approach introduced by Lifshitz [62] provides a calculation tool for bulk materials using a continuum approach, at the expense of performing the calculation for cases where the materials are in close proximity (interatomic distance ~0.3nm).

The value Johnston *et al.* [106] reported for an image force at a 1nm thick film, is equivalent to a Hamaker coefficent of 1300zJ (for this given separation). This is a very high Hamaker coefficient, which is larger than at a metal-alumina interface separated by a vacuum, and even larger than values for the force between two metal surfaces [63]. Having stated this, in ceramic systems with intergranular films subjected to pressures of 40MPa during creep tests (which is in order of magnitude suggested by Johnston *et al.* [106]) the films, although thinner, were still stable [51]. Another point that should be taken into account is that their calculation introduces a Ca distribution in the film that contributes to the calculated force. It would be interesting to calculate whether this distribution serves to increase the attractive force or screens the interaction between the metal and alumina as in the Hamaker force calculations. This only emphasizes the need for an accurate measurement of the film composition and element distribution within the film to allow more accurate calculations of the forces.

Although it may seem that their calculated attractive force is rather high, it cannot be dismissed at this stage. If it is correct, it still supports the conclusions reached based on the present experimental findings.

4.2.2. Interfacial Force Balance

Estimation of the force balance leading to the equilibrium thickness of the intergranular films is rather speculative at this point. The calculation of the Hamaker coefficient is well founded from colloid science both experimentally and theoretically. In the context of intergranular films, work mostly led by French [19,53,61,73,74] in collaboration with different groups have yielded experimental data directly measured from the interface using electron energy loss spectrums from the low loss range [73], and bulk parameters from optical spectroscopic methods [74], backing the calculated values.

Different qualitative attempts to try and explain the effect of the films' chemical composition on the thickness and stability are usually based on intuitive assumptions of the role of impurities in the film (being a glass modifier or network former), and were

shown in some cases to be in error, as in Tanaka *et al.* [50] and Gu *et al.* [75] reviewed earlier.

In their model Clarke *et al.* [15,56] introduced a frame-work in which various attractive and repulsive forces may be dealt with. The van der Waals force has been thoroughly examined in the previous section. Another possible attractive force is the capillary pressure. It has been reported in a study of intergranular films found in ruthenate resistors immersed in a liquid matrix, that even in the absence of capillary pressure the films can still equilibrate [53]. However, in other studies it was less clear whether capillary pressure can be ignored since polycrystalline alumina deflocculates when immersed in a glass melt, (i.e. without capillary force) [90,107].

Estimated values of the capillary pressure using a silicate based melt used for liquid phase sintering are between 1-12 MPa for a meniscus with a radius of 1-0.1μm respectively [47,70]. The pressure that is expected at the final stages of the alumina sintering is probably at the lower range. This should be quantitatively evaluated since it may be significant in the force balance and in some cases it may be the dominant force rather than the van der Waals force. As a comparison, the van der Waals force acting at a metal-alumina interface calculated in the present work across a 1nm film is 2-4MPa (for a Hamaker coefficient of 40-80zJ respectively). For an alumina grain boundary this value goes down to ~1MPa.

On the other hand the repulsive forces (both steric and double layer) take the form of:

$$\textbf{(26)} \qquad F_{rep}(h) = Ae^{-h/\xi}$$

where A is a constant which may be replaced by physical coefficients for each case (see section 1.3). This exponential form decays faster than the inverse power law of the van der Waals force (thereby balancing the film thickness). However, if the thickness is too large, retardation has to be taken into account, which would further reduce the van der Waals force.

We will proceed to analyze the force balance for the steric forces; these can be extrapolated to account for the additional double layer contribution. The parameters determining the steric repulsion are (a) representing the heat of fusion, the ordering

parameter (η) and the correlation distance (ξ) (equation 9). Since the correlation distance is found in the exponent, the function is very sensitive to this value. Reasonable values for it are between 0.1-0.3nm, which represent the inter-atomic distance for a majority of phases.

Figure 62 presents a set of graphs of the force balance for three different values of Hamaker coefficient (60, 40, and 20zJ). The calculations were performed for a range expected for alumina grain boundaries and metal-alumina interfaces. The graph is represented in terms of separation distance between the surfaces divided by correlation distance. Figure 62 (a-c and e-g) show the balance for two values of the order parameter (0.5 - 1) and three different correlation distances (0.1, 0.2, 0.3nm). As might be expected, a reduction in the correlation distance results in thinner films, and for ξ= 0.1 and η= 0.5 the film becomes unstable. On the other hand, increasing the order parameter increases the film thickness. A similar effect is obtained if a higher heat of fusion is introduced, since both contribute to the coefficient of the expression. It can be seen from Figure 62 d and h that under certain conditions (ξ= 0.3 and η= 1) the film can withstand a considerable external force of 50MPa. These external forces will of course reduce the film thickness but the films are still stable. In calculations presented in Figure 62 d and h, the heat of fusion was increased to 1 GPa (from 0.4GPa used for SiO_2) to account for values found in the literature for a phase including Al and Ca (Table 18).

Although the ordering parameter here is treated as a constant, it actually will change in response to the forces applied on the interface, probably increasing its value. This was accounted for in the calculation by using a value of 1, for a completely ordered film.

The question now addressed is how will the different film compositions be accounted for by these various parameters?

Choi *et al.* [97] approached the calculation of the van der Waals and steric force in a quantitative manner, evaluating the refractive index, dielectric constant, and heat of melting using a rule of mixtures and the relative strength of the bonds formed by different additives in relation to SiO_2. The values they obtained for the parameters

needed to calculate the Hamaker coefficient for film compositions including Al and Ca seem reasonable, although their refractive index is probably slightly large. However, their estimation of the heat of melting is extremely low. Based on a literature search for the heat of fusion of different silicates and oxides (see Table 18), it is clear that SiO_2 has a very low value, in contradiction with Choi *et al.*. The small value for SiO_2 may be due to the small variation in the bond angles between the crystalline and amorphous state. The different silicate phases have values that are more than three times that of SiO_2 (Table 18). On the other hand, Choi *et al.* took the values for the correlation distance and the order parameter as 0.3nm and 0.5 following Clarke's *et al.* [15] study. It would seem they over looked the important factor that the elements they introduced in the film may change the correlation distance, to which the force balance is very sensitive.

Table 18. Heat of fusion for different Al_2O_3-CaO-SiO_2 based phases.

Phase	Heat of fusion [kJ/mole]	Heat of fusion [MJ/m3]	References
$CaAl_2Si_2O_8$	133±4	1305	[108]
$CaSiO_3$	57.3±3	1346	[108]
$Ca_2Al_2SiO_7$	172.9	1879	[109]
SiO_2	9.58±0.2	372	[15]
Al_2O_3	111.1	4348	[110]

It is clear from these calculations that a force balance can be reached that will stabilize the films to thickness values observed in the present study. However, the difficulty is to determine the correct parameters to use for the film, and possible effects resulting from its confinement.

A question that should be considered is how accurate is the term suggested by Clarke for the steric repulsion? As was shown, if phases other than SiO_2 are assumed to form the film, this should result in a higher repulsion force due to the increase in the heat of melting. On the other hand, it is known that some of these additions result in (from bulk glasses) [72] non-bridging oxygen atoms and break up the glass network, thereby reducing the viscosity of the melt. Intuitively we would expect that this would result in reduction of the steric forces, but it is not clear how this is accounted for in the steric term.

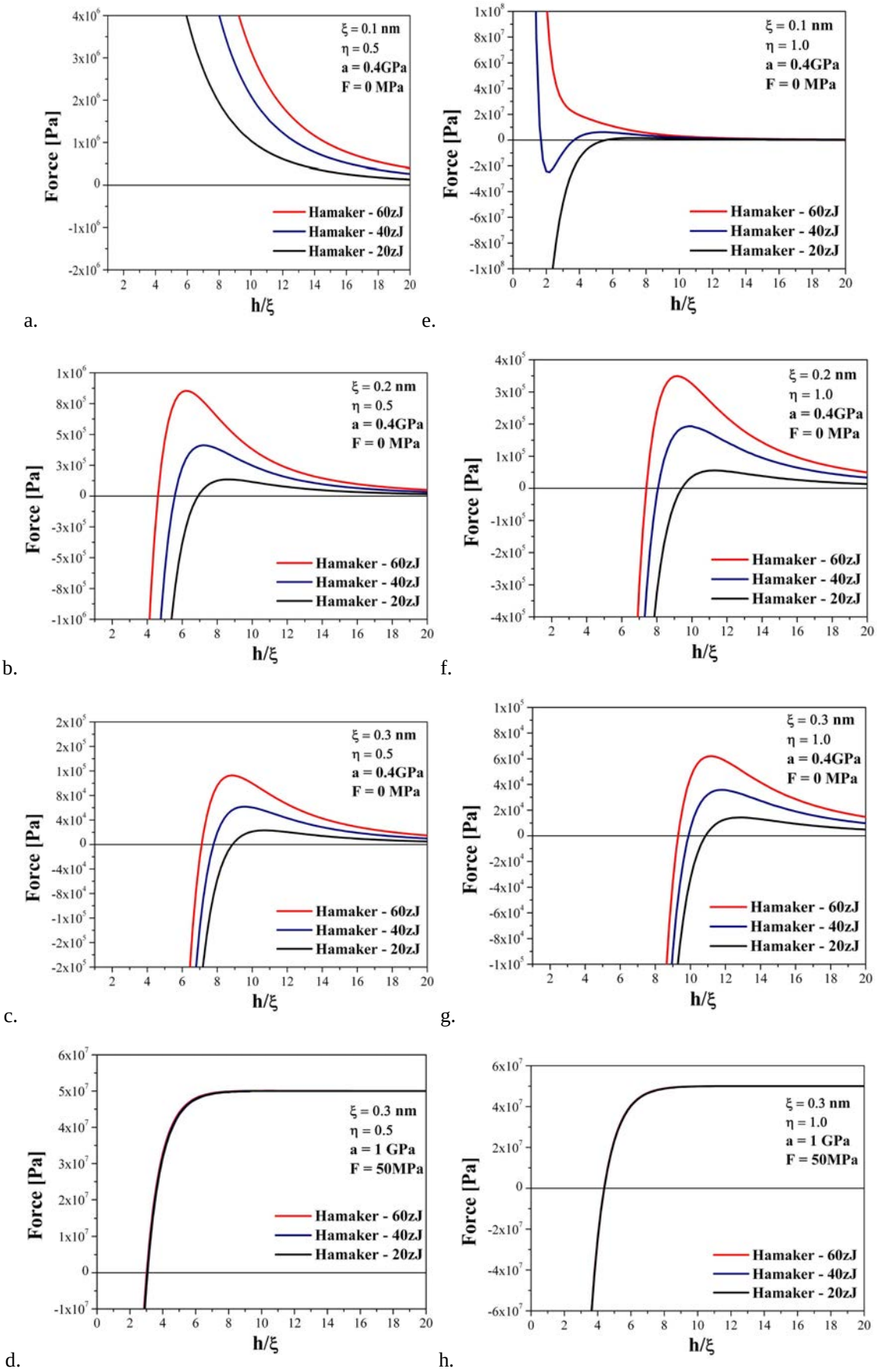

Figure 62. Calculations of the interfacial force balance for different configurations of attractive and repulsive forces.

To resolve some of these questions more accurate experimental data is needed from the films, and as well as a method to evaluate the capillary forces during the final stages of sintering. Here grain boundary grooving experiments of samples with glass additives may contribute some information, if the sample can be cooled fast enough to assure as little as possible change in geometry.

4.2.3. Surface Equilibrium films

An interesting point that is still left unclear from the results and theoretical analysis is the question of possibly surface films on alumina. The XPS and Auger measurements indicated the presence of Si and Ca on the alumina surface, in areas that were not covered by the drop. At this stage, it cannot be experimentally determined unequivocally whether these are surface films or an adsorption layer, but the relative composition of Ca and Si measured in these areas compared to the glass drop suggest it may be a surface film. Alternatively, these may be droplets of glass left after destabilizing of a surface film at a high temperature, as was reported by Carter's group [94,95]. It is clear that the Ca and Si were able to diffuse fast enough, and in a large enough amount to result in formation of relatively large particles in the wetting experiment with a Ni drop, located 5mm from the glass source.

This is important, since if the glass has a lower refractive index than alumina (as is assumed for the grain boundary case) it cannot exist as an equilibrium film at the free surface based on the force balance model (without introducing additional factors such as chemical bonding), since this would result in a negative Hamaker coefficient.

If indeed these are surface films, we return to one of the questions raised at the beginning, if the films found in Scheu's [23] study were in fact remains of a surface film. Based on the results presented in the present study, even if originally there was such a surface film it would probably be altered at the working temperature used to perform the infiltration. The dewetting experiments of Cu on sapphire at temperatures as low as 1000°C resulted in dissolution of the sapphire substrate. Therefore, it would be safe to assume that such a surface film would probably be subjected to dissolution after 30min at 1350°C.

4.3. Microstructure Evolution in Metal-Alumina Composites

In many commercial alumina products liquid phase sintering is used to enhance the sintering process, allowing sintering at lower temperatures and shorter times [14, 111]. Common glass forming additives in alumina are SiO_2 and CaO. Liquid phase sintering is usually accompanied by abnormal and/or elongated grain growth, residual porosity in the form of occluded pores, and glass films at the grain boundaries [14,16,18,95]. These effects can significantly affect the mechanical properties.

The influence of glass in alumina has been studied extensively with respect to grain growth and microstructure morphology [95,112-115], measurements of segregation at grain boundaries and triple junctions [14,16,18,116-120], formation of intergranular films [14,15], mechanical properties [121], and simulations of the glass structure at the interface have been performed [21,22]. Model experiments were performed using sapphire to study the wetting behavior of glass [122,123] and the surface (or interface) morphology in the presence of glass [124,125].

Adding MgO to alumina reduces grain growth rates and suppresses the occlusion of pores [114,115]. MgO has a beneficial effect on sintering, and leads to an equi-axed morphology of the alumina grains [114], This is probably due to reduction of the anisotropy of the grain boundary energy [114,125] and a higher solubility of the glass forming elements in the bulk alumina [117].

In recent years, many studies have been reported on alumina-based composites, where the alumina matrix is reinforced by a second phase [35,126-129]. Of particular interest are the alumina based nanocomposites, where the alumina is reinforced by sub-micron sized particles of a second phase [130-135]. Composites based on alumina reinforced with Cu, Al, Mg, Ni, W and other metals have been studied, using various techniques to introduce the metal [6,131,134,136-138]. The two main morphologies obtained are: an interpenetrating metallic network within a porous alumina body [138,139] or a uniform dispersion of particles within the ceramic matrix [6,131,132,137,140]. In some of the studies, the partial pressure of oxygen was controlled to assist liquid penetration of the metals into the alumina preform [138], or to reduce metal oxides after processing [130,131].

4.3.1. Microstructure of the Metal-Al_2O_3 Composites

The reinforcement of an alumina matrix with metal may influence the mechanical properties of the composite through a number of possible mechanisms: pinning of the alumina grains during sintering, or solution drag as result of segregation at the alumina grain boundaries [45], thereby reducing the average alumina grain size and increasing the fracture strength. The metal can increase fracture toughness by a bridging effect and/or crack deflection [141]. Oh *et al.* showed that Cu particles refined the alumina grain size by grain boundary pinning [130,131]. Adding Ni to the alumina samples is more effective in retarding alumina grain growth by pinning, due to its higher melting temperature.

Glass Doped Composites

In the present study the alumina grain size in the alumina sample without metal reinforcements was not investigated. The average alumina grain size in the Ni reinforced samples was finer than the Cu-alumina samples, however it is not possible to separate the metal's influence from other factors, including: the temperature and pressure during sintering (including the $P(O_2)$). Nevertheless, TEM observations of the doped and undoped metal reinforced samples clearly indicated that doping resulted in a courser microstructure in both composites (Figure 12, and Figure 13). This is due to the higher grain growth rate in the presence of a liquid phase at the grain boundaries [14,114]. The thin equilibrium intergranular film formed at the alumina grain boundaries allows fast diffusion of the material between the adjacent grains. In the present study, the presence of a glass had a detrimental effect, since a large fraction of the metal particles and pores were occluded during sintering. Once the metal particles are occluded, their contribution to mechanical properties is expected to be limited since they contribute primarily during sintering by pining the alumina grain boundaries [131].

The undoped Ni-alumina sample was not investigated systematically by TEM, save for one sample in which some Ni occlusions were observed. However, in the undoped Cu-alumina sample all the Cu particles were found at the alumina grain boundaries. On the other hand, pore occlusion *was* observed. The morphology of the Cu particles was unusual, since it would be expected to be more equi-axed considering that the Cu-alumina system is non-wetting under non-oxidizing conditions [13]. No copper-oxides or copper-aluminates were found by X-ray or TEM analysis (these are known to form elongated particles [82,142]).

The oxygen partial pressure measured during the sintering process was below the detection limit of the measuring system (10^{-9} Torr). According to the literature, at this $P(O_2)$ level the Cu should not oxidize [83,143]. Sessile drop experiments of Cu on alumina/sapphire reported in the literature show that at partial pressures of oxygen in the range of ~10^{-15} – 10^{-7} atm ($8x10^{-13}$ - $8x10^{-5}$ Torr which is below the $P(O_2)$ for Cu oxidation) [12,13] oxygen adsorption occurs, which results in a reduction in the contact angle.

Sessile drop experiments of Cu on sapphire performed in the present study in the same furnace in which the Cu-alumina composites were sintered, and under similar conditions (T, $P(O_2)$) resulted in contact angles of ~114° in the temperature range of 1200-1400°C. At this temperature, for non-oxidizing conditions the contact angle is reported to be ~130° [10,12,13]. These results indicate that under the conditions used for sintering, the Cu-alumina system was probably in the oxygen adsorption range [10,13]. This may explain the elongated Cu morphology and trace amounts of Cu segregation observed at the alumina grain boundaries.

The properties of the composite materials are often dominated by the nature of their interfaces [25]. The presence of impurities in the starting material may lead to the formation of intergranular films or segregation at the interfaces. Examples include crystalline thin films formed at Al-Al_2O_3 interfaces, resulting from non-equilibrium segregation of Ca [92,93], or the formation of intergranular films investigated in this work [23,144].

Very few studies conducted on metal-ceramic composites have addressed the influence of impurities on the microstructure or the mechanical properties, while this issue was addressed for ceramic-ceramic composites [35,127,128] or in basic studies on adhesion at metal-ceramic interfaces [145,146].

The experimental results presented in this study clearly show the stability of intergranular films at metal-alumina interfaces in the glass doped samples. The film's presence modifies the metal-alumina interface chemistry and structure. This in turn is expected to modify the mechanical behavior of the interfaces. The presence of the Ca-Si based intergranular films at the metal-alumina interfaces means the adhesion, even for particles located at triple junctions and alumina grain boundaries, is no longer determined by the metal-alumina interface energy, but rather by the alumina-glass-metal interface. From our present results and results reported by Scheu [23] it seems there is segregation of Ca to the Cu-glass interface, thereby further modifying the properties of the interface. Some qualitative indication of the intergranular film effect may be seen in the fracture behavior of the samples used for the XPS analysis (Figure 45). The sample prepared without glass fractured at the Ni-sapphire interface leaving smooth surfaces. However, the samples prepared together with anorthite glass actually were much harder to fracture, and once fractured the crack propagated through the sapphire substrate. The same behavior occurred with two different samples that were fractured. If these results are indicative of the bonding that may be obtained between the metal and sapphire, this could be used as a joining method for dissimilar materials using very small levels of glass doping. Alternatively, sputter-coating a ~nm thick layer on one of the surfaces, followed by a short bonding treatment, could be a viable method to apply these results.

4.3.2. Occlusion

Two points standout concerning the metal particle occlusion: the fact that glass doping promotes particle occlusion (Figure 63) and the distinct size distribution of the occluded particles relative to particles found at grain boundaries, with an average particle size of 250nm and 1400nm, respectively, in the glass doped Cu-alumina composite (Figure 17). A similar behavior was observed in the glass doped Ni-alumina composite (Figure 34). It seems from the particle size distribution graphs that at the point where the occluded particles frequency declines, the frequency of the metal particles at the grain boundaries begins (this issue is discussed in the following).

In composites prepared by Oh *et al.* using high purity alumina, only a few occluded particles were observed [130,131,140]. However, in a study by Chen & Tuan [132], a large number of Ni particles were reported to be occluded (~20-30%). Based on the findings from the present study, where 70-80% of the particles were found as occluded particles, the question is raised whether the samples prepared by Chen & Tuan contained small amounts of impurities/glass. A similar difference in the distribution of the reinforcing particle size was observed in both studies when comparing the occluded particles and the particles found at grain boundaries and triple junctions [132]. Chen & Tuan reported occluded Ni particles were limited up to ~100nm in size [132]. It is clear this type of behavior is not limited to the composites prepared in the present study.

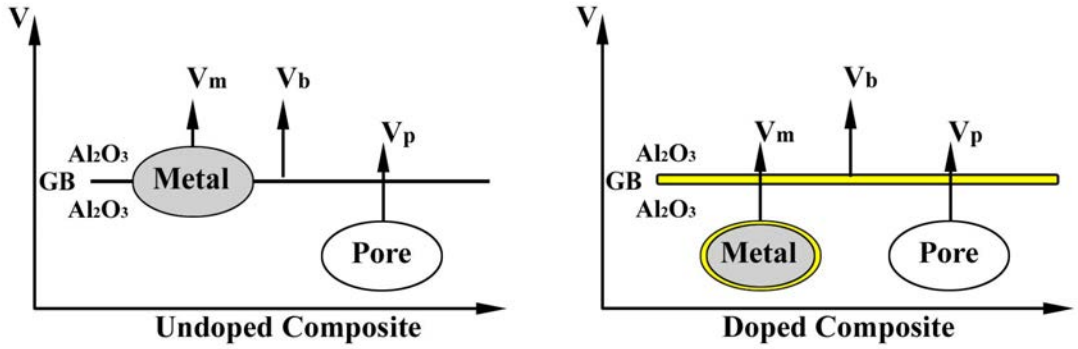

a. b.

Figure 63. Schematic drawing of the grain boundary velocity relative to the pore and metal particle velocity in the a) undoped, and b) glass doped Cu-alumina composites. The yellow color represents the intergranular film. In the undoped sample the pores are occluded while the metal particles are left at the grain boundaries, while in the glass doped sample both pores and metal particles are occluded.

Metal particles or pores at grain boundaries can limit grain growth by pinning the grain boundaries [45]. Assuming the starting condition is a spherical particle at an alumina grain boundary, occlusion by the alumina grain will increase the total grain boundary area. Assuming no special orientation relationships, and thus no low energy interfaces, occlusion will increase the surface energy of the system. Therefore, occlusion occurs due to kinetic reasons rather than a thermodynamic driving force. For the particle (or pore) to stay attached to a grain boundary, its velocity should be the same as the grain boundary [45]. The velocity (V_i) may be described as the product of two parameters; the driving force (F_i) and the mobility (M_i):

$$(27) \qquad V_i = F_i \cdot M_i$$

The driving force for grain growth is the reduction in the total internal surface (grain boundary) energy. The local driving force is the difference in curvature of the grain boundaries, which leads to a gradient in the chemical potential between two boundaries in contact or along the boundaries [47,72]. The driving force for grain growth can be expressed by the grain boundary energy (γ_{GB}) and average grain size ($\bar{G}$) [45]:

$$(28) \qquad F_b \approx \frac{3\gamma_{GB}}{\bar{G}}$$

For a given grain boundary energy, the smaller the grain size the larger the driving force for grain growth. We will first consider the grain boundary mobility of the glass doped metal alumina composites. In the presence of an intergranular film, two possible expressions may describe the grain boundary mobility [45]:

$$(29) \qquad M_{GB-IGF} = \frac{D_l \cdot C_l}{l} \frac{\Omega}{kT}$$

where D_l is the diffusivity of bulk ions in the liquid layer, l is the thickness of the liquid layer, C_l is the solubility, Ω is the total ionic volume divided by the number of slow diffusing ions, k is Boltzmann's constant, and T is the absolute temperature.

$$(30) \qquad M_{GB-IGF} = \frac{\Omega \cdot \kappa'}{kT}$$

where the reaction constant κ' depends on temperature, and can also vary with the kinetic process, orientation, and driving force.

Equation 29 is used for cases where the diffusion across the grain boundary film is the limiting factor, while in Equation 30 the surface reaction rate is the limiting factor. Since in the doped samples the alumina grain boundaries have a thin (~nm thick)

equilibrium film, for both case we may assume to a first approximation that the mobility will not change drastically during the sintering process. This means that the velocity of the grain boundaries will decrease as $1/\bar{G}$ during the sintering.

For the particle/pore the driving force is actually the drag force exerted by the moving grain boundary [45] and its maximum value may be expressed as:

$$(31) \qquad F_p = \pi r \gamma_{GB}$$

where r is the particle radius. This expression is based on a simplistic geometrical model of pore drag and underestimates the drag force exerted on the pore. Hsueh *et al.* [147] developed an expression using a more realistic approach of the pore shape evolution during grain boundary motion, and obtained the following expression which takes into account the dihedral angle ψ (Figure 64) formed between the pore and the leading and trailing surfaces:

$$(32) \qquad F = \pi r \gamma_{GB}(17.9 - 6.2\psi)$$

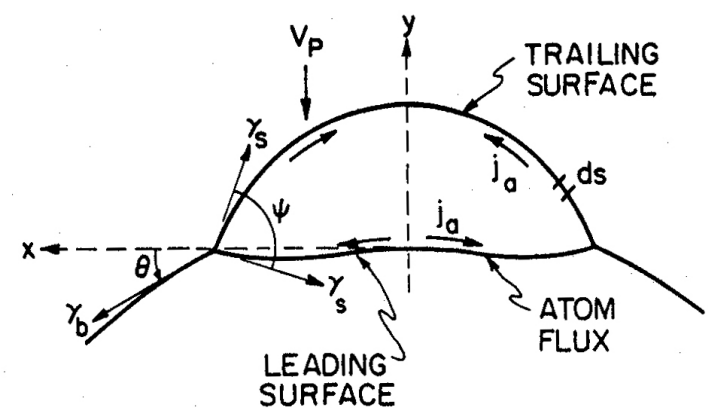

Figure 64. A schematic drawing of a moving pore attached to the grain boundary. The atom flux and the inclination of the grain boundary, θ as indicated in the figure [147].

The mobility of a particle/pore can be expressed in a similar way if the particle is assumed to have a dominate interfacial diffusion [45,148]:

$$(33) \qquad M_p = \frac{D_s \delta_s \Omega}{kT \pi r^4} \quad , \quad M_{m-I} = \frac{D_I \delta_I \Omega}{kT \pi r^4}$$

where δ is the boundary core width. For metal-ceramic interfaces, diffusion tends to be faster than for ceramic surfaces [12]. However, in some cases volume diffusion

dominates over interfacial diffusion as was shown by Saiz *et al.* [12] and Monchoux *et al.* [149]. In this case mobility is a function of $1/r^3$ [12,148,149]:

$$(34) \qquad M_{m-V} = \frac{3D_v c_m \Omega}{4\pi kTr^3}$$

where c_m is the solubility of the diffusing atoms in the particle. It can be seen that whichever diffusion mechanism is dominate, the velocity of small particles is expected to be *higher* than larger ones, since the velocity will depend on $1/r^3$ for surface/interface diffusion while for volume diffusion it will depend on $1/r^2$. This means the observed particle size distribution of small particles occluded while larger particles are found at the interface could not be controlled by particle velocity dependence on particle size.

Both the alumina grains and metal particles coarsen during sintering. In the initial stage of sintering, due to the presence of a thin liquid film at the grain boundaries, the mobility of the boundaries is increased, and at the same time the driving force is high since the alumina starts from a fine 0.3μm size powder. This results in a high velocity of the grain boundaries at this stage, and relatively small occluded particle size.

As the sintering process advances the metal particles coarsen, which reduces their velocity and should result in their occlusion. However, the simultaneous coarsening of the alumina grains reduces the driving force for grain growth and therefore the grain boundary velocity. This enables the metal particles to advance together with the moving alumina boundaries and results in the observed particle size distribution. This model could tested by sintering a set of glass doped metal-alumina composites with different starting powder size.

We are still left with the question of why in the undoped Cu-alumina samples the particles are not occluded, while pore occlusion is observed. In the absence of a liquid film at the interface, two models describe the mobility. In the first, the intrinsic mobility for segregation-free grain boundaries is [45]:

$$(35) \qquad M_0 = \frac{f\, D_{GB}\Omega}{\delta kT}$$

where f is the site factor reflecting the density of boundary core sites associated with high jump probabilities, and D_{GB} is the boundary self diffusion coefficient for the slower ion for transport normal to the boundary plane. This is rarely the case, since as was

observed in the present study it is very hard to maintain a perfectly pure material. Impurity concentration even in the tens of ppm level (if not soluble in the matrix) will be segregated to the grain boundaries and affect the mobility behavior [45,46]. In this case it is more convenient to describe the effect in terms of drag force acting on the boundary [45,46]:

$$F_d = F_d = \frac{V_{GB}}{M_0} + \frac{\alpha_s C_\infty V_{GB}}{\left[1+\left(\beta_d V_{GB}\right)^2\right]} \quad (36)$$

where α_s is the solute drag force per unit velocity and per unit solute concentration in the low-velocity limit, C_∞ is the bulk solute concentration, and β_d^{-1} is approximately the drift velocity with which a solute diffuses across the near grain boundary region (defines the velocity at which the boundary breaks away from the solute cloud).

It turns out that for the undoped sample two important differences exist. First, the mobility of the grain boundaries is lower due to the lack of the intergranular film and the presence of grain boundary segregation, thereby reducing the grain boundary velocity.

From the point of view of the particles, their elongated morphology is expected to increase the drag force exerted on them due to the small dihedral angle, at the same time the higher grain boundary energy in the absence of an intergranular film should as well increase the drag force. Both effects result in a higher particle velocity, allowing the particles to advance together with the grain boundaries. However, the pores are occluded, and this may be due to their lower mobility (surface diffusion relative to interface or possibly volume diffusion in the particle case) [12,149].

This may shed some light on the mechanism of Mg additions which are known to suppress pore occlusion during sintering. Very small amounts of Mg (0.03 wt%) are usually needed, but in most studies the presence of Mg is not detected at the end of the sintering process [150,151]. It is possible that the Mg is essential at the initial stages of the sintering process, when the driving force for grain growth is high. However, once the structure coarsens, the gradual loss of Mg by evaporation (as a result of a high vapor pressure) does not lead to pore occlusion, since at the same time the grain boundary driving force is reduced.

5. SUMMARY AND CONCLUSIONS

The main objective of the present research was to establish the stability of equilibrium intergranular films at *metal-ceramic* interfaces. This was performed by investigation of *metal*-Al_2O_3 nanocomposites specifically designed for that purpose.

Ni and Cu alumina nanocomposites were prepared with predetermined amounts of Ca and Si dopants resulting in Si and Ca rich glass pockets and thin intergranular films. The films were observed at alumina-metal interfaces, at alumina grain boundaries, and at two-phase triple junctions, as well as interfaces between alumina and occluded metal particles. On the other hand, no amorphous phase was observed in the undoped composites.

A difference in the thickness of the intergranular films was measured for the two metal-alumina composites for the same terminating plane of alumina. Some evidence for ordering was observed in the films found at some of the Ni-alumina interfaces. EDS chemical analysis of the films between the Ni-alumina and Cu-alumina interfaces yielded a difference in the chemical composition. At this stage it is unclear whether the difference in the chemistry and structure of the intergranular films in the two composites results from differences in the sintering regime or the type of metal.

In addition Cu/Ni-sapphire wetting and dewetting experiments were performed with and without the presence of anorthite glass. The wetting experiments of Ni on sapphire performed in the presence of a glass drop resulted in glass elements penetrating the Ni-sapphire interface. This caused a considerable reduction of the contact angle and the interfacial energy. Although no direct observation was found for the formation of an intergranular film in these samples, indirect evidence pointed to the presence of such films. In addition, samples fractured for XPS analysis showed that fracture advanced through the sapphire in contrast to the samples without glass, where the crack advanced along the Ni-sapphire interface. XPS analysis of the sapphire surfaces after glass wetting indicated the possibility of surface film formation, which has important implications in regard to intergranular films, since if the glass has a lower refractive index than alumina it cannot exist as an equilibrium film at the free surface.

Calculations of Hamaker coefficients were performed for the alumina grain boundaries and metal-ceramic interfaces which indicated that a stronger attractive force is expected for intergranular films at *metal-alumina* interfaces, even across a relatively wide range of refractive index values for the film. These results correlate to the film thickness measured in this work. At this stage, it is not possible to calculate accurately the repulsive terms since the absolute composition and distribution of the elements in the film are not known. Moreover, it is likely that there is Ca segregation to the alumina-film interface, similar to that found by EDS line-scans across the glass pockets and predicted by MD simulations, together with Al segregation to the metal-film interface. In addition, the film thickness measurements were performed at room temperature, and do not necessarily represent the actual film thickness at the sintering temperature.

From the present study, it is evident that intergranular films at metal-alumina interfaces are stable. The wetting experiments strengthen this conclusion. It seems the metal plays an active role in determining the film's behavior both through the forces exerted on the film and the film chemistry. Using a colloid-like force balance model developed for ceramic systems and performing the calculations for a *metal-ceramic* interface in the presence of an intergranular film, it was shown that a similar force balance may be obtained for the metal-ceramic interfaces. Moreover, the attractive force for the *metal-film-ceramic* interface is expected to be higher than for the ceramic grain boundary.

The results of this research project have technological and scientific consequences to joining of metals to ceramics, and for metal-ceramic composites.

It was observed in the composite materials that glass doping results in significant changes to the nanocomposite microstructure and properties. In the presence of grain boundary and interface equilibrium films, grain boundary mobility dominates, leading to pore and particle occlusion. The uniform size of the occluded Cu particles suggests that the occlusion mechanism is limited to a maximum particle size associated with a higher driving force at the initial stages of sintering. In the absence of grain boundary equilibrium films, the lower pore mobility, relative to particle mobility, results only in pore occlusion. The $P(O_2)$, in the adsorption range of oxygen to the Cu surfaces and interfaces, resulted in elongated morphology of the Cu particles in the undoped sample.

6. RECOMMENDATIONS FOR FUTURE WORK

At the end of the day, there are more questions than answers. A number of experimental results are lacking in order to better correlate between the results and the theoretical calculations. These primarily concern the properties of the intergranular film: its absolute composition, distribution of the elements within it, and the nature of the chemical bonding. In principle, the radial distribution function and dielectric properties of the film may be obtained from EELS measurements. However, these measurements are not experimentally trivial to conduct. Such information could provide additional parameters needed for the calculation of the forces.

The method used by French to directly measure the data needed to calculate the Hamaker coefficient is now in progress. Once this is completed, it will provide valuable support to the calculated results.

The issue of alumina surface films has barely been touched, yet may have some important implications both on the model and the properties of a confined film. Such a film may be investigated using alternative methods and compared to the interfacial film.

Wetting was addressed in the present work mainly to support the results in the composite materials. However, this is an important topic in itself. As seen from the limited work so far, the films at metal-ceramic interfaces may have important implications for the joining of the two dissimilar materials. These issues are currently under investigation.

It was shown that the films have an important implication in the microstructural evolution of the composite materials, although the grain boundary films played the dominant role. It would be relatively simple to try to verify whether the suggested model explaining the occlusion mechanism is correct. Powders having different ranges of particle size could be used to prepare glass-doped metal-alumina composites, and the resulting influence on the occlusion checked by microstructural characterization.

And there are many more possibilities……

1. S. Chevalier, G. Bonnet, J. P. Larpin and J. C. Colson, “The combined Effect of Refractory Coatings Containing Reactive Elements on High Temperature Oxidation Behavior of Chromia-Forming Alloys”, *Corrosion Science*, 45[8], 1661-1673 (2003).

2. D. Treheux, P. Lourdin, B. Mbongo, D. Juve, “Metal-Ceramic Solid State Bonding: Mechanisms and Mechanics”, *Scripta Metallurgica et Materialia*, 31[8] 1055-1060 (1994).

3. G. Elssner, W. Diem, and J. Wallace, “Microstructure and Mechanical Properties of Metal-to-Ceramic and Ceramic-to-Ceramic Joints”, in Materials Science Research vol, 14, Surfaces and Interfaces in Ceramic and Ceramic-Metal Systems, Edited by J. Pask and A. Evans, Plenum Press, 629-639 (1981).

4. “Interfacial Science in Ceramic Joining”, edited by A. Bellosi, T. Kosmač, and A. P. Tomsia, Kluwer Academic Publishers, 1998. Proceeding of the NATO Advanced Research Workshop on Interfacial Science in Ceramic Joining, Bled Slovenia Nov. 12-15 (1997).

5. B. J. Dalgleish, A. P. Tomsia, K. Nakashima, M. R. Lcatelli, and A. M. Glaeser, “Low Temperature Routes to Joining Ceramics for High-Temperature Applications”, *Scripta Metall. Mater.* 31[8], 1043-1048 (1994).

6. M. Lieberthal and W. D. Kaplan, “Processing and Properties of Al_2O_3 Nanocomposites Reinforced With Sub-Micron Ni and $NiAl_2O_4$”, *Mater. Sci. Eng. A*, 302, 83-91 (2001).

7. Y. Ji and J. A. Yeomans, “Processing and Mechanical Properties of Al_2O_3-5% vol.% Cr Nanocomposites”, *J. Eur. Ceram. Soc.*, 22, 1927-1936 (2002).

8. Claude R. Henry, "Surface Studies of Supported Model Catalysts", *Surface Science Reports*, 31, 235-325 (1998).

9. C. Scheu, G. Dehm, M. Ruhle, R. Brydson, "Electron-Energy-Loss Spectroscopy Studies of Cu-α-Al_2O_3 Interfaces Grown by Molecular Beam Epitaxy", *Philosophical Magazine A*, 78[2] 439-465 (1998).

10. N. Eustathopoulos, M. G. Nicholas, and B. Drevet, "Wettability at High Temperatures", R. W. Cahn Ed. (Pergamon Materials Series Vol. 3) (1999).

11. E. Saiz, A. P. Tomsia, R. M. Cannon, "Ridging Effects on Wetting and Spreading of Liquids on Solids”, *Acta Metallurgica*, 46[7], 2349-2361 (1998).

12. E. Saiz, R. M. Cannon, and A. P Tomsia, "Energetics and Atomic Transport at Liquid Metal/Al_2O_3 Interfaces", *Acta Mater.*, 47[15] 4209-4220 (1999).

13. V. Ghetta, J. Fouletier, and D. Chatain, "Oxygen Adsorption Isotherms at the Surfaces of Liquid Cu and Au-Cu Alloys and their Interfaces with Al_2O_3 Detected by Wetting Experiments", *Acta Mater.*, 44[5] 1927-1936 (1996).

14. R. Brydson, S. C. Chen, F. L. Riley, S. J. Milne, X. Pan, and M. Rühle, "Microstructure and Chemistry of Intergranular Glassy Films in Liquid-Phase-Sintered Alumina", *J. Am. Ceram. Soc.*, 81[2] 369-379 (1998).

15. D. R. Clarke, " On the Equilibrium Thickness of Intergranular Glass Phases in Ceramic Materials", *J. Am. Ceram. Soc.*, 70 [1], 15-22, (1987).

16. C. A. Powell-Dogan, A. H. Heuer, "Microstructure of 96% Alumina Ceramics: I, Characterization of the As-Sintered Materials", *J. Am. Ceram. Soc.*, 73[12], 3670–3676 (1990).

17. C. A. Powell-Dogan, A. H. Heuer, "Microstructure of 96% Alumina Ceramics: III, Characterization of High-Calcia Boundary Glasses", *J. Am. Ceram. Soc.*, 73[12], 3684–3691 (1990).

18. W. Swiatnicki, S. Lartigue-Korinek, A. Dubon and J. Y. Laval, “Intergranular Segregation and Grain Boundary Crystallography in Al_2O_3”, *Materials Science Forum*, 126-128, 193-196 (1993).

19. http://www.lrsm.upenn.edu/~frenchrh/eu-nsf_nanoam.htm

20. R. M. Cannon, M. Rühle, M. J. Hoffmann, R. H. French, H Gu, A. P. Tomsia, and E. Saiz. “Adsorption and Wetting Mechanisms at Ceramic Grain Boundaries”, in Grain Boundary

41. V. J. Keast and D. B. Williams, "Quantification of Boundary Segregation in the Analytical Electron Microscope", *J. of Microscopy*, 199, 45-55 (2000).

42. V. J. Keast and D. B. Williams, "Grain Boundary Chemistry", *Current Opinion in Solid State and Mater. Sci.*, 5, 23-30 (2001).

43. D. R. Clarke, "Grain Boundaries in Polycrystalline Ceramics", *Ann. Rev. Mater. Sci*, 17, 57-74, (1987).

44. R. Raj and F. F. Lange, "Crystallization of Small Quantities of Glass (or a Liquid) Segregated in Grain Boundaries", *Acta Metallurgica*, 29, 1993-2000 (1981).

45. J. D. Powers and A. M. Glaeser, "Grain Boundary Migration in Ceramics", *Interface Sci.*, 6, 23-39 (1998).

46. M. F. Yan, R. M. Cannon, and H. K. Bowen, "Grain Boundary Migration in Ceramics" in *Ceramic Microstructures*, ed R. M. Fulrath and J. A. Pask, West-View Press, Boulder, CO, pp.276 (1976).

47. Y. M. Chaing, D. Birnie III, W. D. Kingery, "Physical Ceramics – Principles for Ceramic Science and Engineering", Wiley, MIT series in Materials Science & Engineering, (1997).

48. M. Hillert, "Inhibition of Grai Growth by Second-Phase Particles", *Acta Metall*. 36[12], 3177-3181, (1988).

49. E. Rabkin, "Zener Drag in the Case of Anisotropic Grain Boundary Energy", *Scripta Mater.*, 39[12] 1631-1637, (1998).

50. I. Tanaka, H.-J. Kleebe, M. K. Cinibulk, J. Bruley, D. R. Clarke, and M. Rühle, "Calcium Concentration Dependence of the Intergranular Film Thickness in Silicon Nitride," *J. Am. Ceram. Soc*., 77[4] 911–914 (1994).

51. Q. Jin, D. S. Wilkinson, G. C. Weatherly, W. E. Luecke, and S. M. Wiederhorn, "Thickness Alteration of Grain-Boundary Amorphous Films During Creep of a Multiphase Silicon Nitride Ceramic", *J. Am. Ceram. Soc*., 84[6], 1296-1300 (2001).

52. J. –R. Lee, Y. M. Chiang, and G. Ceder, "Pressure-Thermodynamic Study of Grain Boundaries: Bi: Segregation in ZnO", *Acta Mater*., 45[3], 1247-1257 (1997).

53. Y. M. Chiang, L. A. Silverman, R. H. French, and R. M. Cannon, "Thin Glass Films Between Ultrafine Conductor Particles in Thick-Film Resistors", *J. Am. Ceram. Soc*., 77[5], 1143-1152 (1994).

54. K. M. Knowles and S. Turan, "The Dependence of Equilibrium Film Thickness on the Grain Orientation at Interphase Boundaries in Ceramic-Ceramic Composites" *Ultramicroscopy*, 83, 245-259 (2000).

55. R. Brydson, P. C. Twigg, F. Loughran, and F. L. Riley, " Influence of the CaO-SiO_2 ratio on the Chemistry of Intergranular Films in Liquid-Phase Sintered Alumina and Implications for Rate of Erosive Wear", *J. Mater. Res*., 16[3], 652-665 (2001).

56. D. R. Clarke, T. M. Shaw, A. P. Philipse, and R. G. Horn, "Possible Electrical Double-Layer Contribution to the Equilibrium Thickness of Intergranular Glass Films in Polycrystalline Ceramics", *J. Am. Ceram. Soc*., 76[5], 1201-1204 (1993).

57. M. Yoshiya, K. Tatsumi, I. Tanaka, and H. Adachi, "Theoretical Study on the Chemistry of Intergranular Glassy Film in Si_3N_4-SiO_2 Ceramics", ", *J. Am. Ceram. Soc*., 85[1], 109-112 (2002).

58. M. Brada and D. R. Clarke, "A Thermodynamic Approach to the Wetting and Dewetting of Grain Boundaries", *Acta Mater*., 45[6], 2501-2508 (1997).

59. P. Keblinski, S. R. Phillpot, D. Wolf, and H. Gleiter, "On the Thermodynamic Stability of Amorphous Intergranular Films in Covalent Materials", ", *J. Am. Ceram. Soc*., 80[3], 717-732 (1997).

60. H. Wang and Y. M. Chiang, "Thermodynamic Stability of Intergranular Amorphous Films in Bismuth-Doped Zinc Oxide",", *J. Am. Ceram. Soc*., 81[1], 89-96 (1998).

61. R. H. French, "Origins and Applications of London Dispersion Forces and Hamaker Constants in Ceramics", *J. Am. Ceram. Soc*., 83[9], 2117-2146 (2000).

62. I. E. Dzyaloshinskii, E. M. Lifshitz, and L. P. Pitaevskii, "The General Theory of Van Der Waals Forces", *Adv. Phys.*, 10, 165-209, (1961).

63. J. Israelachvili, "Intermolecular & Surface Forces", Academic Press, NY, ed 2, 1992.

64. L. Bergström, " Hamaker Constants of Inorganic Materials", *Adv. Colloid.Int. Sci.* 70, 125-169 (1997).

65. L. Bergström, A. Meurk, H. Arwin, and D. Rowcliffe, " Estimation of Hamaker Constants for Ceramic Materials from Optical Data Using Lifshitz Theory", *J. Am. Ceram. Soc.*, 79[2], 339-348 (1996).

66. D. B. Hough and L. R. White, "The Calculation of Hamaker Constants from Lifshitz Theory with Applications to Wetting Phenmena", *Adv. in Colloid and Interface Sci.*, 14, 3-41 (1980).

67. D. R. Clarke and M. L. Gee, "Wetting of Surfaces and Grain Boundaries", in *Materials Interfaces* ed D. Wolf and S.Yip Chapman & Hall, London, 255-272(1992).

68. W. J. Huisman, J. F. Peters, M. J Zwanenburg, S. A. de Vries, T. E. Derry, D. Aberanathy, J. F. van der Veen, "Layering of a Liquid Metal in Contact with a Hard Wall", *Nature*, 390, 379 (1997).

69. S. E. Donnelly, R. C. Birtcher, C. W. Allen, L. Morrison, K. Furuya, M. Song, K. Mitsuishui, and U. Dahmen," Ordering in a Fluid Inert Gas Confined by Flat Surfaces", *Science*, 296, 507-510 (2002).

70. W. D. Kingery, H. K. Bowen, and D. R. Uhlmann, "Introduction to Ceramics", John Wiley & Sins, NY, Second Edition, (1991).

71. R. A. Terpstra, P. P. A. C. Pex, and A. H. de Vries, "Ceramic Processing", Chapman & Hall, London, (1995).

72. M. Barsoum, “Fundamentals of Ceramics”, McGraw-Hill, Series in Materials Science and Engineering, (1997).

73. H. Müllejans and R. H. French, " Insights into the Electronic Structure of Ceramics through Quantitative Analysis of Valence Electron Energy-loss Spectroscopy", *Microscopy & Microanalysis*, 6, 297-306 (2000).

74. R. H. French, H. Müllejans and D. J. Jones, "Optical Properties of Aluminum Oxide: Determined from Vacuum Ultraviolet and Electron Energy-Loss Spectroscopies", *J. Am. Ceram. Soc.*, 81[10] 2549-2557 (1998).

75. H. Gu, X. Pan, R. M. Cannon, and M. Rühle, " Dopant Distribution in Grain-Boundary Films in Calcia-Doped Silicon Nitride Ceramics", *J. Am. Ceram. Soc.*, 81[12], 3125-3135 (1998).

76. H. –J. Kleebe and G. Pezzotti, "Grain Boundary Wetting-Dewetting in z=1 SiAlON Ceramic", *J. Am. Ceram. Soc.*, 85[12], 3049-3053 (2002).

77. H. D. Ackler and Y. M. Chiang, "Model Experiment on Thermodynamic Stability of Retained Intergranular Amorphous Films", *J. Am. Ceram. Soc.*, [80[7], 1893-1896 (1997).

78. H. D. Ackler and Y. M. Chiang, "Effect of Initial Microstructure on the Final Intergranular Phase Distribution in Liquid-Phase-Sintered Ceramics", *J. Am. Ceram. Soc.*, 82[1], 183-189 (1999).

79. D. R. Clarke, “Wetting of Grain Boundaries in Metals and Ceramics”, *Mater. Sci. Forum.*, 294[2], 2-8 (1999).

80. E. Rabkin, " Thin Films on Grain Boundaries in Metals and Ceramics and their Importance for the Properties of the Materials", in Materials Science Monographs Vol. 81, Science of Ceramic Interfaces, ed. J. Nowotny, Elsevier, Oxford, 371-398 (1994).

81. M. Knechtel, H. Prielipp, H. Müllejans, N. Claussen, and J. Rödel, “Mechanical Properties of Al/Al_2O_3 and Cu/ Al_2O_3 Composites with Interpenetrating Networks,” *Scr. Metall. Mater.*, 31[8], 1085–1090 (1994).

82. Kirk A. Rogers, Kevin P. Trumble, Brian J. Dalgleish, Ivar E. Reimanis, "Role of Oxygen in Microstructure Development at Solid-State Diffusion-Bonded $Cu/\alpha\text{-}Al_2O_3$ Interfaces", *J. Am. Ceram. Soc.*, 77[8], 2036-2042 (1994).

83. M. Diemer, A. Neubrand, K. P. Trumble, and J. Rodel, "Influence of Oxygen Partial Pressure and Oxygen Content on the Wettability in the Copper-Oxygen-Alumina System", *J. Am. Ceram. Soc.*, 82[10] 2825-2832 (1999).

84. Metal Reference Book, ed C. J. Smithells and E. A. Brandes, 5th edition, 940-946 (1978).

85. "CRC materials science and engineering handbook", ed. J. F. Shackelford and W. Alexander,. CRC Press, London, 3rd ed. (2001).

86. K. P. Trumble and M. Rühle, "The Thermodynamics of Spinel Interphase Formation at Diffusion Bonded Ni/Al_2O_3 Interfaces", *Acta Metallurgica et Materialia*, 39[8], 1915-1924 (1991).

87. R. Brydson, H. Müllejans, J. Bruley, P. A. Trusty, X. Sun, J. A. Yeomans and M. Rühle, "Spacially Resolved Electron Energy-Loss Studies of Metal-Ceramic Interfaces in Transition Metal/Alumina Cermets", *J. of Microscopy*, 177[3], 369-386 (1995).

88. W. Swiatnicki, S. Lartigue-Korinek, and J. Y. Laval, "Grain Boundary Structure and Intergranular Segregation in Al_2O_3", *Acta. Metall. Mater.*, 43[2], 795-805 (1995).

89. G. Levi, "Energy and Structure of Nickel-Alumina Interfaces", Ph.D. thesis, Technion-Israel Institute of Technology, (2002).

90. P. L. Flaitz and J. A. Pask, "Penetration of Polycrystalline Alumina by Glass at High Temperatures", *J. Am. Ceram. Soc.*, 70[7], 449-455 (1987).

91. K. Kaneko and N. Kondo, "TEM Studies of Reaction-Bonded $Si3N_4$/SiC Composites", in Grain Boundary Engineering in Ceramics edited by Taketo Sakuma, Laurel M. Sheppard, and Yuichi Ikuhara, Publihed by the American Ceramic Society, 391-397, (2000)

92. W. D. Kaplan, "The Influence of Ca on Interface Structure and Chemistry in Melt-Infiltrated α-Al_2O_3/Al Composites," *Acta Mater*., 46[7], 2369–2379 (1998).

93. W. D. Kaplan, H. Müllejans, M. Rühle, J. Rödel, and N. Claussen, "Ca Segregation to Basal Surfaces in α-Alumina," *J. Am. Ceram. Soc*., 78[10], 2841–2844 (1995).

94. N. Ravishankar and C. B. Carter, "Exuding Liquid from Grain Boundaries in Alumina", *J. Am. Ceram. Soc.*, 84[4], 859-862 (2001).

95. N. Ravishankar and C. B. Carter, "Migration of Alumina Grain Boundaries Containing a Thin Glass Film", *Acta. Mater.*, 49, 1963-1969 (2001).

96. M. A. Gülgün, R. Voytovych, I. Maclaren, M. Rühle, and R. M. Cannon, "Cation Segregation in an Oxide Ceramic with Low Solubility: Yttrium Doped α –Alumina", *Interface Sci.*, 10, 99-110 (2002).

97. H. J. Choi, G. H. Kim, J. G. Lee and Y. W. Kim, "Refined Continuum Model on the Behavior of Intergranular Films in Nitride Ceramics", *J. Am. Ceram. Soc.*, 83[11], 2821-2827 (2000).

98. A. Parsegian, "Van der Waals Forces", Cambridge Univ. Press, in press (2003).

99. J. Mahanty and B. W. Ninham, "Dispersion Forces", Academic Press, NY, (1976)

100. R. F. Egerton, "Electron Energy-Loss Spectroscopy in the Electron Microscope", Plenum Press, London, (1986).

101. N. W. Ashcrotf, and N. D. Mermin, "Solid State Physics", Saunders College Publishing, London (1976).

102. http://webmineral.com/data

103. R. D. Shannon, J. E. Dickinson, G. R. Rossman, "Dielectric Constants of Crystalline and Amorphous Spodumene, Anorthite and Diopside and the Oxide Additivity Rule", *Phys. and Chem. Minerals*, 19, 148-156 (1992).

104. B. Schwartz, "Ceramic Packaging of Integrated Circuits", in *Electronic Ceramics* ed. L. M. Levinson, Marcel Dekker INC, NY (1988).

105. L. L. Hench, and J. K. West, "Principles of Electronic Ceramics", John Wiley & Sons, Inc. U.S. (1990).

106. K. Johnston and M. Finnis, "Electrostatic and Entropic Interactions Between Parallel Interfaces Separated by a Glassy Film", *J. Am. Ceram. Soc.*, 85[10] 2562-2568 (2002).

107. T. Shaw and P. Duncombe, "Forces between Aluminum Oxide Grains in a Silicate Melt and Their Effect on Grain Boundary Wetting", *J. Am. Ceram. Soc.*, 74[10] 2495-2505 (1991).

108. P. Richet and Y. Bottinga, "Anorthite, Andesine, Wollastonite, Diopside, Cordierite and Pyrope: Thermodynamics of Melting, Glass Transitions, and Properties of the Amorphous Phases", Earth and Planetary Sci. Lett., 67[3],415-432 (1984).

109. O. B. Fabrichnaya and I. Nerád, "Thermodynamic Properties of Liquid Phase in the $CaO{\cdot}SiO_2$–$CaO{\cdot}Al_2O_3{\cdot}2SiO_2$–$2CaO{\cdot}Al_2O_3{\cdot}SiO_2$ system", *J. Eur. Ceram. Soc.*, 20[4], 505-515 (2000).

110. J. A. Golczewski, H. J. Seifert and F. Aldinger, "A Thermodynamic Model of Amorphous Silicates", *Calphad*, 22[3], 381-396 (1998).

111. O. H. Kwon and G. L. Messing, "Kinetic Analysis of Solution-Precipitation During Liquid-Phase Sintering of Alumina", J. Am. Ceram. Soc., 73[2] 275-281 (1990).

112. S. I. Bae and S. Baik, "Sintering and Grain Growth of Ultrapure Alumina", *J. Mater. Sci.*, 28, 4197-4204 (1993).

113. C. Scott, M. Kaliszewski, C. Greskovich, and L. Levinson, "Conversion of Polycrystalline Al_2O_3 into Single-Crystal Sapphire by Abnormal Grain Growth", *J. Am. Ceram. Soc.*, 85[5], 1275-1280 (2002).

114. C. W. Park and D. Y. Yoon, "Abnormal Grain Growth in Alumina with Anorthite Liquid and the Effect of MgO Addition", *J. Am. Ceram. Soc.*, 85[6], 1585-1593 (2002).

115. C. W. Park and D. Y. Yoon, "Effects of SiO_2, CaO_2, and MgO Additions on the Grain Growth of Alumina", *J. Am. Ceram. Soc.*, 83[10], 2605-2609 (2000).

116. K. L. Gavrilov, S. J. Bennison, K. R. Mikeska, J. M. Chabala, and R. Levi-Setti, "Silica and Magnesia Dopant Distributions in Alumina by High-Resolution Scanning Secondary Ion Mass Spectrometry", *J. Am. Ceram. Soc.*, 82[4], 1001-1008 (1999).

117. K. L. Gavrilov, S. J. Bennison, K. R. Mikeska, and R. Levi-Setti, "Grain Boundary Chemistry of Alumina by High-Resolution Imaging SIMS", *Acta Mater.*, 47, 4031-4039 (1999).

118. D. Y. Kim, S. M. Wiederhorn, B. J. Hockey, C. A. Handwerker, and J. E. Blendell, "Stability and Surface Energies of Wetted Grain Boundaries in Aluminum Oxide", *J. Am. Ceram. Soc.*, 77[2], 444-453 (1994).

119. C. A. Handwerker, P. A. Morris, and R. L. Coble, "Effects of Chemical Inhomogeneities on the Grain Growth and Microstructure in Al_2O_3", *J. Am. Ceram. Soc.*, 72[1], 130-136 (1989).

120. S. C. Hansen and D. S. Phillips, "Grain Boundary Microstructures in a Liquid-Phase Sintered Alumina (α-Al_2O_3)," *Philos. Mag.* A, 47[2], 209–234 (1983).

121. Y. Q. Wu, Y. F. Zhang, G. Pezzotti, and J. K. Guo, "Effect of Glass Additives on the Strength and Toughness of Polycrystalline Alumina", *J. Eur. Ceram. Soc.*, 22, 159-164 (2002).

122. S. Ramamurthy, B. C. Hebert, and C. B. Carter, "Dewetting of glass-Coated α-Al_2O_3 $\{10\bar{1}0\}$ Surface", *Phil. Mag. Lett.*, 72[5], 269-275 (1995).

123. M. P. Mallamaci and C. B. Carter, "Crystallization of Pseudo-orthorhombic Anorthite on Basal Sapphire", *J. Am. Ceram. Soc.*, 82[1] 33-42 (1999).

124. M. P. Mallamaci and C. B. Carter, "Faceting of the Interface Between Al_2O_3 and Anorthite Glass", *Acta Mater.*, 46[8], 2895-2907 (1998).

125. C. W. Park and D. Y. Yoon, "Effect of Magnesium Oxide on Faceted Vicinal (0001) Surface of Aluminum Oxide", *J. Am. Ceram. Soc.*, 84[2], 456-458 (2001).

126. M. De Graef, B. J. Dalgleish, M. R. Turner, and A. G. Evans, "Interfaces between Alumina and Platinum: Structure, Bonding and Fracture Resistance," *Acta Metall. Mater.*, 40 [Suppl.], S333–S344 (1992).

127. T. Ohji, T. Hirano, A. Nakahira, and K. Niihara, “Particle/Matrix Interface and its Role in Creep Inhibition in Alumina/Silicon Carbide Nanocomposites”, *J. Am. Ceram. Soc.*, 79[1], 33–45 (1996).

128. L. P. Ferroni, G. Pezzotti, T. Isshiki, and H. J. Kleebe, “Determination of Amorphous Interfacial Phases in Al_2O_3/SiC Nanocomposites by Computer-Aided High-Resolution Electron Microscopy”, *Acta Mater.*, 49, 2109-2113 (2001).

129. H. K. Schmid, M. Aslan, S. Assmann, R. Naß, and H. Schmidt, ” Microstructural Characterization of Al_2O_3-SiC Nanocomposites”, *J. Eur. Ceram. Soc.*, 18, 39-49 (1998).

130. S. T. Oh, M. Sando, T. Sekino, and K. Niihara, “Processing and Properties of Copper Dispersed Alumina Matrix Nanocomposites”, *Nanostructured Mater.*, 10[2], 267-272 (1998).

131. S. T. Oh, T. Sekino, and K. Niihara, “Fabrication and Mechanical Properties of 5 Vol% Copper Dispered Alumina Nanocomposite”, *J. Eur. Ceram. Soc.*, 18,31-37 (1998).

132. R. Z. Chen and W. H. Tuan, “Pressureless Sintering of Al_2O_3/Ni Nanocomposites”, *J. Eur. Ceram. Soci.*, 19,463-468 (1999).

133. W. H. Tuan, H. H. Wu, and T. J. Yang, “The Preparation of Al_2O_3/Ni Composites by a Powder Coating Technique”, *J. Mater. Sci.*, 30, 855-859 (1995).

134. W. H. Tuan and R. J. Brook, “Processing of Alumina/Nickel Composites”, *J. Eur. Ceram. Soc.*, 10, 95-100 (1992).

135. D. E. García, S. Schicker, J. Bruhn, R. Janssen, and N. Claussen, “Processing and Mechanical Properties of Pressureless-Sintered Niobium–Alumina-Matrix Composites”, *J. Am. Ceram. Soc.*, 81[2], 429-432 (1998).

136. A. N. Winter, B. A. Corff, I. E. Reimanis, and B. H. Rabin, “Fabrication of Graded Nickel–Alumina Composites with a Thermal-Behavior-Matching Process”, *J. Am. Ceram. Soc.*, 83[9], 2147-2154 (2000).

137. J. Lu, L. Gao, L. Gui, and J. Guo, “Preparation, Thermal Stability and Sintering Behavior of Ni/Al_2O_3 Coated Powders”, *Mater. Chem. Phys.*, 72, 352-355 (2001).

138. N. A. Travitzky and A. Shlayen, “Microstructure and Mechanical Properties of Al_2O_3/Cu-O Composites Fabricated by Pressureless Infiltration Technique”, *Mater. Sci. Eng. A*, A244, 154-160 (1998).

139. H. Prielipp, M. Knechtel, N. Claussen, S. K. Streiffer, H. Müllejans, M. Rühle, and J. Rödel, “Strength and Fracture Toughness of Aluminum/Alumina Composites with Interpenetrating Network”, *Mater. Sci. Eng. A*, A197**,** 19-30 (1995).

140. S. T. Oh, T. Sekino, and K. Niihara, “Effect of Particle Size Distribution and Mixing Homogeneity on Microstucture and Strength of Alunima/Copper Composites”, *Nanostructured Mater.*, 10[2], 327-332 (1998).

141. A. G. Evans, “Perspective on the Development of High-Toughness Ceramics”, *J. Am. Ceram. Soc.*, 73[2], 187-206 (1990).

142. U. Alber, H. Müllejans, and M. Rühle, " Wetting of Copper on α-Al_2O_3 Surfaces Depending on the Orientation and Oxygen Partial Pressure", *Micron*, 30, 101-108 (1999).

143. A. K.-Slimane, B. Mbongo, and D. Tréheux, "Adhesion and Reactivity in the Copper-Alumina System: Influence of Oxygen and Silver", *J. Adhesion Sci. Technol.*, 13[1], 35-48 (1999).

144. A. Avishai, C. Scheu, and W. D. Kaplan, “Amorphous Films at Metal-Ceramic Interfaces”, Zeitschrift für Metallkunde, 94[3], 272-276, (2003).

145. F. S. Ohuchi, “"Metal - Ceramic Interfacial Reactions: A Surface Science Approach" pp. 93-106 in Metal - Ceramic Interfaces, Edited by M. Rühle, A. G. Evans, M. F. Ashby, and J. P. Hirth, Proceedings of an International Workshop, Santa Barbara California, USA 16-18 January (1989).

146. H. O. Moltaji, J. P. Buban, J. A. Zaborac, and N. D. Browning, “Simulating the Oxygen K-Edge Spectrum from Grain Boundaries in Ceramic Oxides Using the Multiple Scattering Methodology”, *Micron*, 31, 381-399 (2000).

147. C. H. Hsueh, A. G. Evans, and R. L. Coble, "Microstructure Development During Final/Intermediate Stage Sintering-I. Pore/Grain Boundary Separation", *Acta Metall*., 30, 1269-1279, (1982)

148. G. Gottstein and L. S. Shvindlerman, "Theory of Grain Boundary Motion in the Presence of Mobile Particles", *Acta Metall. Mater.*, 41[11], 3267-3275, (1993).

149. J. P. Monchoux and E. Rabkin, "Microstructure Evolution and Interfacial Properties in the Fe-Pb System", *Acta Metall.*, 50, 3159-3174, (2002).

150. A. Krell, P. Blank, H. Ma, T. Hutzler, "Transparent Sintered Corundum with High Hardness and Strength",", J. Am. Ceram. Soc., 86[1], 12-18 (2003).

151. J. E. Burke, S. Prochazka, "The effect of MgO on Intergranular Pore Entrapment in Sintered Aluminum Oxide", Sintering – Theory and Practice, Proceeding of the 5th International Round Table Conference on Sintering, Portorož, Yugoslavia, 7-10 September 1981, Editors: D. Kolar, S. Pejovnik, and M. M. Ristic, Material Science Monographs, Vol. 14, pp 335-341.